Graduate Theses and Dissertations   Graduate School

1-1-2002

Physical-Statistical Modeling and Optimization of Cardiovascular Systems

Dongping Du
University of South Florida, dongpingdu@mail.usf.edu

Physical-Statistical Modeling and Optimization of Cardiovascular Systems

by

Dongping Du

A dissertation submitted in partial fulfillment
of the requirements for the degree of
Doctor of Philosophy
Department of Industrial and Management Systems Engineering
College of Engineering
University of South Florida

Co-Major Professor: Hui Yang, Ph.D.
Co-Major Professor: Eric S. Bennett, Ph.D.
Tapas Das, Ph.D.
Alex Savachkin, Ph.D.
Ashok Kumar, Ph.D.
Fabio M. Leonelli, M.D.

Date of Approval:
April 14, 2015

Keywords: cardiac arrhythmias, glycosylation, design of computer experiments, simulation, stochastic metamodeling

Dedication

To my beloved mother, father and brother.

Acknowledgments

I would like to express my deepest appreciation to my advisor, Dr. Hui Yang, for the academic advice, inspirations, and continuous motivations for my PhD study. I also owe my infinite gratitude to my co-advisor, Dr. Eric S. Bennett, for his guidance, high standard, professionalism and immense impact on my research. Dr. Hui Yang and Dr. Eric S. Bennett are wonderful teachers, excellent researchers, and inspiring advisors – the perfect mentors every graduate student can dream of. I feel fortune to come across them in my life.

I would like to thank my committee members Dr. Tapas Das, Dr. Alex Savachkin, Dr. Ashok Kumar, and Dr. Fabio M. Leonelli for their valuable advice in my research direction and methodologies. A special thank goes to Dr. Yu Zhang for her kind help in serving as the Chair. Additionally, I would like to show my sincere appreciation to Dr. Jose Zayas-Castro for his enormous encouragement on my Ph.D. study.

I would also like to thank all other faculties and staff members, Dr. Bo Zeng, Dr. Paul Schnitzler, Dr. Patricia Anzalone, Ms. Gloria Hanshaw, Ms. Liz Conrad, and Mr. Rafael Urena in the IMSE department for their generous help during my Ph.D. studies. Meanwhile, I would like to express my appreciation to Ms. Catherine Burton for her valuable corrections on my dissertation draft.

Finally, I wish to express my pure-hearted appreciation to my beloved parents and brother. Without their constant support, continual encouragement and endless love, I would have never accomplished my study and achieved what I have so far. I am indebted to them tremendously and love them forever.

Table of Contents

List of Tables

List of Figures

v

Abstract

Heart disease remains the No.1 leading cause of death in U.S. and in the world. To improve cardiac care services, there is an urgent need of developing early diagnosis of heart diseases and optimal intervention strategies. As such, it calls upon a better understanding of the pathology of heart diseases.

Computer simulation and modeling have been widely applied to overcome many practical and ethical limitations in in-vivo, ex-vivo, and whole-animal experiments. Computer experiments provide physiologists and cardiologists an indispensable tool to characterize, model and analyze cardiac function both in healthy and in diseased heart. Most importantly, simulation modeling empowers the analysis of causal relationships of cardiac dysfunction from ion channels to the whole heart, which physical experiments alone cannot achieve.

Growing evidences show that aberrant glycosylation have dramatic influence on cardiac and neuronal function. Variable but modest reduction in glycosylation among congenital disorders of glycosylation (CDG) subtypes has multi-system effects leading to a high infant mortality rate. In addition, CDG in all young patients tends to cause Atrial Fibrillation (AF), i.e., the most common sustained cardiac arrhythmia. The mortality rate from AF has been increasing in the past two decades. Due to the increasing healthcare burden of AF, studying the AF mechanisms and developing optimal ablation strategies are now urgently needed.

Very little is known about how glycosylation modulates cardiac electrical signaling. It is also a significant challenge to experimentally connect the changes at one organizational level (e.g.,

electrical conduction among cardiac tissue) to measured changes at another organizational level (e.g., ion channels). In this study, we integrate the data from in vitro experiments with in-silico models to simulate the effects of reduced glycosylation on the gating kinetics of cardiac ion channel, i.e., hERG channels, Na+ channels, K+ channels, and to predict the glycosylation modulation dynamics in individual cardiac cells and tissues.

The complex gating kinetics of Na+ channels is modeled with a 9-state Markov model that have voltage-dependent transition rates of exponential forms. The model calibration is quite a challenge as the Markov model is non-linear, non-convex, ill-posed, and has a large parametric space. We developed a new metamodel-based simulation optimization approach for calibrating the model with the in-vitro experimental data. This proposed algorithm is shown to be efficient in learning the Markov model of Na+ model. Moreover, it can be easily transformed and applied to many other optimization problems in computer modeling.

In addition, the understanding of AF initiation and maintenance has remained sketchy at best. One salient problem is the inability to interpret intracardiac recordings, which prevents us from reconstructing the rhythmic mechanisms for AF, due to multiple wavelets' circulating, clashing and continuously changing direction in the atria. We are designing computer experiments to simulate the single/multiple activations on atrial tissues and the corresponding intra-cardiac signals. This research will create a novel computer-aided decision support tool to optimize AF ablation procedures.

Chapter 1 Background and Literature Review

1.1   Electrical Conduction System of Heart

The blood-pumping events of the heart are controlled by the electrical conduction system. As shown in Figure 1-1, Pacemaker cells start a self-generating impulse with a rate of 60 to 100 beats per minute (bpm) at the sinoatrial node (SAN) that is located at the border of Superior Vena Cava and Right Atrium. This electrical impulse propagates through both atria to the Atrioventricular (AV) node located in the floor of the Right Atrium. The AV node receives the electrical impulse and transmits to the Bundle of His. The Bundle of His then divides into a right bundle branch and two left bundle branches, which terminate at a complex network of Purkinje Fibers that spreads throughout the ventricles. When impulse reaches the ventricles, the ventricular myocardium is stimulated and contraction occurs.

The electrical impulse excites cardiac myocytes from resting states, and causes the flow of ions in/out of cell membranes, which leads to the contractions of cardiac myocytes. In resting state, sodium (Na+) ions stay outside of the cell and potassium (K+) ions stay inside of the cell. Because the charge of Na+ ions is stronger than the K+ ions, the cell is polarized. When the stimulation reaches, the Na+ ions move into the cell quickly through the ion channels. Then K+ ions flow out of the cell through K+ channels, and at the same time, Calcium (Ca++) ions move slowly into the cell through Ca++ channels. The flows of Na+, K+ and Ca++ ions depolarize the cell and start the contraction (Phase 0). After the depolarization of the cell, the fast sodium channels close, and K+ ions start to move in and the Na+ ions start to move out, which causes an early repolarization

(Phase 1). The slowly repolarization continues while Ca++ ions keep flowing into the cell slowly (Phase 2). The Ca++ channels close after phase 2, and K+ ions move out of cell rapidly, at the same time, K+ ions are transported to the inside of the cell, and Na+ ions are shipped outside of the cell by potassium-sodium pump (Phase 3). The cell goes back to polarized state (Phase 4) gradually and gets ready for another contraction. The action potential (AP) is a short-lasting event in which the difference of membrane potential between the interior and the exterior of cardiac cells raises and falls while the ions (i.e., Na+, K+, Ca++) flow through the cell membrane. Figure 1-2 shows a single cycle of AP. The AP rises to a positive value quickly (phase 0), and goes back to resting potential (phase 4) gradually through phase 1-3.
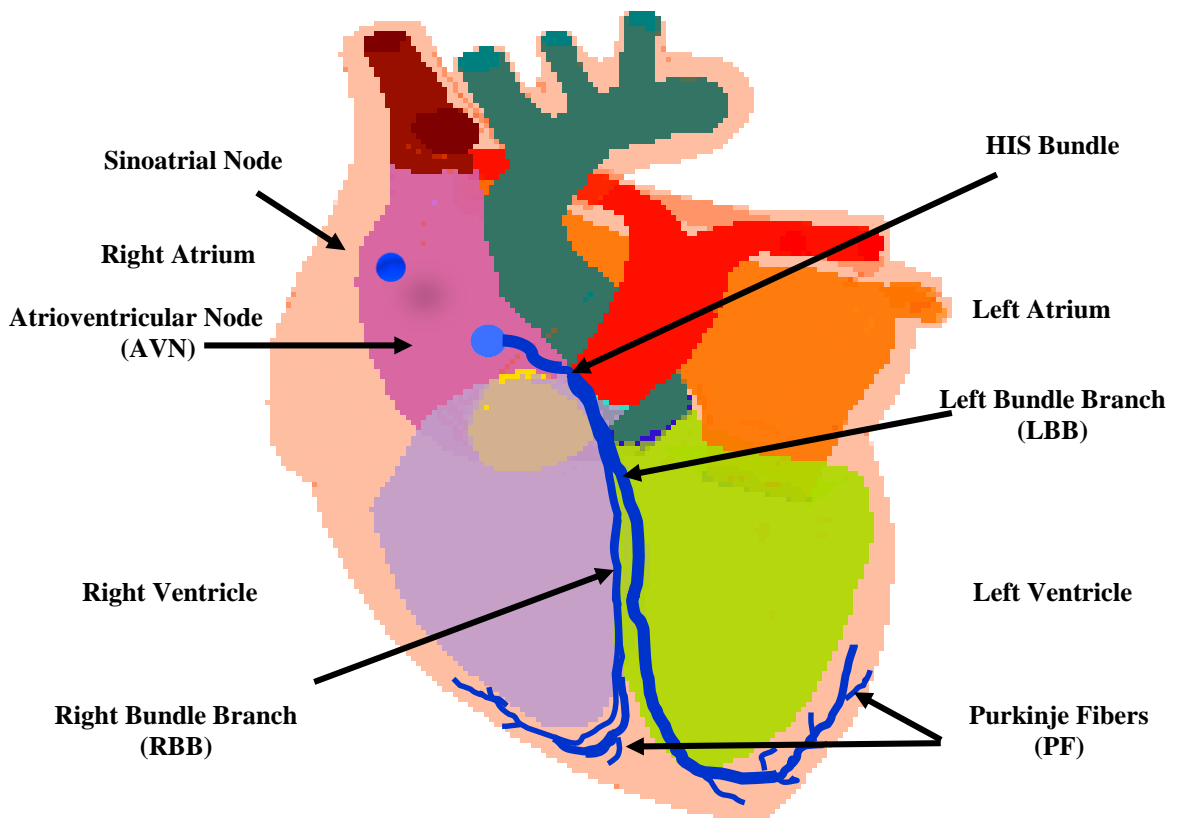
Figure 1-1 Cardiac conduction system.
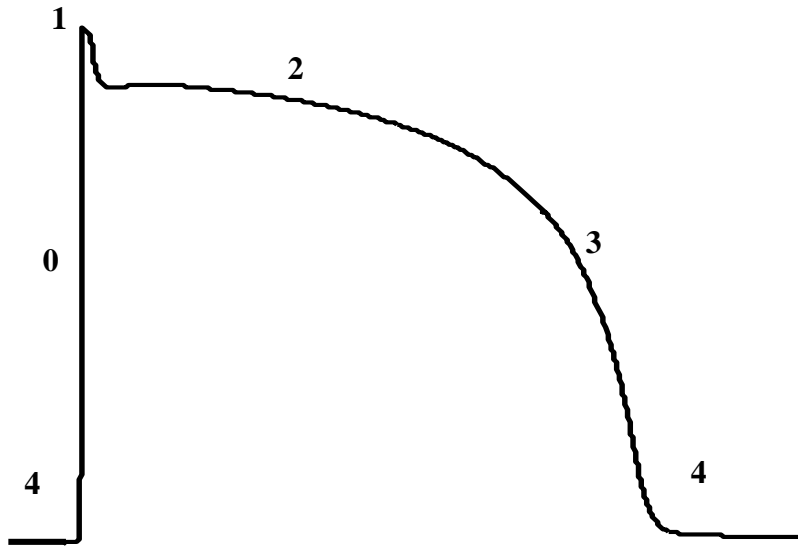
Figure 1-2 Five phases in the cardiac action potential.

1.2 Glycosylation-Associated Cardiac Disease

As mentioned above, the net change of transmembrane potential in a cardiac myocyte during a single contraction is produced by the orchestrated function of ion channels. A slight change in the ion channel activity may affect AP waveforms and electrical conduction throughout the heart, thereby potentially lead to severe cardiac disorder. Ion channels are heavily glycosylated with up to 35% of a mature protein's mass comprised of glycan structure [1]. It was shown that Na+ and K+ channels can be extensively post-translationally modified by protein glycosylation through isoform-specific mechanisms [2-5]. Typically, glycosylation-dependent gating effects were imposed on ion channels primarily by the terminal residue attached to N- and O-glycan, sialic acid [5-7]. Montpetit *et al* showed that cardiac glycome (i.e., the complete set of glycan structure produced in the heart) varies between atria and ventricles, and changes differentially during the development of each cardiac chamber [4]. In addition, the regulated expression of a single glycosgene is shown to modulate AP waveforms and gating of less sialylated Na_v consistently [3].

3

Growing evidence suggests that reduced glycosylation has dramatic effects on ion channels gating and cardiac electrical signaling. There is a set of >40 distinct forms of inherited human diseases of reduced glycosylation known as Congenital Disorders of Glycosylation (CDG) caused, typically, by a mutation or deficiency in glycogene that results in a relatively modest reduction in glycoprotein glycosylation [1, 8]. This variable but modest reduction in glycosylation among CDG subtypes causes a high infant mortality rate. CDG patients often present with severe cardiac deficits, but the mechanisms are not yet understood. Recently reported prevalence of cardiac involvement prompted experts to suggest screening for cardiac dysfunction in all CDG patients and for CDG in all young patients suffering from cardiomyopathy of unknown etiology.

1.3   Atrial Fibrillation

Atrial Fibrillation (AF) is the most common type of arrhythmia that affects more than 5 million Americans. During AF, the atria beat chaotically and irregularly. The blood pools in the atria aren't pumped completely into the ventricles. As a result, the heart's upper and lower chambers don't work cooperatively as they should. The AF occurs because the electrical signals of the heart are not initiated in the SA node. Instead, they begin in the pulmonary veins or another part of atria. These irregular signals spread throughout the atria in a rapid and disorganized way, and cause atria to fibrillate. The impact of AF on healthcare systems is overwhelming, due to high risk of stroke, increased mortality, impaired quality of life and hospitalization.

AF has three different stages: paroxysmal AF, persistent AF and Permanent AF. In paroxysmal AF, abnormal electrical activities occur occasionally, and stop on their own. Episodes can be mild or severe and last for seconds, minutes, hours or even days before stopping and returning back to normal. Persistent AF cannot be stopped until some treatment interventions. It is usually caused by frequent and over time rotors and wavelets. The treatments include pharmacological and

catheter-based interventions. However, permanent AF is a very complex situation that cannot be easily stopped by treatments.

Catheter ablation is an established treatment based on placement of lesions in the left and right atrium with the goal of preventing abnormal activations. The location of the lesions can be anatomically-based such as lines circled around the pulmonary veins. During the procedure, physicians use the electrodes at the end of catheters to record electrical activity in the atria (i.e., intracardiac electrogram). Further, cardiologists pinpoint the potential AF sources and deliver energy through the catheter to create incision lines that block faulty electrical pathways. The key to a successful treatment is accurate identification and ablation of the abnormal signal and tissues. However, the understanding of AF initiation and maintenance has remained sketchy at best. One salient problem is the inability to interpret intracardiac recordings, which have thus far prevented us from reconstructing the rhythmic mechanisms for AF. This makes the task of locating the abnormal triggers very challenging. As a result, physicians often need to make ablation decisions using ad hoc or heuristic strategies. There is an urgent need to realize the full potentials of intracardiac electrograms for optimizing ablation decisions.

1.4 Modeling of Cardiac Electrical Signaling

Modeling and simulation provide more electrophysiological insights of cardiac electrical signaling. A large amount of biological data has been generated over the past decades using advanced technologies. These new generated data has overwhelmed our knowledge to understand it. In many cases, the molecular, cellular, organ and system functions are unknown. Even when we understand functions at genetic level, successful treatment and therapy depends on the knowledge of how behaves at, e.g., molecular levels, interact with the rest of the relevant cellular function. Without this integrative knowledge, it is difficult to identify which disease is relevant to a specific

enzyme or transporter, and it is certainly difficult to know and control the side effects that are unpredictable from molecular or cellular data alone. The interactions among different organizational levels cannot be inspected alone with databases generated through physical experiments. In order to understand the integrative properties of the system, we need to compute the interactions of the properties within the whole biological system [10]. This provides opportunities for analysis by simulation.

In the past decades, the iterative interaction between experiments and simulations benefit the development of cardiac cell models greatly. Models have been built for all main type of cardiac myocytes, and for some type of myocytes, multiple models exist. The current cardiac modeling approaches can be generally categorized in to two groups as follows: The first group is macro/minimal models such as cellular automata model, fitzHugh-Nagumo model and Barkley Model. The second group is micro/maximal models, e.g., Hodgkin-Huxley model, Luo-Rudy model, Rasmusson model and Nygren-Lindblad model [11-12]. The macro/minimal models do not provide detailed ion physics, but they are easier to be incorporated into a large-scale system. The micro/maximal models include hundreds of equations to describe the detailed ion channel biophysics but increase the complexity of large-scale experiments. Alan Hodgkin and Andrew Huxley first described how action potential in neurons are initiated and propagate with a mathematical model (Hodgkin-Huxley model) in 1952. Based on Hodgkin-Huxley model, various types of models, e.g., Purkinje fiber model, ventricular model, atrial model, of different animals, e.g., mouse, pig, rabbit, were developed in the past 60 decades. Beeler and Reuter published the first ventricular model with four ionic currents and 8 variables in 1977. Luo and Rudy improved the Beeler and Reuter's model with more experimental information, and formulated a modified ventricular model (Phase 1 Luo-Rudy model) in 1991. In 1994, they further improved the model

by reformulating and including more ion currents. Priebe and Beuckelman proposed a model of human ventricular cells in 1998, and a reduced version of this model was proposed by Bernus *et al* in 2002 [13]. In 2004, ten Tusscher *et al* formulated a new model for human ventricular cells based on more experimental data, and this model is efficient for large-scale spatial simulations of reentrant phenomena [14-15]. In addition, Iyer *et al* formulated a human left-ventricular epicardial model. In Iyer's model, there are 67 variables, and Markov models are applied to simulate gating kinetics of some ion channels. Besides the human ventricular model, Rasmusson *et al* developed a mathematical model of the action potential of mouse ventricular myocytes in 2004. This model has been widely used to study the electrical signaling of mouse ventricular cells and the electrophysiology of cardiac tissue [16]. In this current study, we also applied this model to simulation the electrical activities of the heart across multiple physical scales such as ventricular cells, 1D cell cables and 2D tissues.
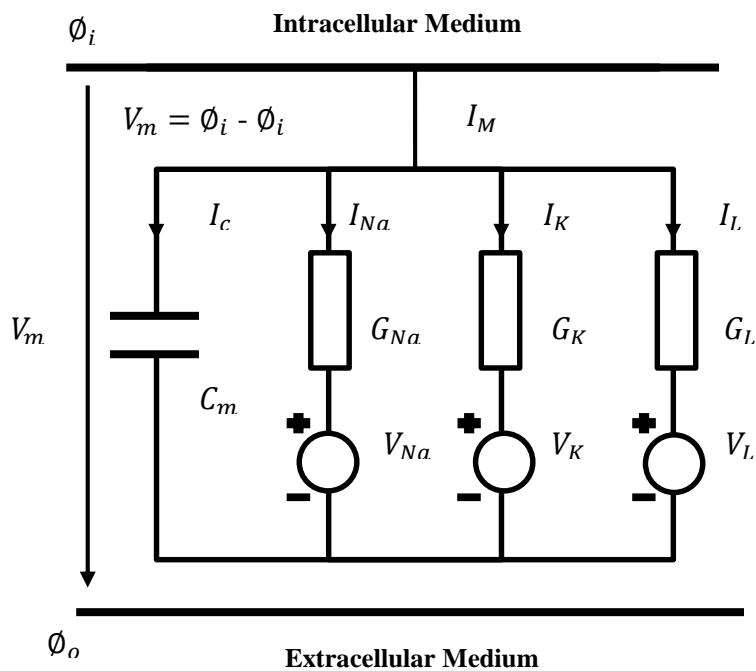
Figure 1-3 The equivalent circuit of the Hodgkin-Huxley model.

The micro/maximal models of cardiac cells are built following similar principles, i.e., the cardiac cell is modeled as a structured electric circuit with capacitors, resistors, and batteries. As shown in Figure 1-3, the Hodgkin-Huxley model is constructed using the basic electric circuit components of voltage source, resistance and capacitance [46]. The ion permeability of the membrane for different ions, e.g. Na+, K+, is considered as the specific conductance per unit area. Based on Ohm's law, the model conductance can be formulated as [46]:

$$G_{Na} = \frac{I_{Na}}{V-E_{Na}}, \qquad G_K = \frac{I_K}{V-E_K}, \qquad G_{Na} = \frac{I_L}{V-E_L}$$

where G_{Na}, G_K, G_L are membrane conductance per unit area for Na+, K+ and leakage current; I_{Na}, I_K and I_L are the corresponding ion currents; V_{Na}, V_K and V_L are the Nernst voltage for Na+, K+ and other ions; V is the action potential. The transmembrane current can be formulated as [46]:

$$I_m = C_m\frac{dV}{dt} + (V - E_{Na})G_{Na} + (V - E_K)G_K + (V - E_L)G_L$$

The conductance of Na+ ions can be calculated as:

$$G_{Na} = G_{Na\,max}m^3h$$

m and h can be obtained by the ordinary differential equations:

$$\frac{dm}{dt} = \alpha_m(1 - m) - \beta_m m \qquad \frac{dh}{dt} = \alpha_h(1 - h) - \beta_h h$$

where α's and β's are functions of V. The conductance of K+ ions can be calculated following the similar way. Many modern neuronal and cardiac AP model were developed following similar basis after Hodgkin-Huxley model. However, more ion currents are taken into consideration in the models developed later. Figure 1-4 shows a schematic diagram of the dynamic Luo-Rudy (LRd) ventricular cell model. This model includes a fast inward sodium current, an outward potassium current, and a time-independent potassium current [47]. The Ten Tusscher *et al* modeled and the Bondarenko *et al* model describe the electrophysiology of cardiac cells following the same

schemes, but have more transmembrane currents. The relatively detailed models enable a more accurate interpretation of the cellular mechanisms.
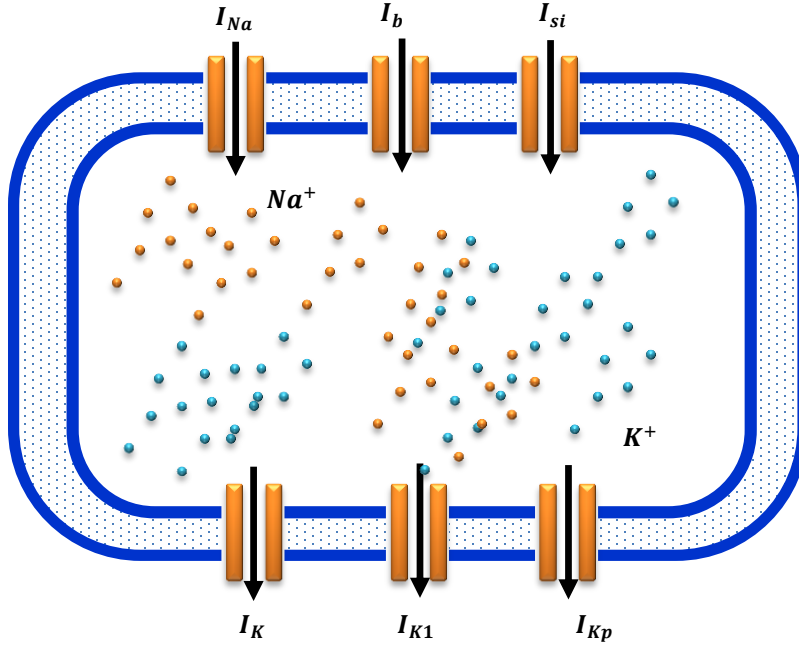
Figure 1-4 Schematic diagram of the dynamic Luo-Rudy (LRd) ventricular cell model.

The activities of tissue are like a functional syncytium of electrically coupled cells. The tissue can be simulated as a resistor network, and the electrical propagation among tissue can be considered as an excitable medium in 1D, 2D and 3D. Among this excitable medium, i.e. cardiac tissues, cells are coupled diffusively through the transmembrane voltage. There are two types of tissue models: bidomain model and monodomain model. In bidomain model, cardiac tissue is simulated as a syncytium composed of intracellular and extracellular domains. It simulates the current flow, distribution of electrical potential and the conservation of charge and current [17, 48]:

$$\nabla \cdot \mathbf{G_i}(\nabla V_m + \nabla \emptyset_e) = \beta_m (C_m \frac{\partial V_m}{\partial t} + i_{ion})$$

$$\nabla \cdot \left((\mathbf{G_i} + \mathbf{G_e})\nabla \emptyset_e\right) = -\nabla \cdot (G_i \nabla V_m)$$

9

where V_m is the membrane potential, $\mathbf{G_i}$ and $\mathbf{G_e}$ are conductivity tensors determined by the anisotropy of cardiac tissues. Their components depend on the conductivities and local orientation of cardiac tissue in the coordinate system of the model.

The monodomain model assumes the anisotropy of the intracellular and extracellular spaces is the same. It describes the membrane potential (V_m) with a partial differential equation [18, 48]:

$$\frac{\partial V_m}{\partial t} = \nabla \cdot \mathbf{D}\nabla V_m - \frac{i_{ion}}{C_m}$$

where $\mathbf{D}$ is a diffusion tensor or scalar diffusion coefficient:

$$\boldsymbol{D} = D_2\mathbf{I} + (D_1 - D_2)\mathbf{ff}^T$$

where D_1 is the longitudinal coefficient for propagation along fibers, D_2 is a transverse coefficient for propagation orthogonal to the fibers if the fiber direction is given by vector $\mathbf{f}$.

Monodomain and bidomain models have been demonstrated to be very close when there is no injection of current into the extracellular space [19, 48]. Potse et al. compared the patterns of action potential propagation simulated using monodomain and bidomain models. They found the patterns obtained from both models were almost identical when there is not external stimulation [20]. Similarly, Roth simulated spiral wave tip trajectories with both bidomain and monodomain models. The study showed similar trajectories in the two cases [21]. The monodomain model is preferred when there are no external stimuli because monodomain models are numerically easier to be solved. However, bidomain models are necessary when currents are injected into the extracellular space during the external stimulation and defibrillation [22]. While simulating defibrillation, it is important to consider the unequal anisotropy of the intracellular and extracellular spaces, because the virtual electrodes generated are critical for successful defibrillation [23]. The bidomain models can be expanded to higher domains, for example Sachse et al. applied bidomain model to fibroblasts by adding an additional domain [24].

Modeling the functional relationship between the discrete structure and integrated functions of heart at microscope and macroscope are quite challenging. Different assumptions and simplifications are made while building models of cardiac cells and tissues. There is no general framework for simulating cellular electrophysiology, tissue electrical activity, and geometrical features. There are still many open questions to be answered. For example, there are no well adapted parameters for determining the patterns of APs in cardiac cells and the propagation of APs among tissues. More work need to be done to efficiently establish the biophysical basis for these parameters and to understand the sensitivity of these parameters to cell and tissue activities. In addition, it is essential to integrate models with experimental data to simulate and predict disease mechanisms and treatment effects. However, many of the models are difficult to calibrate to simulate the physical data, and many phenomena investigated using tissue models are difficult to verify experimentally. Representation of pathological function is still challenging because robust methods and parameters to represent the disease conditions such as arrhythmias and infarction have not been fully developed. This study makes efforts to address the challenges and answer all these open questions in the cardiac modeling area.

1.5   Simulation Optimization

Simulation optimization finds the optimal input variables from all potential candidates without explicitly evaluating each possible set of variables. In simulation optimization, the output of a simulation model is used by the optimization method to evaluate the performance of each search for the optimal solution, and provide feedback to the search thereby guiding further input to the simulation model. There are six major types of simulation optimization methods: Gradient Based Search Methods, Stochastic Optimization, Response Surface Methodology (RSM), Heuristic Methods, A-Teams and Statistical Methods [25]. Gradient based search methods estimate the

gradient of the response function (∇f) to learn the shape of the objective function. The optimal solution is searched with deterministic mathematical programming approaches. Finite differences [26], likelihood ratios [27] and perturbation analysis [28] are some common methods for gradient search optimization methods. Stochastic optimization applies stochastic approaches to estimate or measure the value of the objective functions that cannot be evaluated analytically. Conventionally it is an iterative schemes based on gradient estimation. Some stochastic optimization algorithms can be found in [29-33]. Heuristic methods, e.g., Genetic Algorithms [34], Evolutionary Strategies [35], Simulated Annealing [36, 37], Tabu Search [38, 39], Nelder and Mead's Simplex Search and A-Teams [40], include a set of direct search methods for finding the optimal solutions. Statistical methods basically simulate the system under a number of measurements underlying some probability distributions, and it includes Importance Sampling and Ranking and Selection. RSM method generally is to obtain an approximation in terms of functions between the input variables and the output objective function, i.e., response. The approximation of the response on the entire domain of interest is conventionally called metamodel. This metamodel can be different types of model, for example, regression model and neural network models. Once the metamodel is established, the estimated optimum can be evaluated using appropriate deterministic optimization procedures. However, RSM is not always applied for optimization purpose. Sequential RSM is sometimes used to determine a search strategy, for example to find the best next point.

In the simulation optimization community there is a long history of research on experiment design for applying metamodels to replace the time-consuming simulation model. Metamodels serve as surrogate models that approximate the input/output functions defined by computer experiments. It has been illustrated to be sufficient in locating the optimum solution. In simulation optimization polynomial regression models are applied to fit the response surface of the system of

interest [41]. In addition, the krigging methodology becomes increasingly popular and has been quite successful for investigating uncertainties of the unknown response in computer experiments [42]. Many previous studies focused on the application of krigging model, e.g. Gaussian Process (GP) model, for calibrating computer models in the engineering domain, e.g., Kennedy and O'Hagan [43], Qian and Wu [44], and Chang and Joseph [45]. However, little has been done in the cardiovascular domain. Calibrating cardiac models is not a straightforward application of aforementioned works, due to nonlinear/non-convex characteristics of models and different types of function responses. In particular, calibrating cardiac models needs to specifically consider the kinetics and physical properties of ion channels, cells, tissues, and the heart. This investigation made one of the first attempts to bridge the gaps in statistical metamodeling between engineering and cardiac domains.

1.6   References

[1]   A. R. Ednie and E. S. Bennett, "Modulation of voltage-gated ion channels by sialylation," in Comprehensive Physiology. Hoboken, NJ, USA: Wiley, pp. 1269–1301, 2012.

[2]   T. A. Schwetz, S. A. Norring, A. R. Ednie, and E. S. Bennett, "Sialic acids attached to O-glycans modulate voltage-gated potassium channel gating," J. Biol. Chem., vol. 286, pp. 4123–4132, 2011.

[3]   M. L.Montpetit, P. J. Stocker, T. A. Schwetz, J. M. Harper, S. A. Norring, L. Schaffer, S. J. North, J. Jang-Lee, T. Gilmartin, S. R. Head, S. M. Haslam, A. Dell, J. D. Marth, and E. S. Bennett, "Regulated and aberrant glycosylation modulate cardiac electrical signaling," Proc Nat. Acad. Sci. USA, vol. 106, pp. 16517–16522, 2009.

[4]   P. J. Stocker and E. S.Bennett, "Differential sialylationmodulates voltagegated Na+ Channel gating throughout the developing myocardium," J. Gen. Physiol., vol. 127, pp. 253–265, Mar. 1, 2006.

[5]   I. Watanabe, J. Zhu, J. J. Sutachan, A. Gottschalk, E. Recio-Pinto, and W. B. Thornhill, "The glycosylation state of Kv1.2 potassium channels affects trafficking, gating, and simulated action potentials," Brain Res., vol. 1144, pp. 1–18, 2007.

[6]   C. A. Ufret-Vincenty, D. J. Baro, and L. F. Santana, "Differential contribution of sialic acid to the function of repolarizing K+ currents in ventricular myocytes," Amer. J. Physiol.—Cell Physiol., vol. 281, pp. C464–C474, Aug. 1, 2001.

[7] Y. Zhang, H. A. Hartmann, and J. Satin, "Glycosylation influences voltage dependent gating of cardiac and skeletal muscle sodium Channels," J. Membrane Biol., vol. 171, pp. 195–207, 1999.

[8] H. H. Freeze, "Genetic defects in the human glycome," Nat. Rev. Genet., vol. 7, pp. 537–551, 2006.

[9] J. Jaeken, "Congenital disorders of glycosylation (CDG): Update and new developments," J. Inherit. Metab. Dis., vol. 27, pp. 423–426, 2004.

[10] D. Noble, "Modeling the Heart from Genes to Cells to the Whole Organ," Science, vol. 295, pp. 1678–1681, 2002.

[11] J. R. Silva and Y. Rudy, "Multi-scale electrophysiology modeling: from atom to organ," The Journal of General Physiology, vol. 135, pp. 575-581, June 01, 2010.

[12] E. V. Bondarenko and L. R. Rasmusson, "Simulations of propagated mouse ventricular action potentials: effects of molecular heterogeneity," Am J Physiol Heart Circ Physiol, vol. 293, pp. H1816-H1832, 2007.

[13] O. Bernus, R. Wilders, C.W. Zemlin, H. Verschelde, A.V. Panfilov, "A computationally efficient electrophysiological model of human ventricular cells," Am J Physiol Heart Circ Physiol., vol. 282, pp. 2296-2308, June 01, 2002.

[14] K. H. W. J. ten Tusscher, D. Noble, P. J. Noble and A. V. Panfilov, "A model for human ventricular tissue," Am J Physiol Heart Circ Physiol, vol. 286, pp. 1573-1589, 2004.

[15] K. H. W. J. ten Tusscher and A. V. Panfilov, "Alternans and spiral breakup in a human ventricular tissue model," Am J Physiol Heart Circ Physiol, vol. 291, pp. H1088-H1100, September 01, 2006.

[16] V. E. Bondarenko, G. P. Szigeti, G. C. L. Bett, S. Kim and R. L. Rasmusson, "Computer model of action potential of mouse ventricular myocytes," American Journal of Physiology - Heart and Circulatory Physiology, vol. 287, pp. H1378-H1403, September 01, 2004.

[17] C.S., Henriquez, "Simulating the electrical behavior of cardiac tissue using the bidomain model," Critical Reviews in Biomedical Engineering, vol. 21, pp. 1-77, 1993.

[18] A.V. Panfilov, J.P. Keener, "Re-entry in three-dimensional Fitzhugh-Nagumo medium with rotational anisotropy," Physica D, vol. 84, pp545-552, 1995.

[19] P. Colli Franzone, L. Pavarino, B. Taccardi, "Simulating patterns of excitation, repolarization and action potential duration with cardiac Bidomain and Monodomain models," Mathematical Biosciences, vol. 197, pp. 35-66, 2005.

[20] M., Potse, B., Dube, J., Richer, A., Vinet, R.M., Gulrajani, "A comparison of monodomain and bidomain reaction-diffusion models for action potential propagation in the human heart, " IEEE Transactions on Biomedical Engineering, vol. 53, pp. 2425-2435, 2006.

[21] B.J., Roth, "Meandering of spiral waves in anisotropic cardiac tissue," Physica D, vol. 150, pp. 127-136, 2001.

[22] N., Trayanova, "Defibrillation of the heart: insights into mechanisms from modelling studies," Experimental Physiology, vol. 91, pp. 323-337, 2006.

[23] J. P., Wikswo, S.F., Lin, R.A., Abbas, "Virtual electrodes in cardiac tissue: a common mechanism for anodal and cathodal stimulation, " Biophysical Journal, vol. 73, pp. 2195-2210, 1995.

[24] F. B., Sachse, A. P., Moreno, G., Seemann, J. A., Abildskov, "A model of electrical conduction in cardiac tissue including fibroblasts," Annals of Biomedical Engineering, vol. 37, pp. 874-889, 2009.

[25] Y., Carson, A., Maria, "Simulation optimization: methods and applications," in Proceeding of the 1997 Winter Simulation Conference, pp. 118-126, 1997.

[26] F., Azadivar, "A tutorial on simulation optimization," in Proceedings of the 1992 Winter Simulation Conference, pp. 198-204, 1992.

[27] P. W., Glynn, "Likelihood ratio derivative estimators for stochastic systems," Proceedings of the 1989 Winter Simulation Conference, pp. 374-380. 1989.

[28] Y. C., Ho, and X. R., Cao. "Perturbation analysis of discrete event dynamic systems", New York: Springer, 1991.

[29] S., Andradottir, "A new algorithm for stochastic optimization," Proceedings of the 1990 Winter Simulation Conference, pp. 364-366, 1990.

[30] Y. T., Leung, and R., Suri. "Finite-time behavior of two simulation optimization algorithms," Proceedings of the 1990 Winter Simulation Conference, pp. 372-376, 1990.

[31] M. C., Fu, J. Q., Hu. "Conditional Monte Carlo: gradient estimation and optimization applications, " Boston, MA: Kluwer Academic, 1997.

[32] P., Glasserman, "Gradient estimation via perturbation analysis", 1st ed. Dordrecht, Netherlands: Kluwer Academic Publisher Group, 1991.

[33] Y. C., Ho, X. R., Cao. "Discrete event dynamics systems and perturbation analysis," Dordrecht, Netherlands: Kluwer Academic Publisher Group, 1991.

[34] J. H., Holland, "Genetic algorithms", Scientific American, pp. 66-72. 1992.

[35] H. P., Schwefel, "Evolution and optimum seeking", 6th ed. New York: John Wiley, 1995.

[36] N., Metropolis, A., Rosenbluth, M., Rosenbluth, A., Teller and E., Teller. "Equation of state calculations by fast computing machines," Journal of Chemical Physic, vol. 21, pp. 1087-1092, 1953.

[37] S. Kirkpatrick, C. D. Gelatt, Jr. and M. P., Vechi. "Optimization by simulated annealing," Science, vol. 221, pp. 671-680, 1983.

[38] F. Glover, "Tabu search - part I," ORSA Journal on Computing, vol. 1, no. 3, summer 1989.

[39] F. Glover, "Tabu search - part II, " ORSA Journal on Computing, vol. 2, no. 1, Winter 1990.

[40] P. S. De Souza, and S. N. Talukdar, "Genetic algorithms in asynchronous teams," Proceedings of the 4th International Conference on Genetic Algorithms, 392-397, 1991.

[41] M. C. Fu, "Optimization via simulation: a review." Annals of Operations Research, vol. 53, no.1, pp. 199-247, 1994.

[42] B. Ankenman, B. L. Nelson, and J. Staum, "Stochastic kriging for simulation metamodeling." Operations Research, vol.58 no. 2, pp. 371-382, 2010

[43] M. C. Kennedy, and A. O'Hagan. "Bayesian calibration of computer models," Journal of the Royal Statistical Society: Series B (Statistical Methodology) vol. 63, no. 3, pp. 425-464, 2001.

[44] Peter Z. G. Qian, H. Wu, and C. F. J. Wu, "Gaussian process models for computer experiments with qualitative and quantitative factors," Technometrics, vol. 50, no. 3, pp. 383-396, 2008.

[45] C. Chang and V. R. Joseph, "Model calibration through minimal adjustments," Technometrics, vol. 56, no. 4, 2014.

[46] J. Malmivuo and R. Plonsey, "Bioelectromagnetism - principles and applications of bioelectric and biomagnetic fields." New York: Oxford University Press, 1995.

[47] C. Luo and Y. Rudy, "A Model of Ventricular Cardiac Action Potential," Circulation Research, vol. 68, no. 6, pp. 1501-1526 1991.

[48] R. H. Clayton, O. Bernus, E. M. Cherry, H. Dierckx, F. H. Fenton, L. Mirabella, A. V. Panfilov, F. B. Sachse, G. Seemann and H. Zhang, "Models of cardiac tissue electrophysiology: Progress, challenges and open questions," *Progress in Biophysics and Molecular Biology,* vol. 104, pp. 22-48, 2011.

Chapter 2 In-Silico Modeling of Glycosylation Modulation Dynamics in hERG Ion Channels and Cardiac Electrical Signals[1]

Cardiac action potentials (AP) are produced by the orchestrated functions of ion channels. A slight change in ion channel activity may affect the AP waveform, thereby potentially increasing susceptibility to abnormal cardiac rhythms. Cardiac ion channels are heavily glycosylated, with up to 30% of a mature protein's mass comprised of glycan structures. However, little is known about how reduced glycosylation impacts the gating of hERG (human ether-a-go-go related gene) channel, which is partially responsible for late phase 2 and phase 3 of the AP. This study integrates the data from in vitro experiments with in-silico models to predict the glycosylation modulation dynamics in hERG ion channels and cardiac electrical signals. The gating behaviors of hERG channels were measured under four glycosylation conditions, i.e., full glycosylation, reduced sialylation, mannose-rich. And N-glycanase treated. Further, we developed in-silico models to simulate glycosylation-channel interactions and predict the effects of reduced glycosylation on multi-scale cardiac processes (i.e., cardiac cells, 1-D and 2-D tissues). From the in-silico models, reduced glycosylation was shown to shorten the repolarization phase of cardiac APs, thereby influencing electrical propagation in cardiac fibers and tissues. In addition, the patterns of derived electrocardiogram show that reduced glycosylation of hERG channel shortens the QT interval and decreases the re-entry rate of spiral waves. This work suggests new pharmaceutical targets for the long QT syndrome and potentially other cardiac disorders.

2.1 Introduction

Glycosylation is a common enzymatic process in cardiac cells. It was shown that nearly 30% of a mature protein's mass is comprised of glycan structures [1]. It is established that voltage-gated Na$^+$ channels (Na_v) and K$^+$ channels (K_v) are also known to be modulated by posttranslational glycosylation through isoform-specific mechanisms [2-5]. Many previous studies showed that glycosylation-dependent gating effects were imposed on ion channels primarily by the terminal residue attached to N- and O-glycans, sialic acid [5-7]. The addition and removal of glycans from proteins and lipids are completed by the activity of >200 glycosidases, glycosyltransferases, and transport proteins (glycogenes). Recently, Montpetit et al. showed that the cardiac glycome (i.e., the complete set of glycan structures produced in the heart) varies between atria and ventricles, and changes differentially during development of each cardiac chamber [4]. Regulated expression of a single glycogene was sufficient to modulate action potential (AP) waveforms and gating of less sialylated Na_v consistently [3].

In addition to the evidence that a correctly regulated glycome is vital to normal cell function, aberrant glycosylation has dramatic effects on the cardiac function. There is a set of >40 distinct forms of inherited human diseases of reduced glycosylation known as Congenital Disorders of Glycosylation (CDG) caused, typically, by a mutation or deficiency in a glycogene which results in a relatively modest reduction in glycoprotein glycosylation [8, 9]. This variable but modest reduction in glycosylation among CDG subtypes causes a high infant mortality rate. Recently reported prevalence of cardiac involvement prompted experts to suggest screening for cardiac dysfunction in all CDG patients and for CDG in all young patients suffering from cardiomyopathy of unknown etiology. Together, the literature suggests that regulated and aberrant changes in glycosylation impact cardiac function.

However, little is known about how altered glycosylation will impact cardiac function at different organization levels, i.e., from ion channels to cells to tissues to the whole heart. Corroborating data that connects the changes in multi-scale cardiac systems is difficult without performing computer simulations. There is an urgent need to couple the wealth of data obtained from in-vitro and in-vivo experiments with in-silico models. Computer model overcomes practical and ethical limitations in the in-vivo experiments. In addition, it enables the prediction of causal relationships between normal or abnormal functions (e.g., glycosylation modulation dynamics) that in-vivo experiments alone cannot easily achieve.

Our objective is to investigate how changes in glycosylation influence the hERG (i.e., human ether-a-go-go related gene) ion channels and cardiac electrical signaling from cells to cables, and to tissues. In this present study, we developed in-silico models of cardiac cells and tissues to study the role of glycosylation in cardiac function. The hERG channel mediates the rapid delayed rectifying potassium current (I_{Kr}), which is partially responsible for late phase 2 and phase 3 of the AP, i.e., the repolarization of cardiac myocytes [10]. The "gain" or "loss" in the hERG channel function can potentially lead to the Short or Long QT syndromes [11]. Our contribution is to integrate the data from in-vitro experiments with in-silico models for predicting the effects of reduced glycosylation on cardiac function. The purpose of this article is to model the glycosylation effects on ion channels, and further predict its impacts at larger scales, i.e., from cells to tissues.

2.2   Multi-Scale Cardiac Modeling

Computer models facilitate the quantitative simulation, elucidation and understanding of cardiac function in health and disease. The need to integrate models and data across multiple biological scales has been widely recognized by biomedical and clinical researchers [12, 13]. This present investigation integrates glycosylation-channel interactions, obtained from the whole-cell

patch clamp experiments, with in-silico models to predict glycosylation modulation dynamics in hERG channels and cardiac electrical signals including ionic currents, action potentials, spiral waves, and ECG signals. The development of multi-scale cardiac models, i.e., hERG channel, cell, and tissues, is described as follows.

2.2.1 Model of hERG Channel

The hERG channel is widely modeled in two forms. One is the Hodgkin-Huxley (HH) type model, and the other is Markov state model. The HH type formulation typically describes the gating of hERG channel with two independent activation and inactivation variables, as shown in the following equations:

$$I_{Kr} = G_{Kr}\sqrt{\frac{K_o}{5.4}} X_{r1} X_{r2} (V - E_K)$$

$$X_{r1\infty} = \frac{1}{1 + e^{-\frac{(V - V_a)}{K_a}}} \qquad X_{r2\infty} = \frac{1}{1 + e^{\frac{(V - V_i)}{K_i}}}$$

where V is the trans-membrane action potential, K_o=5.4mM is the extracellular K+ concentration, E_K is the reversal potential, G_{Kr} is the conductance (nS/pF), $X_{r1\infty}$ is the steady-state activation, $X_{r2\infty}$ is the steady-state inactivation, V_a is the voltage of half-activation, V_i is the voltage of half-inactivation, K_a and K_i are slope factors.

Despite the popularity of HH-type descriptions, Markov models have become increasingly important in recent years. There are a number of Markov models developed with different states and structures, e.g., Wang et al. [14], Clancy and Rudy [15], Mazhari et al. [16], and Oehmen et al. [17]. In 2011, Bett et al. compared the HH type formulation with the aforementioned four Markov models. The conclusion is that hERG is best represented by a linear Markov model with 3 closed states, one open and one inactivated state [18]. Hence, we adopted the 5-state Markov formulations to model the gating of hERG channel. As shown in Figure 2-1, the Markov model

20

includes 3 closed states (C1, C2, C3), 1 inactivation (I) and 1 open (O) state. The transition rates ($\alpha's$ and $\beta's$) are voltage-dependent, i.e., $\alpha = a_i \times e^{b_i \cdot V}$ and $\beta = c_i \times e^{d_i \cdot V}$, wherer i is the index of transition rate parameters. The constants, Kf and Kb, describe the voltage insensitive transition in the gating of hERG channel. Ψ is defined as a function of other transition rates to ensure the microscopic reversibility [16, 18]. The hERG channel stays in the fully closed state (C1) during resting, and transfers to other states when excited. The initial value of C1 = 1, and others are 0.

$$I_{Kr} = G_{Kr} O (V - E_K)$$
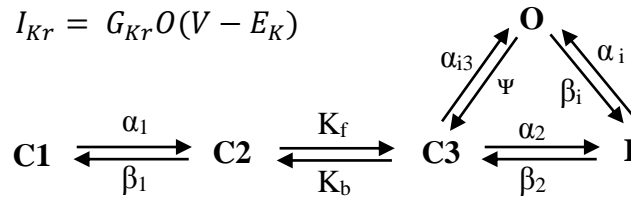
Figure 2-1 Structure of 5-state Markov model of hERG channel.

2.2.2 Model of Cardiac Myocyte

When a cardiac myocyte is stimulated, the states of ion channels (e.g., close, activation, inactivation) control the ability of the ions (e.g., Na^+, Ca^{++}, and K^+) to cross the membrane. The influx and efflux of ions generate electrical currents through the ion channels, and vary trans-membrane potentials. The cardiac cell is modeled as a structured electric circuit with capacitors, resistors and batteries. Specific to human ventricular cells, a number of models have been developed in the literature, e.g., Priebe and Beuckelmann model [19], ten Tusscher-Panfilov 2004 model [20] and the updated 2006 model [21], Iyer et al. model [22], Grandi et al. model[23], and O'Hara et al. model [24].

In this present investigation, we utilized ten Tusscher-Panfilov 2006 model to describe the electrophysiological behaviors of human ventricular myocytes [21]. The justification is that the results of ten Tusscher-Panfilov 2006 model best match our wild-type data (i.e., full glycosylation)

21

from in-vivo experiments. The major updates from the ten Tusscher-Panfilov 2004 model to the 2006 version are the inclusion of more detailed description of intracellular Ca^{++} dynamics and subspace Ca^{++} dynamics, as well as the revisions of fast and slow voltage inactivation gate in I_{CaL}.

The endocardial-cell version of ten Tusscher-Panfilov 2006 model is used to simulate the AP (V) with the following ordinal differential equation:

$$-C_m \frac{dV}{dt} = I_{to} + I_{Ks} + I_{Kr} + I_{K1} + I_{NaCa} + I_{NaK} + I_{pK} + I_{pCa} + I_{bCa}$$

$$+ I_{bNa} + I_{Na} + I_{CaL} + I_{stim}$$

where t is time, C_m is the cell capacitance per unit surface area, I_{stim} is the external stimulus current which activates the cell from the resting state. The transmembrane currents include transient outward current (I_{to}), slow delayed rectifier K^+ current (I_{Ks}), rapid delayed rectifier K^+ current (I_{Kr}), inward rectifier current (I_{K1}), Na^+/Ca^{++} exchange current (I_{NaCa}), pump current (I_{NaK}), plateau currents (I_{pK}, I_{pCa}), background currents (I_{bCa}, I_{bNa}), fast Na$^+$ current (I_{Na}) and L-type Ca^{++} current (I_{CaL}). Most of these voltage-gated ionic currents are modeled in the form of cell conductance, membrane potential gradients and channel gate dynamics. The details of all ion-channel kinetics can be found in references [20, 21]. All parameters and initial values are the same as given in the ten Tusscher-Panfilov 2006 model. Note that we replaced the HH type model of I_{Kr} with the 5-state Markov model. The G_{Kr} is the same as the original value in ten Tusscher-Panfilov model. We optimally calibrated the 5-state Markov model to fit the in-vivo data of four glycosylation conditions from our in-vivo experiments.

2.2.3 Model of Cardiac Tissue

The cardiac cell is not an independent unit. Each depolarized cell can stimulate neighboring cells and trigger cell-to-cell conductions. In the rapid depolarization phase, the overshoot of Na^+ ions causes a resting-to-depolarizing Na^+ gradient and drives the flow of Na^+ through gap

junctions that stimulates adjacent cells. The influx of Na^+ causes neighboring cells to reach threshold potential and initiates the depolarization phase of the AP. As the depolarization and repolarization propagate among cells, electrical waves are generated. This cell-to-cell conduction is analogous to a circuit system with resistances and capacitors. As shown in Figure 2-2, the consecutive cell connections are modeled as linear fiber (cable) and tissue (cell array). The 1D linear cable is composed of 600 cells, and a stimulus is given at cell 1. The linear strand of cells (i.e., cable) is modeled using the following mono-domain reaction-diffusion equation:

$$\frac{\partial V}{\partial t} = -\frac{1}{C_m}(I_{ion} + I_{stim}) + \frac{1}{\rho S C_m}\frac{\partial^2 V}{\partial x^2}$$

and in 2D tissue, the equation is:

$$\frac{\partial V}{\partial t} = -\frac{1}{C_m}(I_{ion} + I_{stim}) + \frac{1}{\rho S C_m}\left(\frac{\partial^2 V}{\partial x^2} + \frac{\partial^2 V}{\partial y^2}\right)$$

where I_{ion} is the sum of trans-membrane ion currents, $\rho = 180\Omega cm$ is the cellular resistivity, $S = 0.2\ um^{-1}$ is the surface-to-volume ratio, and $C_m = 2\ uF/cm^2$ is the cell capacitance.

To simulate the propagation of cardiac electrical waves along 1D fiber, reaction-diffusion equations are numerically solved with the finite-difference scheme. The action potential can be calculated as:

$$V_i^{t+dt} = -\frac{dt}{C_m}(I_{ion} + I_{stim}) - \left(\frac{2q}{C_m} - 1\right)V_i^t + \frac{q}{C_m}(V_{i-1}^t + V_{i+1}^t)$$

where $q = \frac{dt}{\rho S dx^2}$ is the same for all cells. Neuman boundary condition was assumed in the simulation of 1D cardiac cable, i.e. $V_{101}^t = V_{99}^t$ and $V_0^t = V_2^t$ at the boundaries. The numerical finite-difference scheme for 2D tissue is formulated as:

$$V_{i,j}^{t+dt} = -\frac{dt}{C_m}(I_{ion} + I_{stim}) - \left(\frac{4q}{C_m} - 1\right)V_{i,j}^t + \frac{q}{C_m}(V_{i-1,j}^t + V_{i+1,j}^t + V_{i,j-1}^t + V_{i,j+1}^t)$$

where no flux boundary condition is assumed to ensure there are no current leakages on the borders.

23

Cable:
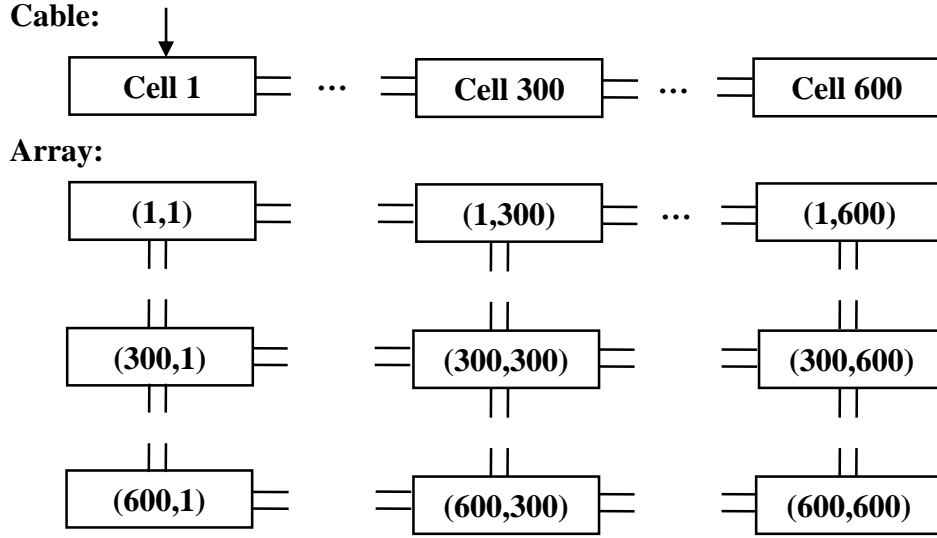
Figure 2-2 Structures of 1D fiber and 2D tissues.

2.2.4 ECG Derivation

The ECG signal provides a system-level view of cardiac electrical activity, which is an important clinical diagnostic tool. The standard lead I, II and III (i.e., Einthoven's triangle) measure difference in potentials between electrodes placed on left arm, right arm and left leg [25]. In this study, 3-lead ECG signals are measured using 3 virtual electrodes in an equilateral triangle on 2D tissues. The ECG will be used to evaluate and quantify whether and how altered glycosylation affects cardiac electrical conduction. In this investigation, the electrodes were placed at a distance of 6 cm above 2D tissues with no-flux boundary conditions. The potential at each electrode is calculated using the following equation:

$$\emptyset = \iint_S \frac{I_{ion}}{r} \, dxdy$$

where S is the area over cardiac tissue, i_{ion} is the transmembrane currents, x and y represent the coordinates of cells on 2D tissue, and r is given as:

$$r = \sqrt{(x - x_E)^2 + (y - y_E)^2 + z_E{}^2}$$

24

where $E = (x_E, y_E, z_E)$ is the location of the electrode. The I_{ion} current is obtained with the following equation:

$$I_{ion} = \frac{1}{\rho S C_m} \left(\frac{\partial^2 V}{\partial x^2} + \frac{\partial^2 V}{\partial y^2} \right)$$

Lead I, II, III ECG signals are the potential differences between two electrodes as:

$$ECG(E_1, E_2) = \emptyset(x_{E1}, y_{E1}, z_{E1}) - \emptyset(x_{E2}, y_{E2}, z_{E2})$$

It may be noted that 60° orientation is considered between each two leads.

2.3 Materials and Experimental Design

2.3.1 Physical Experiments

We recently reported the effects of differential glycosylation on the gating of hERG ion channels, showing that N-glycosylation effectively limits the hERG activity [26, 27]. The in-vitro experimental data were collected from hERG-expressing CHO cells under 4 glycosylation conditions, i.e., full glycosylation (n = 11), reduced sialylation (n = 11), mannose-rich glycosylation (n = 6) and N-Glycanase treated (n = 6). Steady-state gating parameters were examined with the use of standard pulse protocols and solutions described by the Bennett lab [26].

Steady State Activation (SSA) protocol is described as follows. Cells were held at -80 mV, stepped to more depolarized potentials (-80 mV to +40 mV in 10 mV increments) for 4 seconds, then stepped back to -50 mV for another 4 seconds, and returned to the holding potential. Steady-state conductance values (G) were calculated using ohm's law $G = I/(V_p - E_K)$, where I is the peak of tail currents elicited at each test potential (V_p). The maximum conductance generated by each cell was used to normalize the data for each cell to its maximum conductance by fitting the data to a single Boltzmann distribution as:

$$\text{Fraction of maximal conductance} = [1+\exp(-(V-V_a)/K_a)]^{-1}$$

where V is the membrane potentials, V_a is the half-activation potential, K_a is the slope factor. The normalized data were averaged with those from the other cells to calculate the resulting average G-V curves.

Steady state inactivation (SSI) is measured following a conventional protocol. Cells were held at -80 mV before stepping to +20 mV for 3 seconds. Then we stepped to -120 mV to +60 mV (in 10 mV increments) for 30ms before stepping back to +20 mV for 1 second and then returned to the resting potential. The maximum current generated by each cell was used to normalize the data for each cell to its maximum current by fitting the data to a single Boltzmann distribution, from which the mean Vi ±SEM and Ki ±SEM values were determined.

$$\text{Fraction of maximal current} = [1+\exp((V-V_i)/K_i)]^{-1}$$

where V is the membrane potential, Vi is the voltage of half-inactivation, Ki is the slope factor. Table 2-1 shows the mean ± SEM SSA and SSI parameters measured under four glycosylation conditions, as reported by us previously [26] . These changes in hERG channel gating were used to calibrate in-silico models, which further predict glycosylation effects on cardiac electrical signaling of cells and tissues.

Table 2-1 hERG channel activation and inactivation parameters [26].

hERG Channel	n	V_a(mV)	K_a(mV)	V_i(mV)	K_i(mV)
Full Glycosylation	11	-22.0±1.3	8.4±0.3	-74.4±4.9	-19.0±0.8
Reduced Sialylation	11	-13.7±2.4	8.6±0.4	-56.2±5.3	-17.2±1.3
Mannose-Rich	6	-12.6±2.4	8.9±0.4	-51.48±3.6	-16.4±0.9
N-Glycanase treated	6	-12.1±2.2	8.9±0.9	-58.5±5.9	-20.3±1.2

2.3.2 Computer Experiments

Recall that we modeled the hERG channel with a 5-state Markov formulation, as opposed to the traditional HH type formulation. First, the Markov model was calibrated and fitted to

glycosylation data from in-vivo experiments (see Table 2-1). The sensitivity analysis is performed to establish model parameters that maximally influence the output for each protocol. Furthermore, the algorithm of nonlinear constrained optimization is used to find the parameter values minimizing the sum of the least-square errors between model predictions and experimental data in glycosylation. Pulse protocols used in in-silico models are the same as in in-vivo experiments. Second, we simulated and compared the variations of I_{Kr} currents and APs for four glycosylation conditions. The glycosylation-induced variations in hERG channels were modeled to predict the changes of I_{Kr} magnitudes and action potential durations (APDs). Third, cardiac cells were connected by gap junctions in a linear fiber, i.e., cable, to predict the glycosylation effects on AP propagation, assuming that altered glycosylation impacts hERG channel gating only. The inhomogeneous cable contains 600 cells, in which 300 cells are fully glycosylated and the other 300 cells are under one of three conditions of reduced glycosylation (i.e., reduced sialylation, mannose-rich, or N-Glycanase treated)., Further, we measured the APD restitution curves for 4 glycosylation conditions in the 1D cable of cardiac cells. Finally, we construct the model of 2D tissues by arranging cardiac cells in an array (see Figure 2-2). Glycosylation effects on the rectilinear and spiral waves were predicted using in-silico simulation models. In addition, ECG signals were derived to characterize the variations of cardiac electrical conduction between full glycosylation and reduced glycosylation.

In the single cell, we used a 2-ms 38 pA/pF stimulus current (I_{stim}) applied at a frequency of 0.5~2 Hz to trigger simulated APs. The I_{Kr} currents and AP were obtained after at least 100 cycles when the cell reached steady states. The variable temporal resolution is used in the single-cell simulation. In the linear cable, the I_{stim} amplitude of 52 pA/pF and spatial resolution Δx=0.25mm were used to generate the electrical waves. In addition, APD restitution curve is quantified with

the S1-S2 protocol. The left of the cable is paced at a basic cycle length of 1000ms with the S1 stimulus until steady-state is reached and is then perturbed by a stimulus (S2) after waiting a variable-length interval. (3) In the 2D tissues, the I_{stim} amplitude is twice the diastolic threshold, i.e., 52pA/pF. The spatial resolution Δx is 0.04cm, and the temporal resolution Δt is 0.02ms. The spiral wave was initiated by applying a first stimulus (S1=2ms) along one side of the tissue to generate a rectilinear wave propagating toward the other side. When the refractory tail of electrical waves reaches the middle, a second stimulus (S2=5ms) will be given in the middle of the tissue, paralleling to the first rectilinear wave covering only 3/4 of the length of the tissue [21].

Table 2-2 Numerical accuracy of APD and CV at different Δx and Δt.

Δx(cm)	Δt = 0.01 ms		Δt = 0.02 ms	
	APD (ms)	CV (cm/s)	APD (ms)	CV (cm/s)
0.02	323.00	71.38	322.98	69.89
0.025	322.96	69.44	322.94	68.10
0.03	322.94	67.43	322.92	66.26
0.035	322.94	65.31	322.92	64.31
0.04	322.94	63.06	322.92	62.23

We measured the CVs at different spatial and time resolutions for four glycosylation conditions on a cable of 600 cells. Note that Table 2-2 does not include the CVs and APDs for different glycosylation conditions. This is because I_{Na} is the main contributor to excite a cardiac cell and trigger electrical conduction. In this investigation, we assumed that only hERG channels have altered glycosylation and all other channels (including Na^+ channel) remain unchanged. In the 1D cable, the CVs are primarily controlled by the front of the waves (i.e., I_{Na} current). Hence, in-silico experiments show that CVs are approximately the same for different glycosylation conditions at the same Δx and Δt. However, when electrical waves propagate in the tissues, not

28

only the front of the waves, but also the back of the waves (i.e., refractory period) could affect the

conduction. This will be shown later in the section of results of spiral waves.

Here, the APD and CV decrease slightly when Δx increase from 0.02cm to 0.04cm at both time

steps. When Δt increases from 0.01ms to 0.02ms, there is a slight decrease in both APD and CV.

These small variations are mainly due to the approximation errors in the numerical analysis. The

models of cardiac cell and tissue are solved with the use of Ode15s solver and explicit finite

difference methods. Computer models were implemented using Matlab R2010a and Simulink v7.5

software from MathWorks (Natick, MA, USA) in a Windows 7 (Microsoft, Redmond, WA, USA)

64-bit machine.

2.4   Results and Discussions

2.4.1 Glycosylation Modulation of hERG Channel

Table 2-3 Markov state transition rates under four glycosylation conditions.

	Full glycosylation	Reduced Sialylation	Mannose-rich	N-Glycanase
α_0	0.0312·exp(0.0165V)	0.018633·exp(0.0234V)	0.0199·exp(0.0254V)	0.0173·exp(0.022V)
β_0	0.0993·exp(-0.0269V)	0.0413·exp(-0.03533V)	0.0469·exp(-0.0385V)	0.0364·exp(-0.0318V)
α_1	0.0036·exp(0.0221V)	0.0024·exp(0.0210V)	0.0025·exp(0.0225V)	0.0023·exp(0.0195V)
β_1	0.0003·exp(-0.0088V)	1.55E-4·exp(-0.0195V)	1.55E-4·exp(-0.0209V)	1.48E-4·exp(-0.0181V)
α_i	0.0127·exp(-0.0343V)	0.0274·exp(-0.0357V)	0.0293·exp(-0.0393V)	0.0250·exp(-0.0320V)
β_i	0.4916·exp(0.0065V)	0.4660·exp(0.0048V)	0.5771·exp(0.0063V)	0.3458·exp(0.0032V)
α_{i3}	8.04E-5·exp(3.86E-7V)	1.53E-6·exp(6.34E-7V)	1.54E-6·exp(6.47E-7V)	1.53E-6·exp(6.2E-7V)
K_f	0.0262	0.0296	0.0321	0.0272
K_b	0.1478	0.2136	0.2297	0.1972

Markov model of hERG channels is optimally calibrated to reproduce the in-vitro data from the

whole-cell voltage clamp experiments. Note that the SSA and SSI curves were obtained using the

same pulse protocol from simulated currents as well as from in-vitro experiments (see Figure 2-3).

First, we performed the sensitivity analysis on the Markov model to identify transition rates that

29

maximally impact the in-silico data for each pulse protocol. Second, a constrained nonlinear optimization algorithm, i.e., trust-region-reflective [28], is employed to identify the parameters of transition rates. The objective function is to find optimal parameter values that minimize the sum of the least-square errors between in-silico and in-vivo data. Note that the parameter values from Mazhari et al. [16] were used as initial guesses in the minimization procedure. A full list of the parameters of transition rates under 4 glycosylation conditions is reported in Table 2-3.

Figure 2-3 shows the fitted SSA and SSI relationships of hERG under four glycosylation conditions. Note that the SSA and SSI curves are shifted rightward (5~15mv) to more hyperpolarized potentials. In other words, N-glycans limits hERG voltage-dependent activation and inactivation by shifting the half-activation voltage of hERG to more depolarized potentials (see Table 2-3 for parameter values). Thus, changes in glycosylation modulate the voltage-dependent gating behaviors of hERG ion channels.
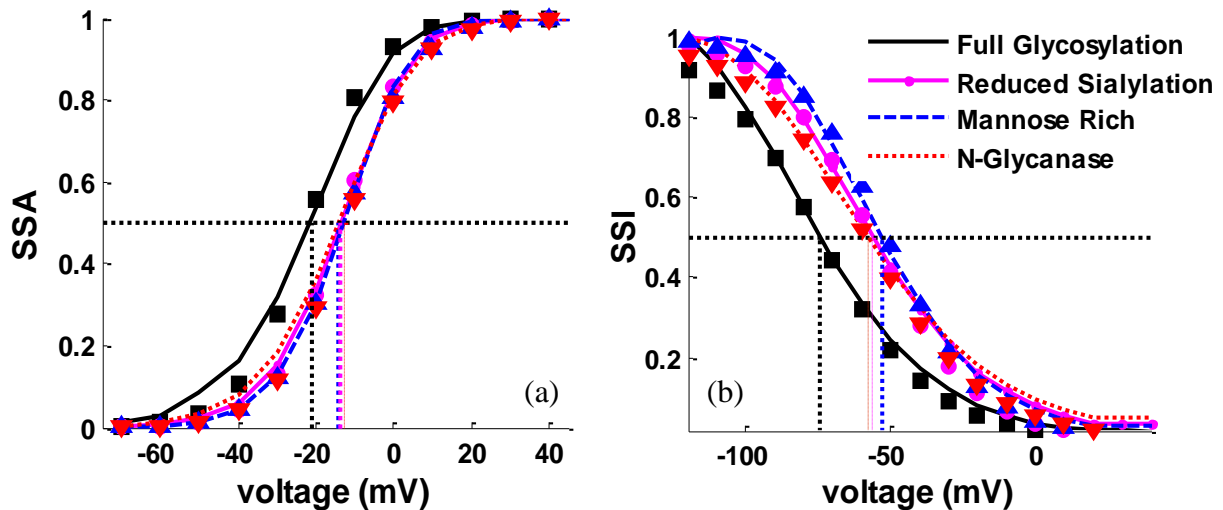
Figure 2-3 The hERG channel gating and kinetics under four glycosylation conditions. (a) Steady-state activation (b) Steady-state inactivation. (In-vitro data as reported by us previously [26]: ■ Full Glycosylation ●Reduced Sialylation▲Mannose Rich▼N-Glycanase, In-silico data from the Markov model: straight and dashed lines).

2.4.2 Reduced Glycosylation Modifies I_{Kr} and Shortens APD

The measured shifts in SSA and SSI with changes in glycosyaltion would likely modulate I_{Kr} during the repolarization phases of the AP. Further, we integrate glycosylation-channel interactions (see Figure 2-3 from the whole-cell patch clamp experiments) with the in-silico model of cardiac cell to predict whether and how reduced glycosylation will impact the I_{Kr} currents and action potentials. As shown in Figure 2-4, the I_{Kr} current is shifted leftward along the time axis with earlier and higher current densities under 3 reduced glycosylation conditions (i.e., reduced sialylation, mannose-rich, and N-Glycanase). When hERG channels recover from the inactivation to the activated state, the repolarized cell will decrease the AP from the peak value to resting potential. As shown in Figure 2-4, the N-Glycanase treated cell has a early peak in the I_{Kr} current along the time axis. This indicates the efflux of potassium current occurs earlier (i.e., repolarization) in Phases 2 and 3 of AP. It may also be noted that mannose-rich and reduced sialylation treated cells have similar I_{Kr} spike shapes except the former has a higher peak in Figure 2-4. The larger rightward shift in SSI curve measured for the mannose-rich conditions (See Figure 2-3 b) are likely responsible for this higher peak. In other words, hERG channels under mannose-rich conditions would recover from inactivation at more depolarized potentials during the AP, therefore the hERG channel would be more active during the AP, causing an increased K^+ efflux.

Figure 2-5 shows that reduced glycosylation shortens the action potential duration (APD), and the N-Glycanse treated cell yields the shortest APD. When K^+ efflux increases, the transmembrane potential decreases quickly and the cell repolarizes to the resting potential more quickly. Reduced glycosylation promotes an earlier/higher I_{Kr} peak, thereby leading to a faster repolarization and a shortened APD. (see Figure 2-5). In addition, we validated the results from in-silico models by measuring hERG current in CHO cells treated with N-Glycanase and under

conditions of full glycosylation. As shown in Figure 2-6, in-vitro I_{Kr} currents [26] match the simulated I_{Kr} curves in major characteristics (e.g., leftward shifted and higher amplitude in the N-Glycanase treated conditions), but with more random variations in the in-vitro data.
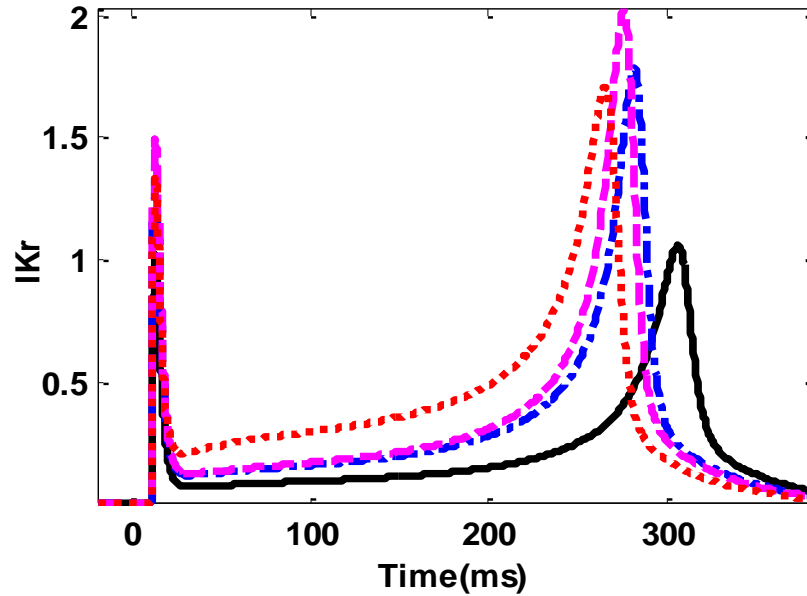
Figure 2-4 Predicted rapid delayed rectifier K$^+$ current (I_{Kr}).
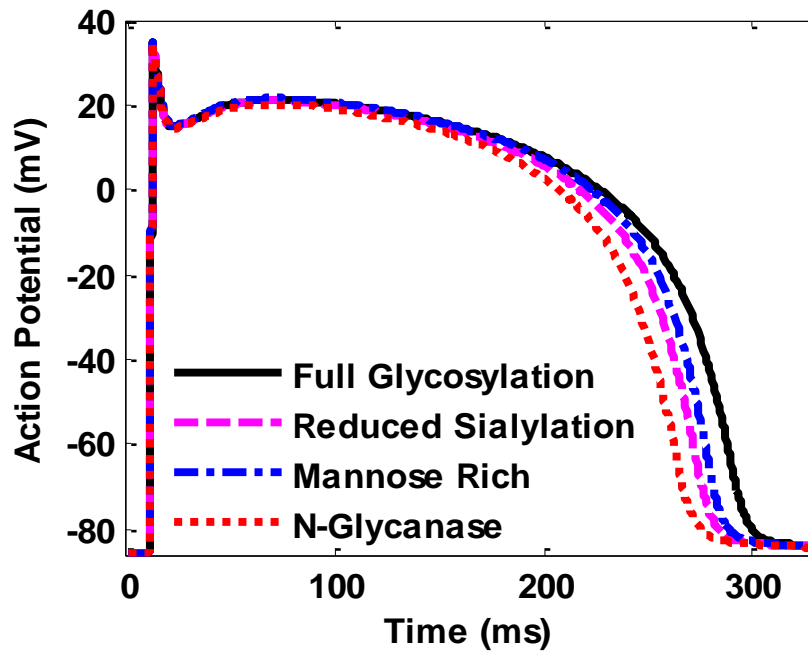
Figure 2-5 Human ventricular action potential under four glycosylation conditions.
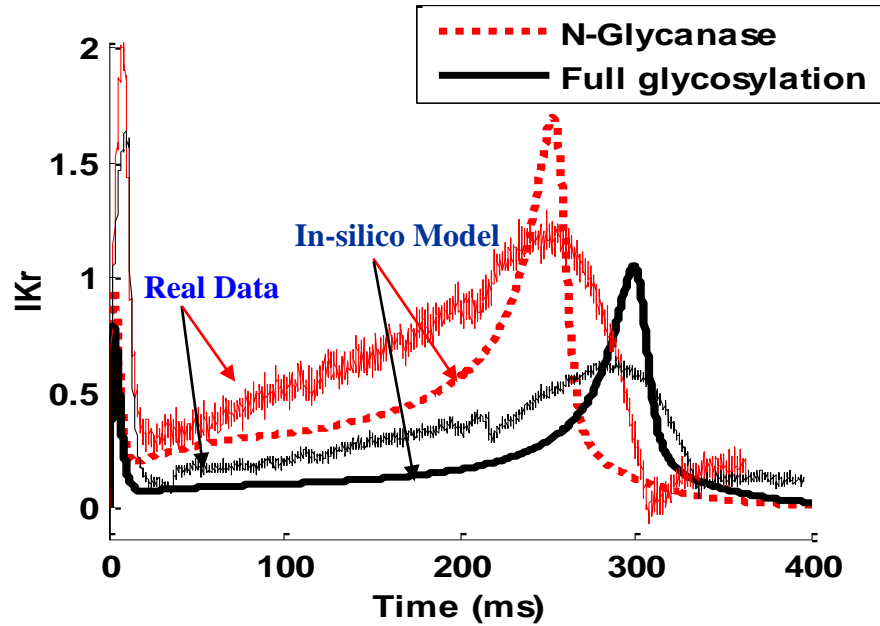
Figure 2-6 Comparison between in-vitro and simulated I_{Kr} currents.

2.4.3 Reduced Glycosylation Affects the APD Restitution in A Single Cell

We measured the APD restitution with the S1-S2 restitution protocol. The cell is paced at a basic cycle length (BCL) with the S1 stimulus until steady-state is reached and is then perturbed by a stimulus (S2) after waiting a variable-length interval. In our experiments, S1 stimulus is applied for 30 cycles to reach the steady state. Also, two different BCLs, i.e., 1000ms and 2000ms were used. Both S1 and S2 stimulus are 1ms duration and 38pA/pF amplitude.

Figure 2-7 a and b shows the APD_{90} restitution curves $APD_{n+1} = f(DI_n)$ at the BCL of 1000ms and 2000ms, respectively. Note that the BCL of 1000ms yields a similar shape of APD_{90} restitution curve as the 2000ms. The APD increases with the DI, and the reduce glycosylated cell has smaller APD_{90} than the fully glycosylated one. However, there is a negative slope ($df/d(DI) =< 0$) at small DIs, i.e., 15ms~22ms (see Figure 2-7a) for the BCL of 1000ms. For the BCL of 1000ms, the minimal DI is 74.56ms, 73.16ms, 73.75ms and 70.69ms respectively for full glycosylation,

reduced sialylation, mannose rich and N-Glycanase. The minimal DI is calculated when the slope of APD$_{90}$ restitution curve reaches 1 (i.e., $df/d(DI) = 1$). Note that the minimal DI interval in the condition of full glycosylation is the largest. Similar results were obtained for the BCL of 2000ms. The minimal DI interval is slightly smaller, i.e., 71.89ms, 64.29ms, 68.23ms and 64.74ms respectively for full glycosylation, reduced sialylation, mannose rich and N-Glycanase.
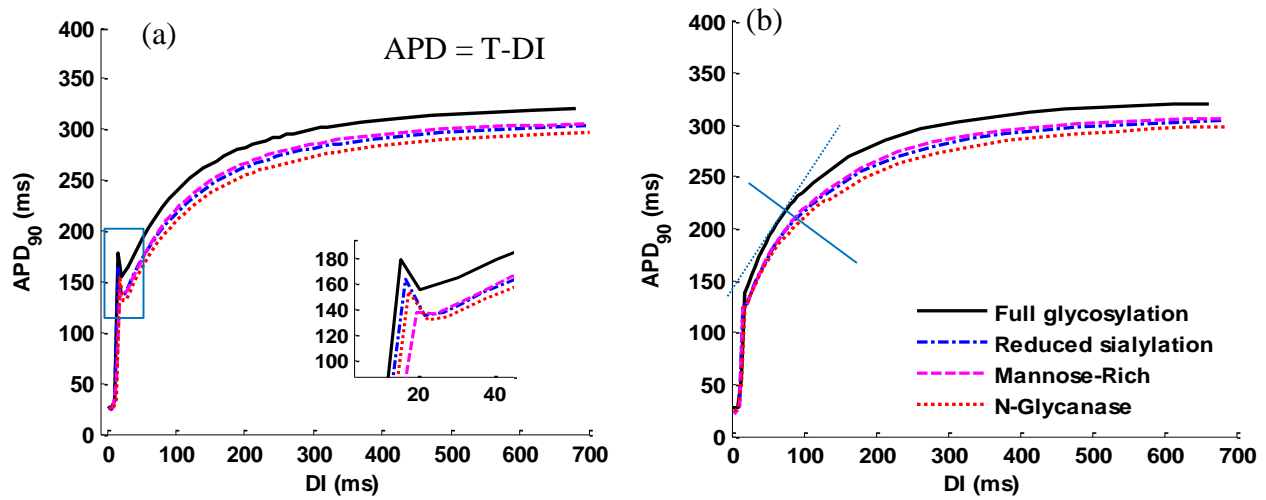
Figure 2-7 Single-cell action potential duration (APD) restitution curves. The cell is stimulated with the pacing rates of 1Hz (a) and 0.5Hz (b).
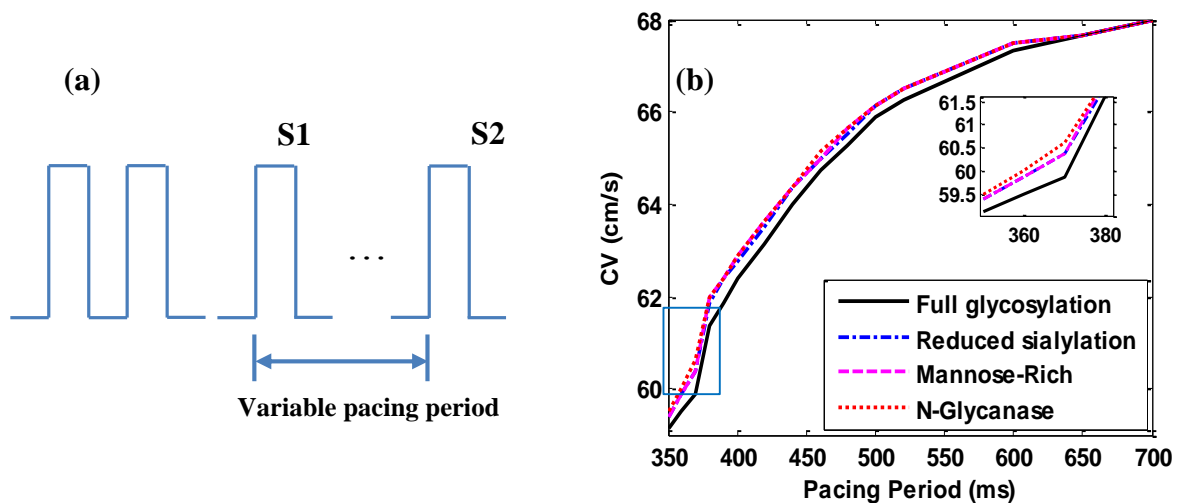
Figure 2-8 Protocol and CV restitution of 1D cable. (a) The experimental protocol, (b) CV restituion of 1D cable at Full Glycosylation, Reduced Sialylation, Mannose Rich and N-Glycanase.

34

2.4.4 Conduction Velocity

We measured the conduction velocity (CV) restitutions on 1D cables composing of 1400 cells. The S1-S2 protocol used is similar to the one in the APD restitution of 1D cable. As shown in Figure 2-8, we varied the pacing period between S1 and S2 stimulus to investigate the impact on the CVs. Note that the CVs increase when the pacing period increase, and tend to be the same for four glycosylation conditions when the pacing period is > 650ms. However, when the pacing period <650ms, the CVs for full glycosylation are smaller than others. This is because the refractory period is larger for fully glycosylation condition. Also, when the pacing period is < 370ms, the CVs of reduced sialylation and mannose rich are smaller than the N-Glycanase. The minimal pacing period (i.e., if smaller than this interval, electrical waves cannot be stimulated) is 350ms, 340ms, 342ms and 338ms respectively for full glycosylation, reduced sialylation, mannose rich and N-Glycanase.

2.4.5 Reduced Glycosylation Affects I_{Kr} Magnitudes, APDs at Different Pacing Rates, and APD Restitution in A Cardiac Cable

Figure 2-9 shows the variations of I_{Kr} currents (peak currents) of four glycosylation conditions at different pacing rates in a linear cable of cardiac cells. In our experiments, 600 cardiac cells are connected to form a cell cable. The first cell in the cable is stimulated. The I_{Kr} for the 200th cell are collected in the steady state. In order to make sure the stability, computer experimental results are collected after the first cell is stimulated for at least 20 times. As shown in Figure 2-9, the I_{Kr} magnitude decreases 30.98%, 26.08%, 17.37% and 32.73% when the pacing period increases from 400ms to 2000ms for full glycosylation, reduced sialylation, mannose rich and N-Glycanase, respectively. However, the differences of I_{Kr} magnitudes are bigger between four glycosylation conditions for the larger pacing period, i.e., 1000ms-2000ms (see Figure 2-9).
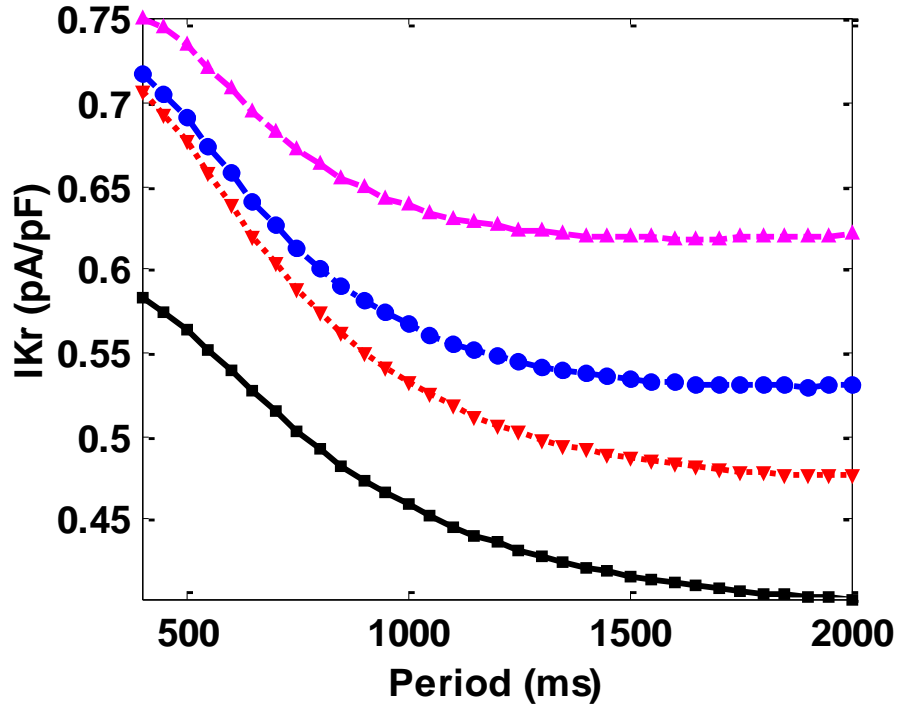
Figure 2-9 The variations of I_{Kr} magnitudes in 1D cable. The peaks of I_{Kr} currents are measured with respect to different pacing periods under the conditions of Full Glycosylation, Reduced Sialylation, Mannose Rich and N-Glycanase.

Figure 2-10 shows the variations of APDs of four glycosylation conditions, i.e., Full Glycosylation, Reduced Sialylation, Mannose Rich and N-Glycanase, at different pacing rates in a linear cable of 600 cells. Similarly to the experiments of I_{Kr} currents, the first cell in the cable is stimulated. The APDs for the 200th cell are collected in the steady state (i.e., after the first cell is stimulated for at least 20 times). Modeling results shows that APD$_{90}$ increases when the pacing period increases from 400ms to 2000ms (see Figure 2-10). Note that APD$_{90}$ differences decrease among 3 reduced glycosylation conditions when the pacing period increases. However, if we compare reduced glycosylation with full glycosylation, the effect to shorten the APD$_{90}$ is the same for different pacing periods (see Figure 2-10). It may also be noted that the APD$_{90}$ differences among 3 reduced glycosylation conditions vanish when the pacing periods is greater than 1500ms.
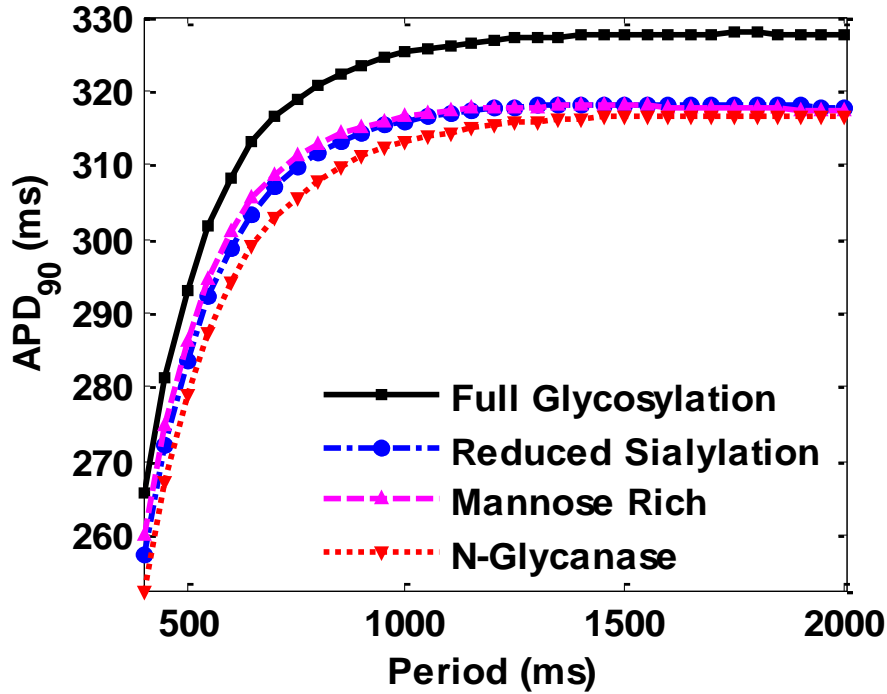
Figure 2-10 The variations of APDs in 1D cable. APDs are measured at different pacing periods under the conditions of Full Glycosylation, Reduced Sialylation, Mannose Rich and N-Glycanase.

We also measured APD restitution $APD_{n+1} = f(DI_n)$ for a linear cable of 600 cells with the S1-S2 restitution protocol (see details in Section 2.3, computer experiments). Note that the experiments of APD restitution not only quantify the effects of glycosylation on the minimal diastolic interval (DI), but also potentially indicate the stability of spiral waves. In other words, the slope of APD restitution curve provides potential information on the alternans or breakups of spiral waves [28]. In our experiment, S1 stimulus is applied in the first cell for 20 cycles at the basic cycle length (BCL) of 1000ms to reach the steady state. The APD$_{90}$ restitution curve for the 200th cell is collected. As shown in Figure 2-11, the APD increase with DI. The slope of APD restitution curve are greater than or equal to 1 (i.e., $df/d(DI) \geq 1$) for four glycosylation conditions. This indicates that reduced glycosylation does not increase the probability of spiral wave breakups. In addition, the minimal DIs that elicit a propagating action potential are 99.02ms,

99.44ms, 99.58ms and 99.40ms for full glycosylation, reduced sialylation, mannose rich and N-Glycanase, respectively. Note that the minimal DI in tissues is often larger than a single cell because of the effects of cell coupling and electrical conduction.
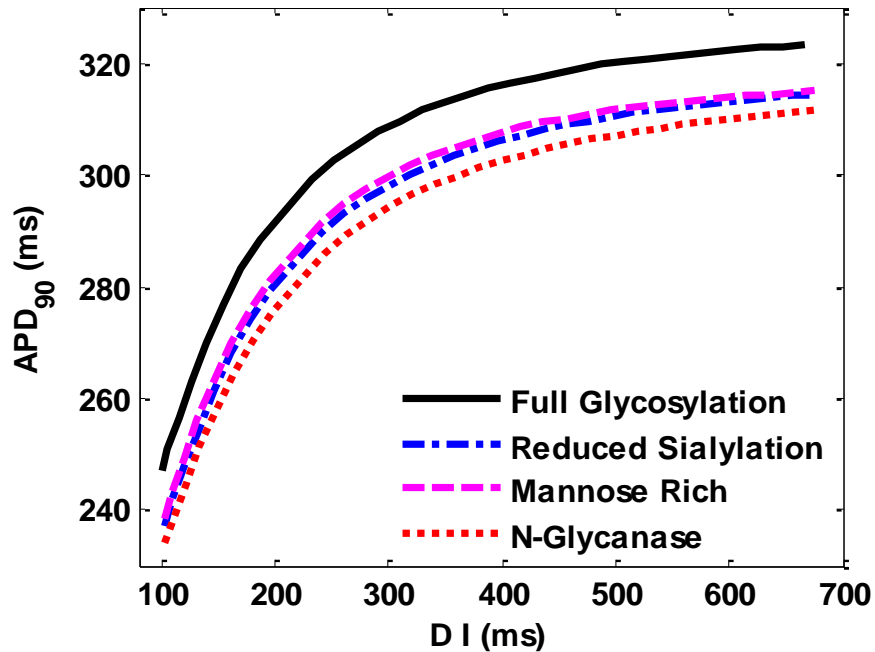
Figure 2-11 The APD restitution curve of 1D cable.

2.4.6 Reduced Glycosylation Affects the AP Propagation in the Inhomogeneous Cable

Repolarization heterogeneity can potentially cause inhomegeneous electrical wavelength in cardiac fibers. As depicted in Figure 2-12 a-c, we connected 600 inhomogeneous ventricular cells with gap junctions in a linear cable. The first 300 cells are fully glycosylated and the next 300 cells are under one of the following conditions: reduced sialylation (a), mannose-rich (b), or N-Glycanase (c). The stimulus is initiated in the first cell, then adjacent cells are consecutively excited until electrical waves are conducted to the end of the tissue. The abruptions in electrical waves indicate the heterogeneity of APD between fully glycosylated cells and less glycosylated cells. Such a repolarization heterogeneity may potentially increase the risks of cardiac arrythmia.

The comparisons under those conditions are presented in Figure 2-12 d-f, which represent the differences between the inhomogenous cables (see Figure 2-12 a-c) and a homogenous cable, i.e., fully glycosylated. The N-Glycanase treated cable is shown to have the most significant abruptions in electrical wave conductions. Experimental results are consistent with predicted effects on cardiac electrical signaling based on multi-scale modeling of hERG ion channel, cardiac cells and tissues (i.e., cable). Reduced glycosylation modulates the gating of hERG channels, shortens the APD of cardiac cell, and affects the AP repolarization in cardiac cable. If periodic stimuli are applied, reduced glycosylation can also potentially vary electrical propagation in a linear cable of cells.
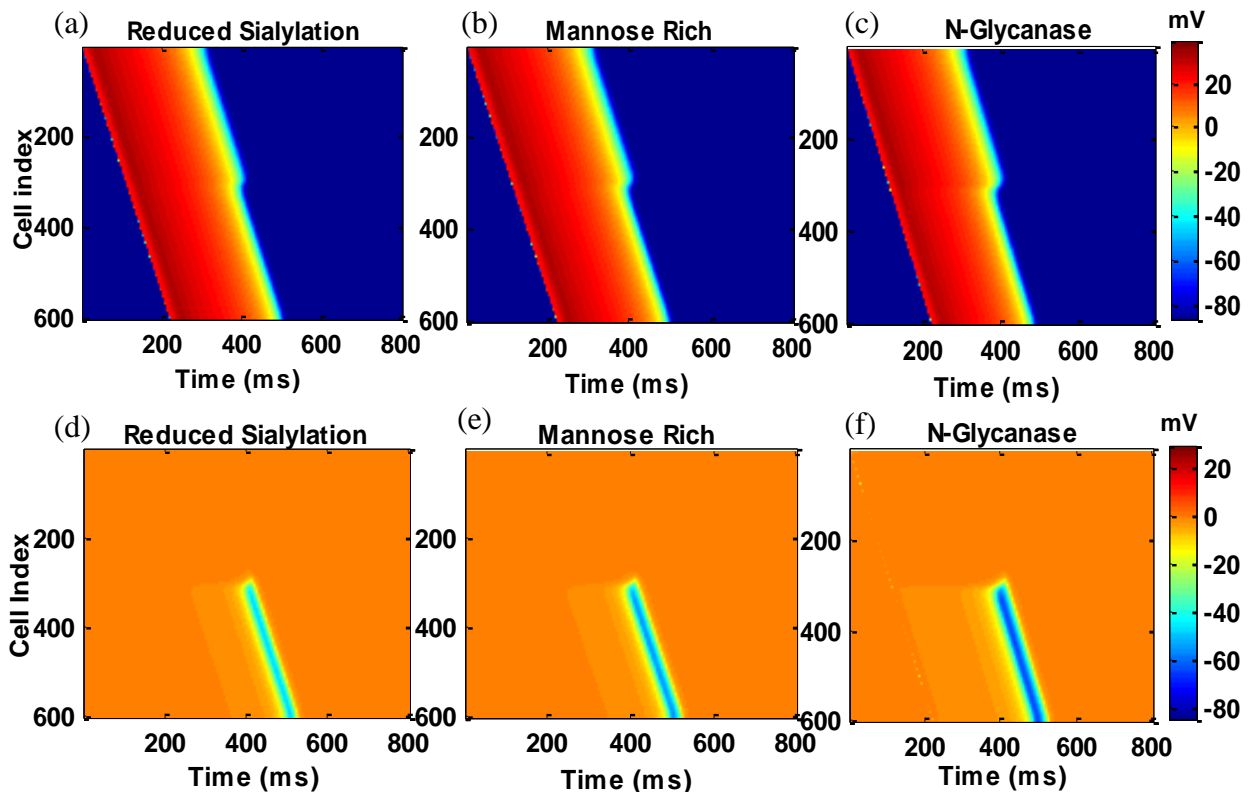
Figure 2-12 AP propagation along a 1D inhomogeneous cable with 600 cells.The first 300 cells are fully glycosylated and the second 300 cells are under the reduced glycosylation conditions: (a) Reduced Sialylation, (b) Mannose Rich, and (c) N-Glycanase. The comparison plots (d-f) represent the differences between (a-c) vs. a Fully Glycosylated cable.

2.4.7 Reduced Glycosylation Affects Electrical Conduction in 2D Cardiac Tissues

Little is known about how reduced glycosylation affects electrical conduction in 2D cardiac tissues [29]. Most previous work focused on glycosylation modulation effects at the levels of ion channels (e.g., sodium and potassium channels) and cells. Note that electrical conduction may produce either non-spiral or spiral waves in 2D tissues.

Non-spiral waves often represent normal cardiac electrical conductions. The stimulus (i.e., 52 pA/pF) is applied along the entire left edge of the tissue, and electrical waves propagate toward the right side (see Figure 2-13a). Because there are no potential gradients in the perpendicular direction, this type of electrical propagation in 2D tissues is similar to the 1D cable.

However, spiral waves are modeling reentrant cardiac arrhythmias. The reentry on 2D tissue was generated using the pulse protocols that are introduced in Section 2.3 – Computer Experiments. As shown in Figure 2-13, three virtual electrodes were placed at the locations as follows: $E_1(60, 60, 60)$, $E_2(60, 600, 60)$, $E_3(600, 330, 60)$. The 3-lead ECG signals were derived to quantify the effects of reduced glycosylation on electrical conductions.
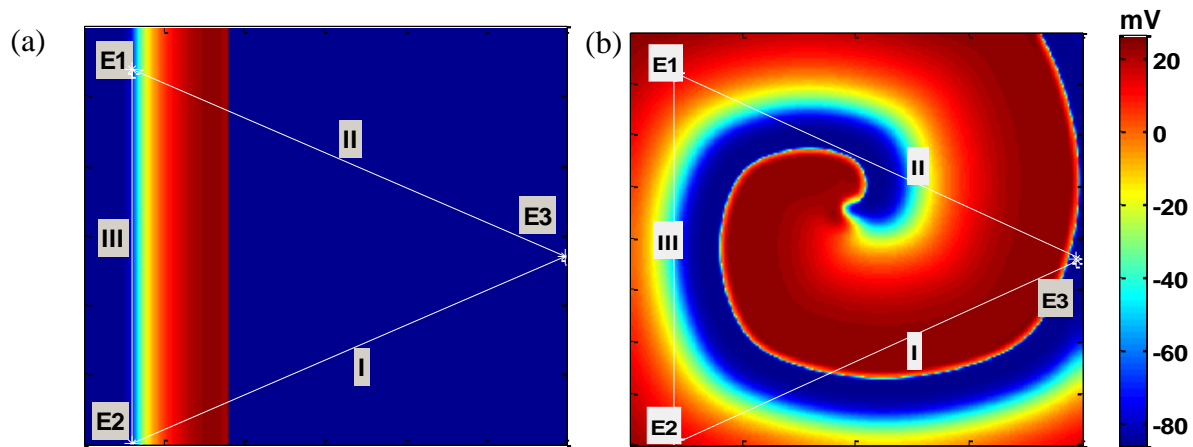
Figure 2-13 The propagation of rectilinear waves and spiral waves in 2D cardiac tissues. Three virtual electrodes are placed at E_1, E_2 and E_3. The 3-lead ECGs are derived based on the potential differences between two electrodes.

First, we simulated the propagation of normal electrical waves (i.e., rectilinear waves in Figure 2-13a) in fully glycosylated and N-Glycanase treated ventricular tissues, assuming that only hERG channel gating is impacted by changes in glycosylation. As shown in Figure 2-14a, lead I, II, III ECG signals capture electrical conduction along 3 different directions in 2D tissues. It may be noted that the wavelength of ECG signals of N-Glycanase treated tissues is shorter than fully glycosylated tissue. Because ECG signals are derived from a piece of ventricular tissue instead of a 3D heart, it is difficult to obtain T wave. However, 3-lead ECG signals indicate that reduced glycosylation influences the electrical propagation on the 2D tissue. Further, the waveforms of ECG signals demonstrate that reduced glycosylation will shorten the wavelength in ECG signals. The in-silico prediction results show that reduced glycosylation can potentially be used to shorten the QT interval, thereby controlling the LQTS.

Second, spiral waves were simulated in the fully glycosylated and N-Glycanase treated ventricular tissues to investigate how reduced glycoslyation will impact the progression of reentrant cardiac arrhythmias. Note that spiral wave simulations roughly correlate with monomorphic ventricular tachycardia. Two spiral waves were rotating for at least 8s to reach the steady state. As shown in Figure 2-15, there are distinct differences in the wave lengths between full glycosylation and N-Glycanase treated. The measurements show that N-Glycanase treated tissue yields a smaller width of wave (L2 = 5.64 cm) than the fully glycosylated one (L1 = 6 cm). This indicates that the vulnerability to arrhythmia is different for reduced hERG channel glycosylation, because the wave length impacts not only the propagation of electrical waves in space but also the rotating cycle of the vortex.

Furthermore, we derived the 3-lead ECG to characterize how N-Glycanase treatment of hERG channels impacts the propagation of spiral waves. Figure 2-13b depicts the locations of 3

electrodes for deriving the ECG. As shown in Figure 2-14b, the waveforms of ECG signals are distinctly different from the ones in rectilinear waves, because spiral waves represent and model cardiac arrhythmias. In addition, N-Glycanase treated tissue is predicted to yield a shorter RR interval than fully glycosylated tissue. In other words, N-Glycanase treated tissue takes less time to fulfill a single cardiac cycle than full glycosylation, when stimulated with the same protocol, assuming only hERG channel gating is impacted by N-Glycanase treatment. Figure 2-14b shows that N-Glycanase yields the ECG cycle of 0.207s, which is shorter than 0.22s in full glycosylation. Because of the prolonged T wave in LQTS, depolarization often occurs during the late repolarization phase of the previous ECG cycle (R on T phenomenon) [11]. Therefore, N-Glycanase can potentially prevent a premature depolarization by shortening the ECG cycle. This can potentially reduce the risk of LQTS and spiral wave breakups (i.e., Ventricular Tachycardia is less likely transfer into Ventricular Fibrillation) [30].
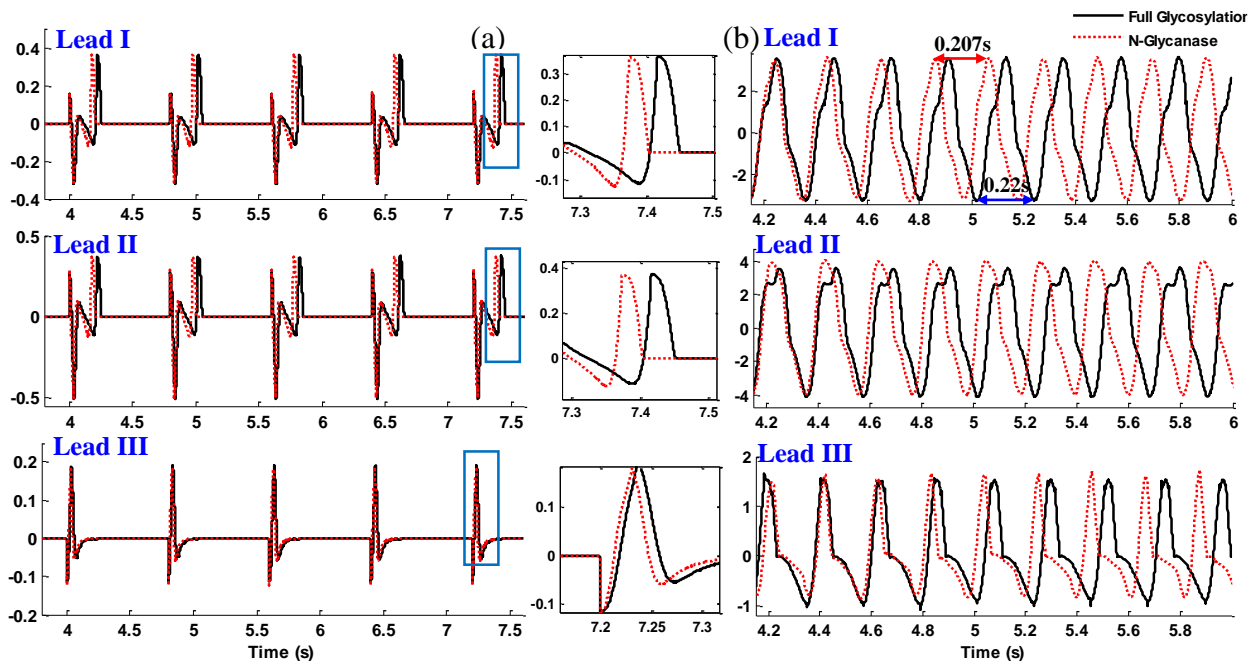
Figure 2-14 Derived Lead I, II, III ECG signals from the propagation of rectilinear waves and spiral waves in 2D cardiac tissues. (Solid black line: Fully Glycosylation. Red dash line: N-Glycanase treated.)
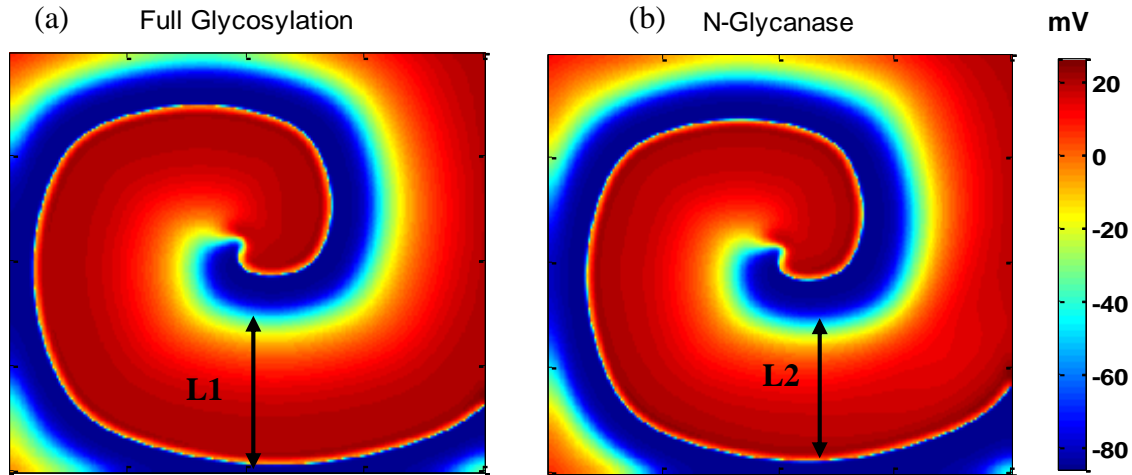
Figure 2-15 Spiral waves in fully glycosylated & N-Glycanase treated cardiac tissues.

2.4.8 State Occupancy of hERG Channels

Figure 2-16 shows how reduced glycosylation impacts the state occupancy in the Markov model of hERG channels. Note that fully glycosylated channel transfer out of C1 to O and I faster than reduce glycosylated channels. At the early stage of AP (phase 0-2), hERG channel mostly stays in I and C, and switches to O in the rapid repolarization phase (Figure 2-16 c-d). Figure 20 d shows the state occupancies at 287ms. Noted that fully glycosylated channels are out of C and stay in I, while reduce glycosylated channels has already began to enter the O state. At 300ms (Figure 2-16 e), fully glycosylated channels transfer from I to O, but reduce glycosylated channels enter more and more into the O state and begin to go back to C. The state occupancy diagram in different glycosylation conditions shows the glycosylation-modulated variations of I_{Kr} and AP.

2.5 Conclusions

In the pharmaceutical industry, in-vitro and in-vivo experiments are widely used to characterize and quantify the drug effects on biological systems. However, there are often many practical and ethical limitations in physical experiments of animal or human subjects. Also, it is very expensive

and difficult to comprehensively conduct physical experiments across biological scales, e.g., from ion channels to cells to tissues. In-silico models allow one to overcome these limitations, discover gaps in the in-vivo data, derive new hypotheses and/or suggest new experimental designs.
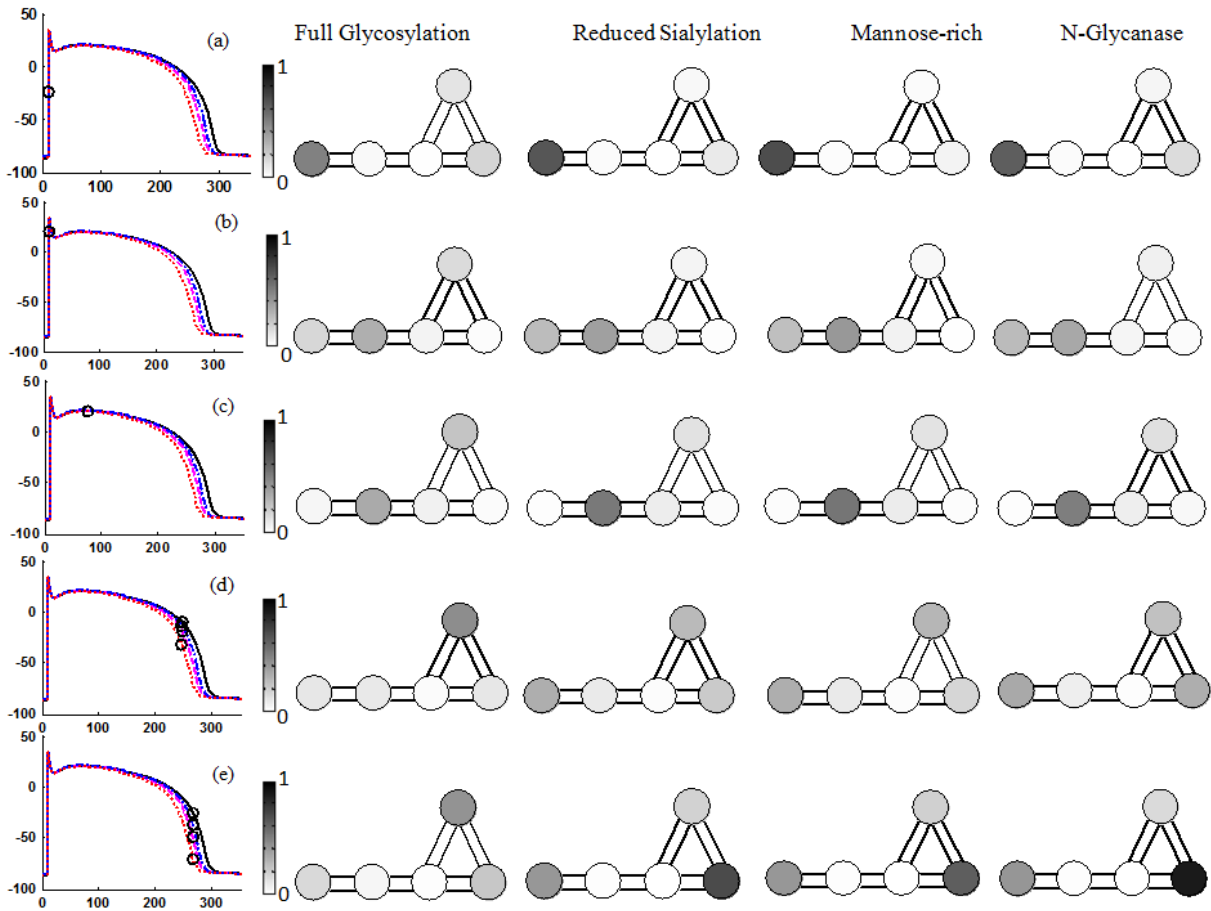
Figure 2-16 Markov state occupancy under the conditions of full glycosylation, reduced sialylation, mannose-rich and N-Glycanase.

Although computer models have long been intertwined with physical experiments in cardiac research, no approach to date has integrated the understanding of cardiac function in variable levels of glycosylation across the physical scales of increasing complexity, from molecules to cells to tissues. Note that cardiac ion channels are heavily glycosylated, and slight changes in the glycan structure can possibly impact the gating behaviors of ion channels. This study made one of the first

attempts to integrate glycosylation-channel data from in-vitro experiments with in-silico models to investigate how aberrant glycosylation modulates hERG ion channels and, as a result, cardiac electrical signaling across different organization levels, from molecule to cell to tissues.

Currently, little data is available about how reduced glycosylation will impact the gating of hERG channels [26]. In this present investigation, it is shown that reduced glycosylation, i.e., reduced sialylation, mannose-rich and N-Glycanase, shifts the steady-state activation and inactivation of hERG channels towards more positive potentials. These measured changes were integrated with in-silico models to predict glycosylation modulation dynamics on cardiac cells and tissues. The results of computer experiments show that reduced glycosylation increases the I_{Kr} magnitudes and shortens the APD. These glycosylation-induced changes are consistent over a range of pacing rates from 0.5 Hz to 2Hz, but they are less pronounced for faster rates. Also, the APD restitution indicates that reduced glycosylation does not increase the probability of spiral wave breakups. Further, the abruptions in inhomogeneous cable experiments show that reduced glycosylation affects the AP repolarization and shortens the wavelength in 1D cable. It may be noted that N-Glycanase has the most significant effect on cardiac repolarization and electrical propagations. Moreover, 3-lead ECGs derived from rectilinear waves and spiral waves in 2D tissues demonstrate that reduced hERG channel glycosylation narrows the width of waves, shortens the QT interval, and speeds up the reentry.

Because QT intervals are closely related to ventricular repolarization and hERG ion channel gating, a better understanding of glycosylation modulation dynamics in hERG ion channels can suggest a possible new mechanism to control QT intervals in ECG signals. As a result, new "rescue" therapies can be developed by imposing a glycan-dependent change in channel function that counterbalances the dysfunction due to diseases such as long QT syndrome. Our future studies

will be dedicated to a continued understanding of how regulated and aberrant glycosylation impacts cardiac function using in-vitro and in-vivo experiments as well as in-silico simulations as tools to test this novel mechanism for the control of cardiac electrical signaling.

2.6   References

[1]   A. R. Ednie and E. S. Bennett, "Modulation of voltage-gated ion channels by sialylation," in Comprehensive Physiology, John Wiley & Sons, Inc., pp. 1269-1301, 2012.

[2]   T. A. Schwetz, S. A. Norring, A. R. Ednie and E. S. Bennett, "Sialic acids attached to O-glycans modulate voltage-gated potassium channel gating." Journal of Biological Chemistry, vol. 286, pp. 4123-4132, 2011.

[3]   M. L. Montpetit, P. J. Stocker, T. A. Schwetz, J. M. Harper, S. A. Norring, L. Schaffer, S. J. North, J. Jang-Lee, T. Gilmartin, S. R. Head, S. M. Haslam, A. Dell, J. D. Marth and E. S. Bennett, "Regulated and aberrant glycosylation modulate cardiac electrical signaling," Proc Natl Acad Sci USA, vol. 106, pp. 16517-16522, 2009.

[4]   P. J. Stocker and E. S. Bennett, "Differential Sialylation Modulates Voltage-gated Na+ Channel Gating throughout the Developing Myocardium," The Journal of General Physiology, vol. 127, pp. 253-265, March 01, 2006.

[5]   I. Watanabe, J. Zhu, J. J. Sutachan, A. Gottschalk, E. Recio-Pinto and W. B. Thornhill, "The glycosylation state of Kv1.2 potassium channels affects trafficking, gating, and simulated action potentials," Brain Research, vol. 1144, pp. 18, 2007.

[6]   C. A. Ufret-Vincenty, D. J. Baro and L. F. Santana, "Differential contribution of sialic acid to the function of repolarizing K+ currents in ventricular myocytes," American Journal of Physiology - Cell Physiology, vol. 281, pp. C464-C474, August 01, 2001.

[7]   Y. Zhang, H. A. Hartmann and J. Satin, "Glycosylation influences voltage-dependent gating of cardiac and skeletal muscle sodium Channels." Journal of Membrane Biology, vol. 171, pp. 195-207, 1999.

[8]   H. H. Freeze, "Genetic defects in the human glycome," Nat. Rev. Genet., vol. 7, pp. 537-551, 2006.

[9]   J. Jaeken, "Congenital disorders of glycosylation (CDG): Update and new developments," J. Inherit. Metab. Dis., vol. 27, pp. 423-426, 2004.

[10]   M. C. Sanguinetti and M. Tristani-Firouzi, "hERG potassium channels and cardiac arrhythmia," Nature, vol. 400, pp. 463-469, 2006.

[11]   H. Morita, J. Wu and D. P. Zipes, "The QT syndromes: long and short," The Lancet, vol. 372, pp. 750-763, 2008.

[12] R. H. Clayton, O. Bernus, E. M. Cherry, H. Dierckx, F. H. Fenton, L. Mirabella, A. V. Panfilov, F. B. Sachse, G. Seemann and H. Zhang, "Models of cardiac tissue electrophysiology: Progress, challenges and open questions," Progress in Biophysics and Molecular Biology, vol. 104, pp. 22-48, 2011.

[13] M. Fink, S. A. Niederer, E. M. Cherry, F. H. Fenton, J. T. Koivumäki, G. Seemann, R. Thul, H. Zhang, F. B. Sachse, D. Beard, E. J. Crampin and N. P. Smith, "Cardiac cell modeling: Observations from the heart of the cardiac physiome project," Progress in Biophysics and Molecular Biology, vol. 104, pp. 2-21, 2011.

[14] S. Wang, S. Liu, M. J. Morales, H. C. Strauss and R. L. Rasmusson, "A quantitative analysis of the activation and inactivation kinetics of HERG expressed in Xenopus oocytes." The Journal of Physiology, vol. 502, pp. 45-60, July 01, 1997.

[15] C. E. Clancy and Y. Rudy, "Cellular consequences of HERG mutations in the long QT syndrome: precursors to sudden cardiac death," Cardiovascular Research, vol. 50, pp. 301-313, May 01, 2001.

[16] R. Mazhari, J. L. Greenstein, R. L. Winslow, E. Marbán and H. B. Nuss, "Molecular Interactions Between Two Long-QT Syndrome Gene Products, HERG and KCNE2, Rationalized by In Vitro and In Silico Analysis," Circulation Research, vol. 89, pp. 33-38, July 06, 2001.

[17] C. S. Oehmen, W. R. Giles and S. S. Demir, "Mathematical Model of the Rapidly Activating Delayed Rectifier Potassium Current IKr in Rabbit Sinoatrial Node," J. Cardiovasc. Electrophysiol., vol. 13, pp. 1131-1140, 2002.

[18] G. C. Bett, Q. Zhou and R. L. Rasmusson, "Models of HERG Gating," Biophys. J., vol. 101, pp. 631-642, 8/3, 2011.

[19] L. Priebe and D. J. Beuckelmann, "Simulation Study of Cellular Electric Properties in Heart Failure," Circulation Research, vol. 82, pp. 1206-1223, June 15, 1998.

[20] K. H. W. J. Ten Tusscher, D. Noble, P. J. Noble and A. V. Panfilov, "A model for human ventricular tissue," Am J Physiol Heart Circ Physiol, vol. 286, pp. 1573-1589, 2004.

[21] K. H. W. J. Ten Tusscher and A. V. Panfilov, "Alternans and spiral breakup in a human ventricular tissue model," Am J Physiol Heart Circ Physiol, vol. 291, pp. H1088-H1100, September 01, 2006.

[22] V. Iyer, R. Mazhari and R. L. Winslow, "A Computational Model of the Human Left-Ventricular Epicardial Myocyte," Biophys. J., vol. 87, pp. 1507-1525, 9, 2004.

[23] E. Grandi, F. S. Pasqualini and D. M. Bers, "A novel computational model of the human ventricular action potential and Ca transient," J. Mol. Cell. Cardiol., vol. 48, pp. 112-121, 1, 2010.

[24] T. O'Hara, L. Virág, A. Varró and Y. Rudy, "Simulation of the undiseased human cardiac cardiac ventricular action potential: model formulation and experimental validation," PLoS Computational Biology, vol. 7, pp. e1002061, 2011.

[25] J. Malmivuo and R. Plonsey, Bioelectromagnetism:Principles and Applications of Bioelectric and Biomagnetic Fields. New York Oxford: Oxford University Press, 1995.

[26] S. A. Norring, A. R. Ednie, T. A. Schwetz, D. Du, H. Yang and E. S. Bennett, "Channel Sialic Acids Limit hERG Channel Activity During the Ventricular Action Potential," The FASEB Journal, vol. 27, pp. 622-631, 2013.

[27] D. Du, H. Yang, S. A. Norring and E. S. Bennett, "Multi-scale modeling of glycosylation modulation dynamics in cardiac electrical signaling," in Engineering in Medicine and Biology Society,EMBC, 2011 Annual International Conference of the IEEE, 2011, pp. 104-107.

[28] R. H. Byrd, J. C. Gilbert and J. Nocedal, "A trust region method based on interior point techniques for nonlinear programming," Math. Program., vol. 89, pp. 149-185, 11/01, 2000.

[29] F. Xie, Z. Qu, A. Garfinkel and J. N. Weiss, "Electrical refractory period restitution and spiral wave reentry in simulated cardiac tissue," Am J Physiol Heart Circ Physiol, vol. 283, pp. 448-460, 2002.

[30] A. R. Ednie, K. K. Horton, J. Wu and E. S. Bennett, "Expression of the sialyltransferase, ST3Gal4, impacts cardiac voltage-gated sodium channel activity, refractory period and ventricular conduction," J Mol Cell Cardiol, vol. 59, pp. 117-127, 2013.

[31] J. N. Weiss, P. S. Chen, Z. Qu, H. S. Karagueuzian and A. Garfinkel, "Ventricular Fibrillation : How Do We Stop the Waves From Breaking?" Circulation Research, vol. 87, pp. 1103-1107, December 08, 2000.

[32] D. Du, H. Yang, S. Norring and E. Bennett, "In-Silico Modeling of Glycosylation Modulation Dynamics in hERG Ion Channels and Cardiac Electrical Signals," IEEE Journal of Biomedical and Health Informatics, vol. 18, pp. 205-214, 2014.

Chapter 3 Statistical Metamodeling and Sequential Design of Computer Experiments to

Model Glyco-altered Gating of Sodium Channels in Cardiac Myocytes

Glycan structures account for up to 35% of the mass of cardiac sodium (Na_v) channels. To question whether and how reduced sialylation affects Na_v activity and cardiac electrical signaling, we conducted a series of in-vitro experiments. Although aberrant electrical signaling is observed in reduced sialylation, realizing a better understanding of mechanistic details of pathological variations in I_{Na} and AP is difficult without performing in-silico studies. However, computer model of Na_v channels and cardiac myocytes involves greater levels of complexity, e.g., high-dimensional parameter space, nonlinear and non-convex equations. Traditional linear and nonlinear optimization methods have encountered many difficulties for model calibration. This study presents a new statistical metamodeling approach for efficient computer experiments and optimization of Na_v models. First, we utilize a fractional factorial design to identify control variables from the large set of model parameters, thereby reducing the dimensionality of parametric space. Further, we develop the Gaussian Process (GP) model as a surrogate of expensive and time-consuming computer models and then identify the next best design point that yields the maximal probability of improvement. This process iterates until convergence, and the performance is evaluated and validated with real-world experimental data. Experimental results show the proposed algorithm achieves superior performance in modeling glycosylated and controlled kinetics of Na_v channels. As a result, in-silico models provide a better understanding of glycol-altered mechanistic details in state transitions and distributions of Na_v channels. Notably,

ST3Gal4-/- myocytes are shown to have higher probabilities accumulated in intermediate inactivation during the repolarization and yield a shorter refractory period than WTs. The proposed approach of statistical design of computer experiments is generally extensible to many other disciplines that involve large-scale and computationally expensive models.

3.1   Introduction

Action potential (AP), the net change of transmembrane potential in a cardiac myocyte during a contraction cycle, is produced by the orchestrated function of ion channels. A slight change in ion channel activity may affect the AP waveform and electrical conduction, thereby potentially leading to severe cardiac disorders. Voltage-gated sodium (Na_v) channel activity is responsible for the excitation of cells and contributes to electrical conduction in tissues [1, 2]. It was shown that Na_v channels can be extensively post-translationally modified by protein glycosylation through isoform-specific mechanisms [3-8]. Typically, glycosylation-dependent gating effects were imposed on ion channels primarily by the terminal residue attached to N- and O-glycans, sialic acid [3-8]. Montpetit *et al.* showed that cardiac glycome (i.e., the complete set of glycan structures produced in the heart) varies between atria and ventricles, and changes differentially during development of each cardiac chamber. In addition, regulated expression of a single glycogene was shown to modulate AP waveforms and gating of less sialylated Na_v consistently [9].

Growing evidence suggests that reduced glycosylation has dramatic effects on ion channels and cardiac electrical signaling. There is a set of >40 distinct forms of inherited human diseases of reduced glycosylation known as Congenital Disorders of Glycosylation (CDG) caused, typically, by a mutation or deficiency in a glycogene that results in a relatively modest reduction in glycoprotein glycosylation [1-14]. While the mechanism(s) is not yet understood, recently reported prevalence of cardiac involvement prompted experts to suggest screening for cardiac dysfunction

50

in all CDG patients and for CDG in all young patients suffering from cardiomyopathy of unknown etiology [15].

In order to question whether and how reduced glycosylation affects Na_v activity and cardiac electrical signaling, we conducted a series of electrophysiological experiments to measure and characterize sodium currents (I_{Na}) and action potentials (AP). The experiments showed that ventricular Na_v from the sialyltransferase beta-galactoside alpha-2,3-sialyltransferase 4 (ST3Gal4) deficient mice (ST3Gal4$^{-/-}$) inactivated more slowly and recovered from fast inactivation more rapidly than wild type (WT) controls, and ST3Gal4$^{-/-}$ cell showed a shortened myocytes refractory period. Although we observed aberrant electrical signaling in ST3Gal4$^{-/-}$ ventricular myocytes and across the ST3Gal4$^{-/-}$ ventricle, understanding mechanistic details of pathological variations in I_{Na} and AP is very difficult without performing in-silico studies. Experiments can measure ionic currents I_{Na} and AP with voltage and current clamp protocols, but preclude us from determining directly the change in transitions among molecular states (e.g., open, close, intermediate inactivated, and fast inactivated states) and their systematic contributions to AP variations. There is an urgent need to integrate computer models with experimental data to model the variations of state transitions under conditions of reduced sialylation, and the resulting changes in ionic currents and AP.

In this present study, we propose to couple in-silico studies with the wealth of data from our electrophysiological experiments to model, mechanistically, how reduced sialylation that occurs in the ST3Gal4$^{-/-}$ heart affects Na_v channel activity and electrical signaling in the adult mouse ventricle. Indeed, computer models not only overcome practical and ethical limitations in physical experiments but also provide predictive insights into the underlying mechanisms.

Computer models of Na_v channels involve greater levels of complexity, e.g., the high dimensionality of parameter space, nonlinear and non-convex characteristics. Hodgkin and Huxley

formulated the first model of myocyte AP in 1952 using a set of nonlinear and ordinary differential equations, including the submodels of potassium, sodium and leak channels. However, Hodgkin-Huxley model is not adequate to capture detailed gating mechanisms of Na_v channels. Further, Clancy and Rudy developed a 9-state Markov model for I_{Na} with three closed states (C1, C2, C3), one fast inactivation (IF), one open state (O), two intermediate inactivated states (I1, I2) and two closed-inactivation states (IC2, IC3) [18]. The dynamic transitions among Markov states involve a large set of interacting nonlinear differential equations, and thus lead to highly nonlinear and non-convex characteristics in the model.

In order to model glyco-altered I_{Na}, there are a total of 25 calibration parameters that need to be estimated (also see Table 3-1). This gives rise to the issue of "curse of dimensionality" for model calibration because we would need 2^{25} (approximately 33.5 million) design points to run full-factorial experiments that fill up the corner points of a 25-dimensional hypercube. In addition, we will need to follow standard pulse protocols used in electrophysiological experiments (i.e., steady state activation, steady state inactivation and recovery from fast inactivation) to design computer experiments for the minimization of model discrepancy from real-world experimental data. In other words, this is a multi-objective optimization problem instead of a single objective function. As such, the process of model calibration is very computationally expensive, due to the running of complex Markov model in the high-dimensional design space. It should be noted that traditional linear and nonlinear optimization methods (e.g., interior point algorithm, trust-region reflective algorithm, Levenberg-Marquardt algorithm and genetic algorithm) have encountered many difficulties, even infeasible, for I_{Na} model calibration and computer experiments.

This study presents a new statistical metamodeling approach for efficient computer experiments and optimization of Na_v channel models, so as to describe glyco-altered Na_v gating kinetics using

52

a model for reduced Na_v channel sialylation as an experimental model system in the ST3Gal4$^{-/-}$ heart. The organization of this study is as follows: Section 3.2 presents the research methodology, including screening design, space-filling design, statistical metamodel and the maximal probability of improvement; section 3.3 introduces the materials and experimental protocols; Section 3.4 presents experimental results; Section 3.5 includes the conclusions arising out of this investigation.

3.2　Research Methodology

It is well known that cardiac models involve a large set of nonlinear differential equations with a high-dimensional space of model parameters. As a result, nonlinear and non-convex characteristics pose significant challenges for traditional optimization methods to achieve optimal solutions. In addition, solving nonlinear differential equations are often heavily computationally-expensive when a large number of experimental runs are needed. It is impractical to seek an optimal solution through the exhaustive search (or full-factorial experiments) in the high-dimensional design space. Hence, there is an urgent need to minimize the number of runs (i.e., reduce the computational cost and time) while calibrating computer models. However, few, if any, previous studies have focused on the statistical design of experiments for model calibration in the field of cardiac simulation and modeling. The present investigation is the first of its kind to integrate statistical metamodeling with sequential design of experiments for efficient and effective calibration of cardiac models.

As shown in Figure 3-1, this present investigation is embodied by three core components focusing on the development of statistical metamodels for efficient and effective calibration of cardiac models. (1) The first component is aimed at the screening of model parameters so as to identify control variables that are sensitive to response functions. Notably, this present investigation includes three different response functions in the computer model of Nav channels

(i.e., steady state activation, steady state inactivation and recovery from fast inactivation). As such, we designed the fractional factorial experiments to identify control variables that are sensitive to one response function but not others. This first component will screen important variables and reduce the dimension of design space, thereby improving the effectiveness and efficiency of statistical metamodeling. (2) The second component will develop statistical metamodels to predict the response functions in the control variable space based on a small sample of computed responses from computer models. The statistical metamodels will serve as the surrogates of expensive and time-consuming computer models. (3) The third component aims to develop an expected improvement algorithm, extended from Jones et al [19], to calculate the responses of statistical metamodels based on a space-filling design and then select the next best point according to the criterion of maximal probability of improvement for running an additional experiment on computer models. Further, this process will continue selecting the next best point and updating the statistical metamodel until the convergence criterion is satisfied. All three components are eventually integrated together in the framework of sequential design of computer experiments to make the calibration of computer models of complex cardiac systems more effective and efficient. The details of this new method are described below.

3.2.1 Screening Design

In order to avoid the "curse-of-dimensionality", it is critical to study the effects of model parameters for identifying control variables that are sensitive to model discrepancy instead of other noise. In this investigation, the computer model includes output variables $\tilde{y}$ and the P-dimensional parameters $\boldsymbol{x}$ (i.e., the large set of covariates with potential effects on outputs) as follows:

$$\text{Computer model: } \tilde{y} = f(t, \boldsymbol{x}, V)$$

$$\text{Model parameters: } \boldsymbol{x}|P = (x_1, x_2, \dots, x_P)$$

Control variables: $x|p = (x_1, x_2, ..., x_p)$

Real experimental data: y

Model discrepancy: $\delta = |y - \tilde{y}|$

The screening design is aimed at identifying a low-dimensional set of *important control variables* $(x|p, p << P)$ from the high-dimensional set of *potential model parameters* $(x|P)$ so as to facilitate the process of statistical metamodeling. It is not uncommon that the "one-factor-at-a-time (OFAT)" approach is used to investigate each parameter by itself, ignoring the other parameters. The recommendation is made only based on how the change of a single parameter Δx impacts the model discrepancy δ. Although this is computationally efficient, this OFAT approach cannot estimate the joint effects of parameters and can also miss important factors [20].
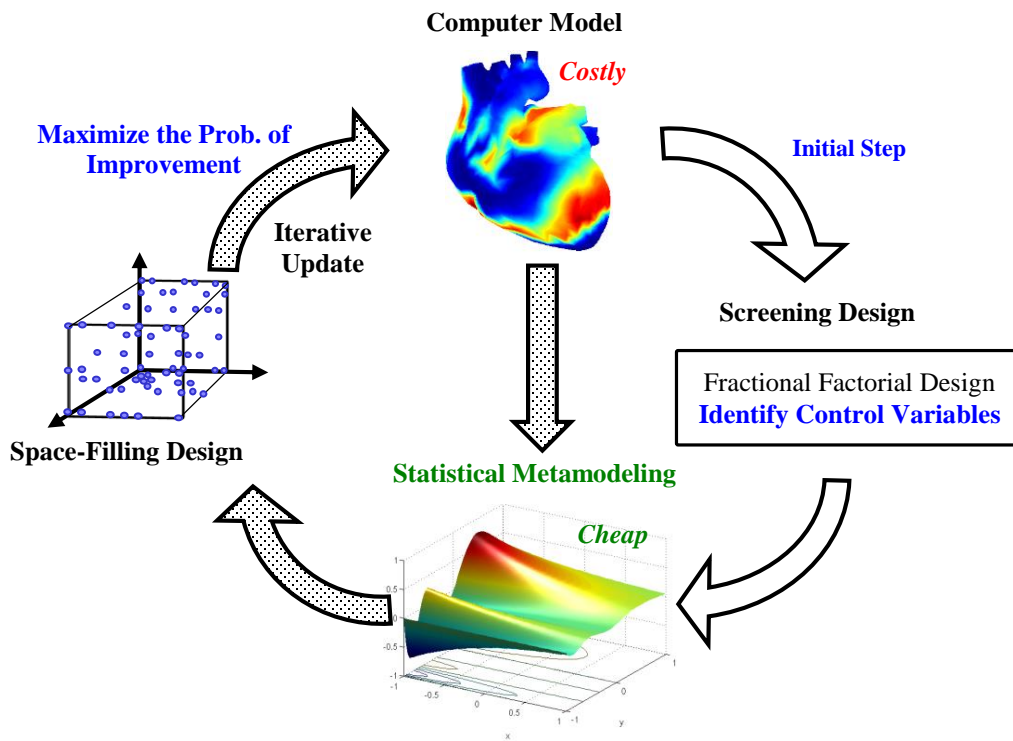
Figure 3-1 Flow chart of the proposed research methodology.

Hence, we adopted the fractional factorial design for the sensitivity analysis of parametric effects on response functions. In this study, there is a set of 25 parameters that have potential effects on the model discrepancy δ of Na^+ ion channels. If each parameter varies at two levels (+1 and -1), a full factorial design will require $2^{25} = 33554432$ runs, which is computationally expensive and time consuming. Because some higher-order interactions are likely to be negligible based on the effect hierarchy principle, we used a 1024-run 2_V^{25-15} fractional factorial design. It should be noted that the resolution V ensures that the main effects are strongly clear and the two-factor interactions are clear. If we denote the 25 parameters by letters 'a'-'y', the design generators derived from the Franklin-Bailey algorithm [21] are:

$$k = abcdefghij;\ l = defghij;\ m = bcfghij;$$

$$n = aceghij;\ o = bdghij;\ p = cefhij;\ q = adfhij;$$

$$r = abehij;\ s = abcdhij;\ t = abefgij;\ u = acfgij;$$

$$v = cdegij;\ w = bcdefij;\ x = befghj;\ y = afghj$$

After obtaining computed responses from the 1024-run experiments on computer models, factorial effects of parameters are estimated by the linear model as:

$$\delta = \beta_0 + \sum_{i=1}^{P} \beta_i x_i + \varepsilon$$

where $i = 1, \dots, P$ is the number of considered parameters. Notably, the least squares estimate $\hat{\beta}_i$ is half of the factorial effect x_i, i.e.

$$\hat{\beta}_i = \frac{1}{1-(-1)}\left(\bar{y}(x_i = 1) - \bar{y}(x_i = -1)\right)$$

$$= \frac{1}{2}\left(\bar{y}(x_i = 1) - \bar{y}(x_i = -1)\right)$$

As such, factorial effects are obtained by doubling the regression coefficients $\hat{\beta}_i's$. Further, we

used a graphical method, namely half-normal probability plot, to test the significance of factorial effects. The fundamental idea is to use the normal curve as the reference distribution against which the significance of effects is tested [22]. Under the null hypothesis of no significant effect, factorial effects are approximately normally-distributed random noises, i.e., $\hat{\beta}_i \sim N(0, \sigma^2)$. As a result, any effect whose point falls off the straight line in the half-normal probability plot is declared significant. The half-normal probability plot is composed of points, i.e.,

$$\left[\Phi^{-1}\left(0.5 + \frac{0.5[i - 0.5]}{P} \right), |\hat{\beta}_{(i)}| \right], i = 1, 2, \cdots P$$

where Φ is the cumulative distribution function (CDF) of a standard normal random variable. The absolute values of factorial effects are ordered as $|\hat{\beta}_{(1)}| \leq \cdots \leq |\hat{\beta}_{(P)}|$, and then plotted against the coordinates based on the half-normal distribution. In the half-normal probability plot, all the significant effects will fall above the straight line of small factorial effects and appear in the upper right corner of the plot. To this end, the initial step of variable screening identifies a reduced set of control variables $(x|p, p << P)$ that will be used to construct statistical metamodels in the following section 3.2.2 and 3.2.3.

3.2.2 Space-Filling Design

The next step is to select inputs $X = (x_1, \ldots, x_n)$, $n \times p$ dimension, at which to calculate the responses of computer models. Space-filling design is commonly used in computer experiments when prediction accuracy is a primary interest. In this present investigation, we proposed the maximin distance design of Latin Hypercube (LH) Sampling to evenly spread the values of the inputs in the experimental region.

In order to obtain a $n \times p$ LH sample $X = (x_1, x_2, \ldots, x_n)$ in the p dimensional experimental regions $[0,1]^p$, each dimension $[0,1]$ is first divided into n equally spaced intervals $[0,1/$

n), ..., $[(n-1)/n, 1]$. All p-dimensional Cartesian products of these intervals provide the n^p cells of equal size. Then, an $n \times p$ matrix $\mathbf{\Pi} = (\Pi_{ij})$ is generated so that its columns are random permutations of $\{1, 2, ..., n\}$. The LH sample $x_{ij}, i = 1, ..., n; j = 1, ..., p$ is obtained from the matrix $\mathbf{\Pi}$ as follows:

$$x_{ij} = \frac{\Pi_{ij} - 0.5}{n}, i = 1, ..., n; j = 1, ..., p$$

The LH sampling evenly distributes the design points when projecting onto the domain of each input variable in the experimental region. Further, we used the *maximin distance* criterion to measure the spread of design points in the experimental region. In other words, any pair of design points should not be "too" close together. In this present investigation, the distance measure between two design points $\mathbf{x}_i$ and $\mathbf{x}_j$ is defined as

$$d_{ij} = \|\mathbf{x}_i - \mathbf{x}_j\|$$

where $\|\cdot\|$ denotes the Euclidean norm. The maximin distance design aims to maximize the minimal distance between any two points in the design space, and thereby guarantee that design points are spread over the experimental region [23]:

$$\max_{\mathbf{X} \in [0,1]^d} \min_{i \neq j} d_{ij}$$

Figure 3-2 shows an illustration of maximin distance design in the 2-dimensional design space $[0,1]^2$. Notably, the design in Figure 3-2 (a) has a smaller minimal distance between two design points than Figure 3-2 (b). As such, design points in Figure 3-2 (b) are distributed more evenly. In this present study, the domain of each control variable has a different range, and therefore design points in the p dimensional experimental regions $[0,1]^p$ are rescaled to their corresponding domains. In addition, the LH sampling is repeated several times and then we select the one maximizing the minimal distance between points.
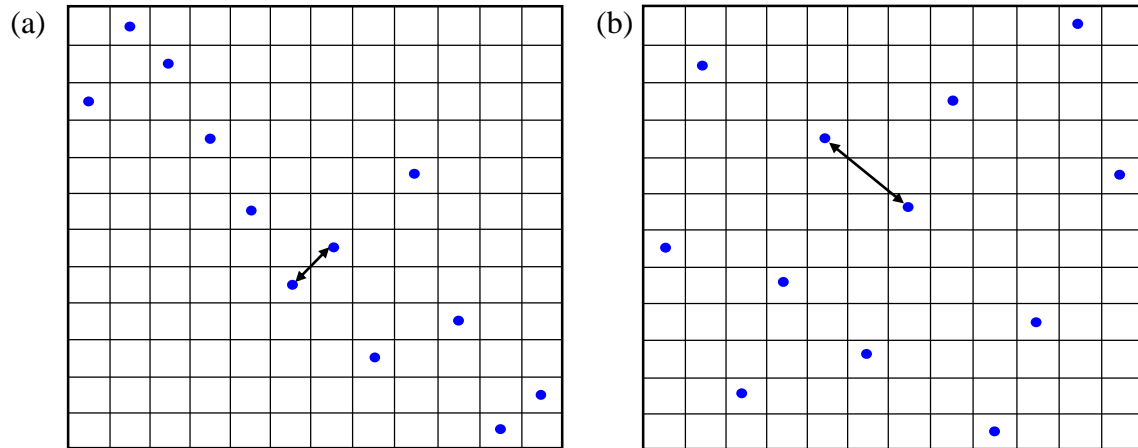
Figure 3-2 Maxmin Latin hypercube design.

3.2.3 Statistical Metamodeling

In this section, we will approximate the discrepancy between computer model and electrophysiological data using the easy-to-evaluate statistical metamodels. This is done in two steps. First, we will run the computer model to compute the responses at some settings of control variables using the maximin Latin Hypercube Design (LHD). Then, we will fit statistical models to capture the relationships between control variables and model discrepancy, which can be used as an approximation model to minimize the discrepancy between computer model and electrophysiological data. Notably, the prediction accuracy depends on the general tendency as well as the uncertainty of statistical metamodels in modeling the response surface. Although the metamodeling approach has been widely used in engineering [23, 24], we have not seen its applications in the cardiovascular domain. In addition, functional responses, pulse protocols and cardiac constraints call for the new development of statistical metamodeling methods that are well-suited for cardiovascular studies.

In this present study, we adopted the Gaussian Process (GP) modeling approach to develop the statistical metamodels. It is worth mentioning that GP model provides both mean and variance for the estimations of complex response surfaces, which facilitates the subsequent prediction and

59

uncertainty analysis of complex systems. Most of previous studies focused on the use of GP model for calibrating computer models in the engineering domain, e.g., Kennedy and O'Hagan [25], Qian and Wu [26], and Chang and Joseph [27]. However, calibrating cardiac models is not a straightforward application of aforementioned works, due to nonlinear/non-convex characteristics of models and different types of function responses (e.g., ion-channel currents and action potentials). Cardiac models need to be calibrated with specific considerations of the kinetics and physical properties of ion channels, cells, tissues, and the heart. This present investigation made an attempt to bridge the gaps in statistical metamodeling between engineering and cardiac domains.

As aforementioned in Section 3.2.2, let $\tilde{y}$ be the model output and $f(t, \boldsymbol{x}, V)$ be the computer model, where $\boldsymbol{x} = (x_1, x_2, \dots, x_p)$ is a p-dimensional vector of control variables (or calibration parameters). Let $(\boldsymbol{x_1}, y_1), \dots, (\boldsymbol{x_n}, y_n)$ be the real data obtained from electrophysiological experiments. The output of such data usually contains some errors due to the variations in the unobserved variables and measurement error. Therefore, we can write down the statistical model as:

$$z_i = |y_i - f(t, \boldsymbol{x_i}, V)| = \delta(\boldsymbol{x_i}) + \epsilon_i, \text{ for } i = 1, \dots, n$$

where $\epsilon_i \sim^{iid} N(0, \sigma_n^2)$, and the bias term $\delta(x)$ is modeled as a Gaussian process [28-31] specified by the mean function $m(\boldsymbol{x})$ and covariance function $k(\boldsymbol{x}, \boldsymbol{x'})$, i.e.,

$$\delta(\boldsymbol{x}) \sim GP(m(\boldsymbol{x}), k(\boldsymbol{x}, \boldsymbol{x'}))$$

$$m(\boldsymbol{x}) = \mathbb{E}[\delta(\boldsymbol{x})]$$

$$k(\boldsymbol{x}, \boldsymbol{x'}) = \mathbb{E}\big[\big(\delta(\boldsymbol{x}) - m(\boldsymbol{x})\big)\big(\delta(\boldsymbol{x'}) - m(\boldsymbol{x'})\big)\big]$$

The GP is defined as a collection of random variables, any finite set of which follows a joint Gaussian distribution. The GP is treated as a functional prior on the bias function [28-30]. Here, the covariance function specifies the covariance between pairs of random variables:

$$k(x, x') = \sigma_f^2 \exp\left(-\frac{1}{2}(x - x')^T M(x - x')\right)$$

where σ_f^2 is the signal variance and $M = \text{diag}(l)^{-2}$ with the length-scale vector l. Note that the $\delta(x)$ and $\delta(x')$ should be similar if x and x' are sufficiently close in the design space, therefore, the length scale l defines the separation between different dimensions of input variables. For a new design point x_*, the computed bias Z from $X = (x_1, \dots, x_n)$, and the predicted $\delta(x_*)$ have a joint prior distribution with zero mean:

$$\begin{bmatrix} Z \\ \delta_* \end{bmatrix} \sim N\left(0, \begin{bmatrix} K(X, X) + \sigma_n^2 I & K(X, x_*) \\ K(x_*, X) & K(x_*, x_*) \end{bmatrix}\right)$$

In order to obtain the posterior distribution, this joint prior distribution is restricted to include only those functions that agree with the computed observations from the space-filling design. Hence, the posterior distribution of δ_* is:

$$p(\delta_* | X, Z, x_*) \sim \mathcal{N}(\bar{\delta}_*, \text{cov}(\delta_*))$$

$$\bar{\delta}_* = \mathbb{E}(\delta_* | X, Z, x_*) = K(x_*, X)[K(X, X) + \sigma_n^2 I]^{-1} Z$$

$$\text{cov}(\delta_*) = K(x_*, x_*) - K(x_*, X)[K(X, X) + \sigma_n^2 I]^{-1} K(X, x_*)$$

However, the hyper-parameters $\theta = \{M, \sigma_f, \sigma_n\}$ need to be optimally chosen in order to yield the best GP model for predicting the point with the maximal probability of improvement to reduce the model discrepancy. These hyper-parameters can be learned by maximizing the log marginal likelihood, i.e.,

$$\theta_{\text{optimal}} = \text{argmax}_\theta \{\log p(Z | X, \theta)\}$$

$$\log p(Z | X, \theta) = -\frac{1}{2}\log|K + \sigma_n^2 I| - \frac{1}{2}Z^T[K + \sigma_n^2 I]^{-1}Z - \frac{n}{2}\log 2\pi$$

As such, the GP is optimally trained with the real experimental data and computed responses from the computer model based on the space-filling design. Figure 3-3 shows an example of GP

model for one-dimensional curve fitting, where blue dots are observed data, and black line shows the predictions from the GP model. The dash line indicates the prediction variances.
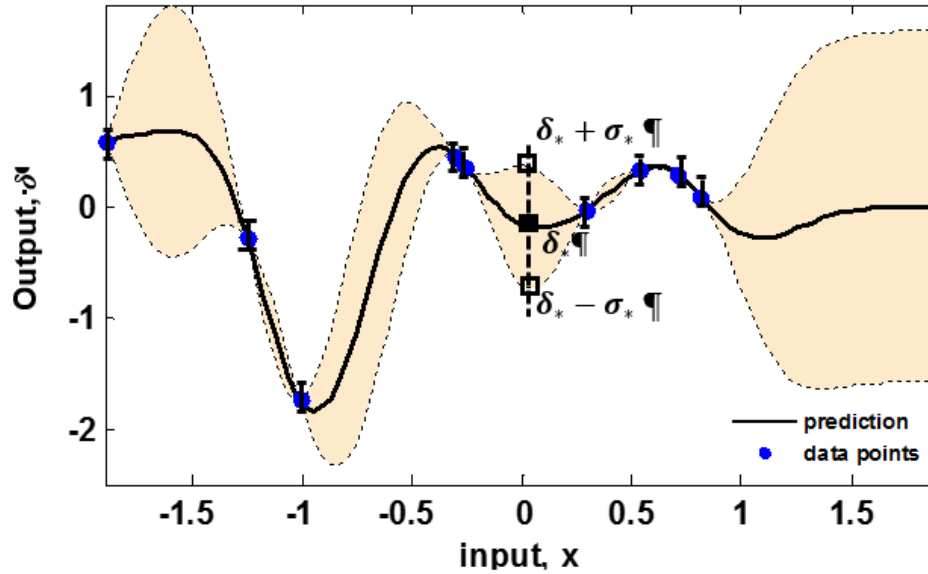
Figure 3-3 An illustration of Gaussian Process fitting of one-dimensional data.

3.2.4 Maximizing the Probability of Improvement

The statistical metamodel provides an approximate model of the functional relationship between model discrepancy $z = |y - f(t, x, V)|$ and control variables x. At any specific point x_* in the experimental region, the GP model predicts our uncertainty about the model discrepancy as the realization of a random variable δ_* with mean $\bar{\delta}_*(x_*)$ and standard error $s(\delta_*|x_*)$ (see Figure 3-4). However, this approximation is based on the initial set of design points $X = (x_1, \dots, x_n)$ from the space-filling design. Hence, we introduced an auxiliary function of the probability of improvement, extended from Jones et al [19], to identify an additional design point where the probability to minimize model discrepancy beyond the target T is the highest (see Figure 3-4):

$$\text{ProbI} = \Phi\left(\frac{T - \bar{\delta}_*(x_*)}{s(\delta_*|x_*)}\right)$$

where $\Phi(\cdot)$ is the Normal CDF function. The target value is defined as $T = \delta_{min} - 0.25|\delta_{min}|$ so as to yield an improvement of at least 25%. Therefore, the objective to minimize the model discrepancy is analogous to iteratively search the next best point $\boldsymbol{x}_*$ that maximizes the probability of improvement. In each iteration, we will compute the response and discrepancy of computer model at this additional best design point $\boldsymbol{x}_*$, and then update the statistical metamodel to search for the next best one.
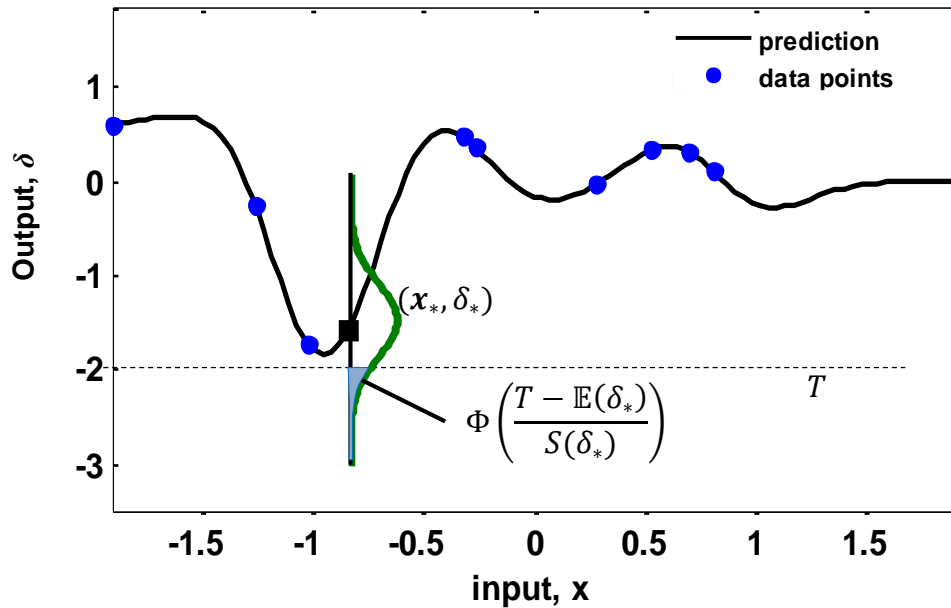
Figure 3-4 An illustration to estimate the probability at a given point to minimize model discrepancy beyond the target T.

It is worth mentioning that if we sample densely around the current best point, the uncertainty (i.e., standard error $s(\delta_*)$) in this region becomes small. As such, the quantity $(T - \bar{\delta}_*)/s(\delta_*)$ is highly negative because T is often less than $\bar{\delta}_*$. This leads to small probability of improvement around the current best point, thereby driving the algorithm to move to some points where the uncertainty is higher. Therefore, the point that has maximal probability could improve the metamodel most. This process will iterate until the convergence criterion is satisfied.

$$\text{argmin}_x |y - f(t, x, V)|$$

Initialization:

  Screen parameters to identify control variables $x = (x_1, \dots, x_p)^T$

  Sample n design points $X = (x_1; \dots; x_n)$ using the maximin LHD

  Evaluate the model output $\tilde{y}_i$ at each design point X_i, $i=1,\dots,n$

  Calculate the model discrepancy from experimental data y,

$$z_i = |y_i - f(t, x_i, V)|, \text{ for } i = 1, \dots, n$$

  Construct a GP model to estimate the response surface

While discrepancy>MinTol

  Sample m new design points $X_* = (x_{*1}, \dots, x_{*m})$ with the maximin LHD

  Predict the model discrepancy $\delta(X_*)$ of X_* using the GP model

  Calculate the probability of improvement (ProbI) for X_*

  Evaluate the model output at the next design with the maximal ProbI,

$$x_N = X_*(\max(\text{ProbI})), \ z_N = \delta_*(\max(\text{ProbI}))$$

  Update the dataset: $(X, Z) = \left(\begin{bmatrix} X \\ x_N \end{bmatrix}, \begin{bmatrix} Z \\ z_N \end{bmatrix} \right)$

  Update the GP model

End

Figure 3-5 The algorithm for statistical metamodeling and sequential design of computer experiments.

3.2.5 Algorithmic Summary for Statistical Metamodeling and Sequential Design of Computer Experiments

As shown in Figure 3-1 and Figure 3-5, the algorithm starts with parameters screening for identifying control variables $x = (x_1, \dots, x_p)^T$ that are sensitive to the variations of model discrepancy. Then, a set of design points $X = (x_1; \dots; x_n)$ is sampled in the p-dimensional space of control variables using the maximin Latin Hypercube Design. Based on the outputs $\tilde{y}$ at each design point x_i, $i=1,\dots,n$ calculated from computer model, the discrepancy from real experimental data is computed as:

$$z = |y - \tilde{y}| = |y - f(t, x, V)|$$

Once this dataset is obtained, a GP-based metamodel is built to model the functional relationship

between model discrepancy and control variables as:

$$z = \delta(x) + \epsilon$$

$$\delta(x) \sim GP(m(x), k(x, x'))$$

However, the GP model may not be accurate enough to capture the true response surface due to the scarcity of design points. Therefore, the GP model is iteratively updated by adding a new design point where the probability to minimize model discrepancy is the highest. This process iterates until the model discrepancy is lower than a minimal tolerance value (MinTol).

3.3 Cardiac Models and Experimental Protocols

We recently modeled the transition of molecular states in glyco-altered gating of hERG (I_{Kr}) channels, showing that N-glycosylation effectively limits hERG channel activity. From the in-silico models, reduced glycosylation was shown to shorten the repolarization phase of cardiac APs and impact the electrical conduction in cardiac fibers and tissues [16, 17]. In this present study, we previously conducted electrophysiological experiments to measure Na$_v$ channel activity and APs of mouse ventricular myocytes using voltage- and current-clamp methods [15]. These experiments provide two full sets of data; one under "control" (physiological, wild-type - WT) conditions, and the other under conditions of reduced sialylation (pathology, ST3Gal4$^{-/-}$). In this section, we will detail computer models and briefly describe experimental pulse protocols (for details, see Ednie et al, 15) together which are used to describe mechanistic details of pathological variations in the Nav channels and myocyte AP.

3.3.1 Computer Model of Ventricular Myocytes

This present investigation used the computer model of action potential of mouse ventricular myocytes from Bondarenko and Rasmusson et al [31], which is only for the mouse ventricular myocytes under "control" (physiological, wild-type - WT) conditions, but is not adequate to model

the mechanistic details of pathological variations (e.g., ST3Gal4$^{-/-}$) in the Na$^+$ ion channels and myocyte AP. The cellular AP is described by the ordinal differential equation:

$$-C_m \frac{dV}{dt} = I_{CaL} + I_{p(Ca)} + I_{NaCa} + I_{Cab} + I_{Na} + I_{Nab} + I_{NaK} +$$

$$I_{Kto,f} + I_{Kto,s} + I_{K1} + I_{Ks} + I_{Kur} + I_{Kss} + I_{Kr} + I_{Cl,Ca} + I_{stim}$$

where t is time, C_m is the cell capacitance, I_{stim} is the external stimulus current which activates the cell from the resting state. The transmembrane currents include the fast Na$^+$ current (I_{Na}), the L-type Ca^{2+} current (I_{CaL}), the rapidly recovering transient outward K$^+$ current ($I_{Kto,f}$), the slowly recovering transient outward K$^+$ current ($I_{Kto,s}$), the rapid delayed rectifier K$^+$ current (I_{Kr}), the ultrarapidly activating delayed rectifier K$^+$ current (I_{Kur}), the noninactivating steady-state voltage-activated K$^+$ current (I_{Kss}), the time-independent inwardly rectifying K$^+$ current (I_{K1}), the slow delayed rectifier K$^+$ current (I_{Ks}), the Na$^+$/Ca^{++}exchange current (I_{NaCa}), the Na$^+$/K$^+$ pump current (I_{NaK}), the Ca^{2+}pump current ($I_{p(Ca)}$), the Ca^{2+}-activated Cl$^-$ current, ant the background Ca^{2+} and Na$^+$ currents. Most ionic currents are modeled using Hodgkin-Huxley or Markov-based formulations, including the cell conductance, the gradients of membrane potential and gating dynamics. For details on all the ion-channel kinetics, see [31].

Our objective is to calibrate the model to describe mechanistic details of pathological variations (i.e., reduced sialylation) in the Na$^+$ ion channels and myocyte AP. Notably, this is not a trivial task, due to the nonlinear and non-convex characteristics in the complex kinetics of Na$^+$ ion channels, which will be detailed in the next section.

3.3.2 Computer Model of Nav Channels

As shown in Figure 3-6, the Markov model of Nav channels includes three close states (C$_1$, C$_2$, C$_3$), one fast inactivation (IF), one open state (O), two intermediate inactivated states (I1, I2) and

66

two closed-inactivation states (IC$_2$, IC$_3$). The transition rates are dependent on the membrane potential in a non-linear fashion. The state probability denotes the fraction of Na$^+$ channels in that state. Let **P** be the vector of state probability:

$$\mathbf{P} = [P_{IC3}, P_{IC2}, P_{IF}, P_{I1}, P_{I2}, P_{C3}, P_{C2}, P_{C1}, P_O]^{\mathrm{T}}$$

The temporal dynamics of **P** are modeled with the following differential equations:

$$\frac{d\mathbf{P}(t)}{dt} = \mathbf{A}(V) \times \mathbf{P}(t)$$

where **A** is the 9×9 transition rate matrix (see the supplement). The diagonal elements in **A** are the sum of transition rates that transfer out of the current state, e.g. $A_{1,1} = -(\alpha_{31} + \alpha_{111})$. The off-diagonal elements contain the transition rates that transfer into the current state from other states, e.g., $A_{1,2} = \beta_{111}$ and $A_{1,6} = \beta_{31}$. Note that $A_{1,2}$ determines the transition rate from IC$_2$ to IC$_3$ (see Figure 3-6). All non-zero elements in the transition rate matrix **A** are dependent on the membrane potential (V), thereby making the gating of Na^+ ion channels voltage-dependent. The fast Na^+ current, I_{Na}, is modeled as:

$$I_{Na} = G_{Na} P_O(t)(V - E_{Na})$$

where $P_O(t)$ is the probability of the Na^+ channels in the open state at time t, E_{Na} is the reverse potential and G_{Na} is the maximum Na^+ conductance.
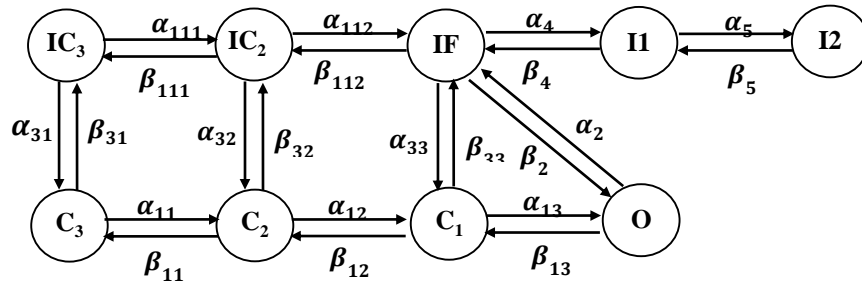
Figure 3-6 The Markov model of Na+ channels.

3.3.3 Experimental Protocols

In the electrophysiological experiments, we used standard pulse protocols to measure whole-cell current-voltage (I-V), steady state activation (SSA), steady state inactivation (SSI) and recovery from fast inactivation (REC) of Na^+ channels (see protocol details in the next section). However, there are slight differences in cell preparation and solutions used between Rasmusson's and our electrophysiological experiments. Notably, the reverse potential E_{Na} in our experiments is 20.5mV, instead of 39 mV.

As such, we adjusted the extracellular Na^+ concentration $[Na^+]_o$ from $140,000\,\mu M$ to $66,000\,\mu M$ in the computer model to match our experimental setting. All other parameters stay the same as given in the Bondarenko and Rasmusson et al [31]. The original values of transition rates in the matrix **A** are used as initial guesses in the process of model calibration. During computer experiments, we followed the same pulse protocols to identify 2 sets of optimal values of transition rates in the matrix **A** that minimize the discrepancy between the responses from the simulation model (i.e., the 9-state Markov model) and 2 sets of experimental data (i.e., control vs. reduced sialylation conditions).

Experimental data were collected from the left ventricular apex of adult (12-14 weeks old) male mice homozygous for the normal ST3Gal4 gene (WT, n=11) and for the ST3Gal4 null-transgene (ST3Gal4$^{-/-}$, n=13) as described by us previously [15]. ST3Gal4 is a uniformly expressed beta-galactoside alpha-2,3-sialyltransferase 4 (ST3Gal4) that is responsible for adding terminal sialic acids in the α2-3 configuration to N- and O-glycans. The pulse protocols used in both physical and computer experiments are illustrated in Figure 3-7 and described in the online supplement and as described in Ednie et al. [15]. The data points in Figure 3-10 ~ Figure 3-12 were as reported in our previous report [15].
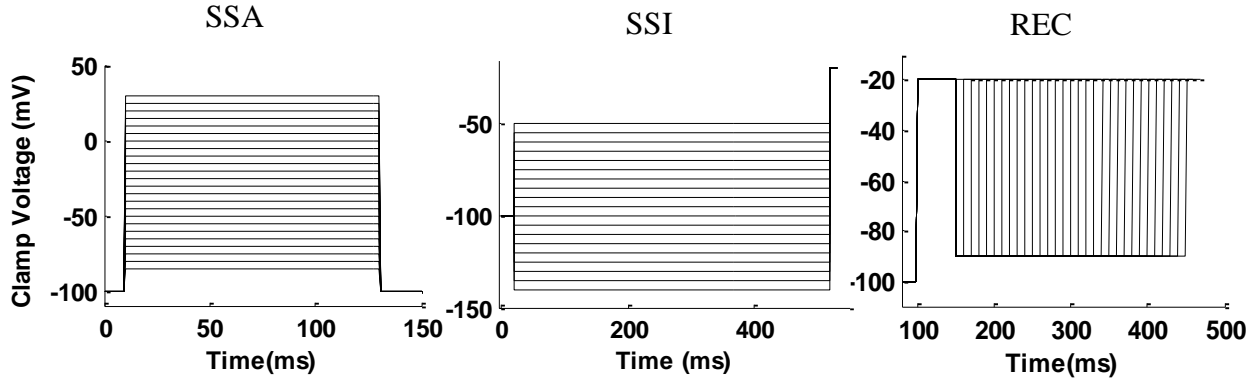
Figure 3-7 Standard pulse protocols of SSA, SSI and REC.

Current Density-Voltage Relationships and Steady-State Activation (SSA) are measured using the protocols described as following. Cells were held at -100mV, stepped to a series of voltage (from -85mV to +30m in 5 increments) for 120ms, and then stepped back to -100mV (see Figure 3-7). Each voltage step was separated by 1.5 seconds. The Na^+ conductance (G) is determined as $G = I_{peak}/(V_c - E_{Na})$, where I_{peak} is the peak of Na^+ currents elicited at each clamp voltage V_c. The current I_{Na} elicited from each test pulse is divided by the cell capacitance to report current density as A/F. The current density-voltage relationship is obtained by plotting the current density with respect to the clamp voltage. The maximum conductance G_{max} generated by each cell was used to normalize the data. Conductance-voltage relationships were fit with a Boltzmann equation and the fraction of maximal conductance is:

$$G/G_{max} = \frac{1}{1 + \exp(-(V - V_a)/K_a)}$$

where V is the membrane potentials, V_a is the half-activation potential, K_a is the slope factor. The normalized data were averaged with those from the other cells to calculate the resulting average G–V curves.

Steady-state inactivation (SSI) is collected following the below protocol. Cells were held at -100 mV and then pre-pulsed to conditioning voltages ranging from -140 mV to -65 mV in 5 mV

69

increments for 500 ms. Following the conditioning pulses, the cells were depolarized to -20 mV for 10 ms (see Figure 3-7). The maximum current generated by each cell was used to normalize the data, and then fit to a single Boltzmann distribution, from which the mean $V_i \pm$ SEM and $K_i \pm$ SEM values were determined. The fraction of maximal currents is:

$$I/I_{max} = \frac{1}{1 + \exp((V - V_i)/K_i)}$$

where I/I_{max} is the ratio of each current to the maximum current, V is the membrane potential, V_i is the voltage of half-inactivation, K_i is the slope factor.

Recovery from Fast Inactivation (REC) is measured by the protocol describe here. As shown in Figure 3-7, cells were held at a voltage of -90mV for a duration of 10ms and then followed by the first depolarization to -20mV for 50ms (the first pulse). The membrane potential then returned to -90mV for a variable duration from 10ms to 300ms with 10ms increments followed by a second depolarization to -20mV for 50ms (the second pulse). The peak currents elicited from the second pulse to -20 mV was normalized to the current from the initial pulse to -20 mV for measuring the recovery from fact inactivation of Na^+ channels [15].

Cellular Refractory Period is modeled using the same protocol in physical experiments. Cells were first injected with a 1.4ms 80 pA/pF stimulus current to excite the first AP. The first stimulation is followed by a second pulse 5ms later and then each additional pulse at an incremental time interval of 5ms until the emergence of the second similar AP [15]. The time interval between 2 similar APs is used to estimate the refractory period.

Computer models were implemented using the MATLAB R2012a software from MathWorks (Natick, MA, USA) in a Windows 7 (Microsoft, Redmond, WA, USA) 64-bit machine. Computer experiments follow the same pulse protocols as in-vitro experiments to compute the model

responses and to calibrate in-silico models. The models of cardiac cells and Na^+ ion channels are

solved with the use of Ode15s solver at a maximal step size of 1ms.

Table 3-1 Transition rates of the Markov Model.

Transition Rates (ms^{-1})
α_{11}=3.802(0.1027exp(-(V+x_1)/17.0) +0.20exp(-(V+ x_1)/150.0))$^{-1}$ β_{11}= 0.1917exp(-(V+x_2)/20.3) α_{12}=3.802(0.1027exp(-(V+ x_3)/15.0) + 0.23exp(-(V+ x_3)/150.0))$^{-1}$ β_{12}= 0.20exp(-(V+x_4)/20.3) α_{13}=3.802(0.1027exp(-(V+ x_5)/12.0) + 0.25exp(-(V+ x_5)/150.0))$^{-1}$ β_{13}= 0.22exp(-(V+x_6)/20.3) α_{111}=3.802(0.1027exp(-(V+x_7)/17.0) + 0.20exp(-(V+ +x_7)/150.0))$^{-1}$ α_{112}=3.802(0.1027exp(-(V+ x_8)/15.0) + 0.23exp(-(V+x_8)/150.0))$^{-1}$ β_{111}= 0.1917exp(-(V+x_9)/20.3) β_{112}= 0.20exp(-(V+x_{10})/20.3) α_{31}= 7.0e-7exp(-(V+x_{11})/(7.7+x_{23})) β_{31} = 0.0084 +x_{12}+ 2e-5(V+7.0) α_{32}= 7.0e-7exp(-(V+x_{13})/ (7.7+x_{24})) β_{32} = 0.0084 +x_{14}+ 2e-5(V+7.0) α_{33}= 7.0e-7exp(-(V+x_{15})/(7.7+x_{25})) β_{33} = 0.0084 + x_{16}+2e-5(V+7.0) α_2= 0.188495exp(-(V+x_{17})/(16.6+x_{22}) + 0.393956) β_2 = α_{13} α_2 α_{33}/(β_{13} β_{33}) α_4= x_{18} $\alpha_2$1e-3 β_4 = $x_{19}\alpha_{33}$ α_5= $x_{20}\alpha_2$/95000 β_5 = $x_{21}\alpha_{33}$/50

3.4   Results

3.4.1 Parameter Screening

As shown in Section 3.2, the 9-state Markov model of Nav channels involves 22 transition rates,

each of which is voltage-sensitive. Table 3-2 shows the detailed model of 22 transition rates. We

performed a preliminary sensitivity analysis to screen parameters that have potential impacts on

the model responses from three pulse protocols, i.e., SSA, SSI and REC. As shown in Table 3-1, we empirically identify a set of 25 potential parameters for further screening (i.e., $x_i, i = 1, \cdots, 25$). The screening design is aimed at identifying a low-dimensional set of important control variables (i.e., sensitive to the model responses to pulse protocols) from the high-dimensional set of *potential model parameters* so as to facilitate the process of statistical metamodeling.

Table 3-2   Experimental parameters and levels in transition rates.

	0	+1	-1		0	+1	-1
x_1	2.5	7.5	-2.5	x_{14}	0	0.001	-0.001
x_2	2.5	7.5	-2.5	x_{15}	7	12	2
x_3	2.5	7.5	-2.5	x_{16}	0	0.001	-0.001
x_4	-2.5	2.5	-7.5	x_{17}	7	12	2
x_5	2.5	7.5	-2.5	x_{18}	1	10	1
x_6	-7.5	-2.5	-12.5	x_{19}	1	10	1
x_7	2.5	5	0	x_{20}	1	10	1
x_8	2.5	7.5	-2.5	x_{21}	1	10	1
x_9	2.5	5	0	x_{22}	0	1.66	-1.66
x_{10}	-2.5	2.5	-7.5	x_{23}	0	1	-1
x_{11}	7	12	2	x_{24}	0	1	-1
x_{12}	0	0.001	-0.001	x_{25}	0	1	-1
x_{13}	7	12	2				

In order to reduce the computational cost, we adopted a 1024-run 2_V^{25-15} fractional factorial design for the sensitivity analysis of parametric effects on response functions. The resolution ensures that the main effects are strongly clear and the two-factor interactions are clear. Each parameter is varied at two levels of high (+1) and low (-1). Table 3-2 shows the values of each parameter at +1 and -1 levels, which are empirically determined based on the original values (0) in the Bondarenko and Rasmusson et al. [31].

Notably, the computational speed for each run in the SSA, SSI and REC experiments is about 1.90s, 4.20s and 8.06s, respectively. A full factorial design (FD) will require 2^{25} runs to screen

the effect of all possible combinations of +1's and -1's, which is computationally expensive and time consuming. As such, the full factorial design is not efficient, even infeasible, for a high-dimensional space of parameters. As shown in Table 3-3, the time durations of full FD are 1.77e4 hrs, 3.91e4 hrs and 7.51e4 hrs for SSA, SSI and REC experiments, respectively. However, the fractional FD is more efficient, and only need 32.42mins, 71.68mins and 137.56mins.

Table 3-3   Comparison of computational time for screening designs.

	Runs	SSA	SSI	REC
Unit time/ run	1	1.90s	4.20s	8.06s
Full FD	2^{25}	1.77e4 hrs	3.91e4 hrs	7.51e4 hrs
Fractional FD	2^{10}	32.42 mins	71.68 mins	137.56 mins

$*$ s: second; hrs: hours; mins: minutes

After obtaining computed responses from the 1024-run experiments on computer models, we estimated the factorial effects of parameters using the linear model. Figure 3-8 shows the half-normal probability plots for factorial effects of 25 parameters in SSA, SSI and REC protocols, respectively. Note that half-normal probability plot is a graphical method to test the significance of factorial effects. The significant effects will fall above the straight line of small factorial effects and appear in the upper right corner of the plot. As shown in Figure 3-8, the set of parameters $\{x_1, x_2, x_3, x_4, x_5, x_6, x_{17}, x_{22}\}$ has significant effects for steady-state activation. Similarly, $\{x_{11}, x_{12}, x_{23}\}$ and potentially $\{x_{13}, x_{14}, x_{24}\}$ are significant on the responses of steady-state inactivation. In addition, the set of parameters $\{x_{11}, x_{12}, x_{15}, x_{18}, x_{19}, x_{23}, x_{25}\}$ has significant impacts on the recovery from fast inactivation.

In addition to half-normal plots, we used the Lenth's method [32] to quantitatively test effect significance in the experiments. The pseudo standard error (PSE) of factorial effects $\hat{\beta}_i's$ is calculated as:

$$\text{PSE} = 1.5 \times \underset{\{|\hat{\beta}_i| < 2.5 s_0\}}{\text{median}} |\hat{\beta}_i|$$

73
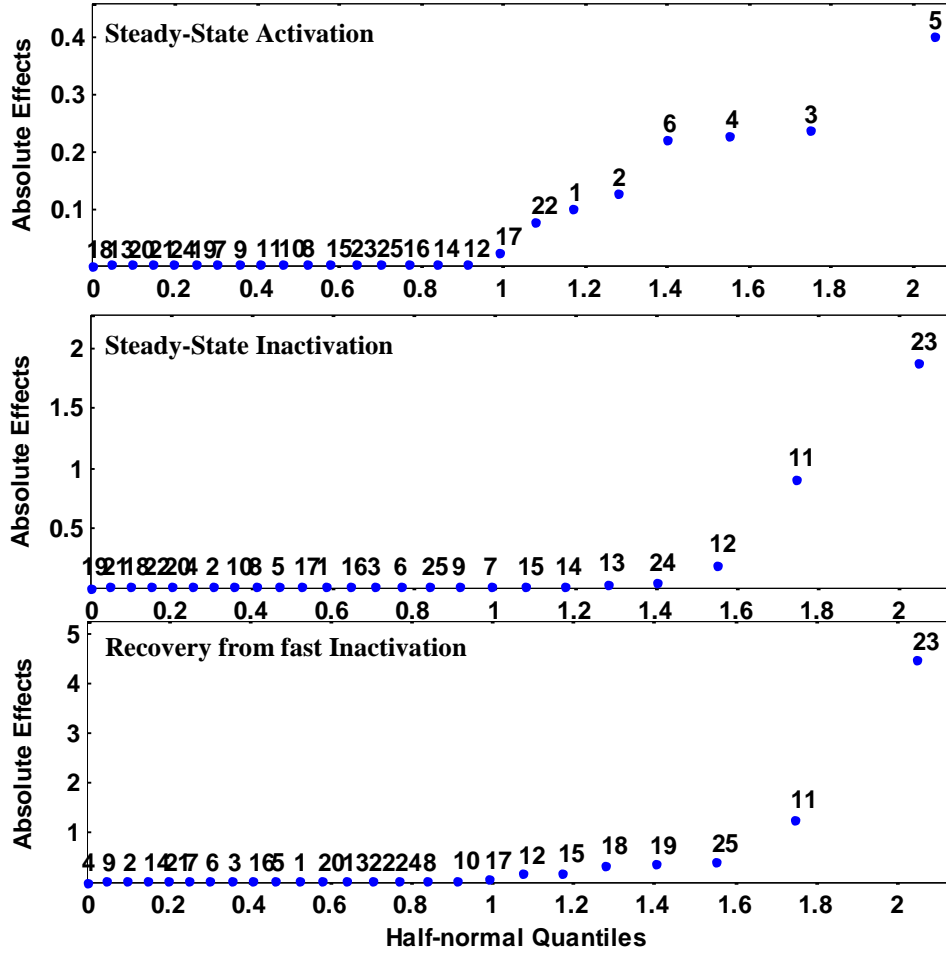
Figure 3-8 Half-normal probability plots for factorial effects of 25 model parameters in SSA, SSI and REC protocols.

where $s_0 = 1.5 \times \text{median}|\hat{\beta}_i|$. Note that PSE is an estimator of the standard deviation of $\hat{\beta}_i's$.

After dividing the $\hat{\beta}_i's$ by the PSE, we obtain the t-like statistics:

$$t_{PSE,i} = \frac{\hat{\beta}_i}{PSE}$$

Under the null hypothesis H_0 that all $\hat{\beta}_i's$ are not significant, we have the critical region:

$$prob(|t_{PSE,i}| > \mu_\alpha|H_0) = \alpha$$

where μ_α is the critical value at the significant level of α. An effect $\hat{\beta}_i$ is declared to be significant

if $|t_{PSE,i}|$ is greater than the critical value μ_α. The critical value of Lenth's method ($\mu_\alpha = 4.82$) at

a significant level ($\alpha = 0.001$) is available in most statistical software, e.g. SAS, Minitab.

The quantitative test confirms the results obtained from the graphical method and identifies three sets of control variables:

$$x_{SSA} = \{x_1, x_2, x_3, x_4, x_5, x_6, x_{17}, x_{22}\}$$

$$x_{SSI} = \{x_{11}, x_{12}, x_{13}, x_{14}, x_{23}, x_{24}\}$$

$$x_{REC} = \{x_{11}, x_{12}, x_{15}, x_{18}, x_{19}, x_{23}, x_{25}\}$$

Figure 3-9 shows the sensitivity plot of transition rates in SSA, SSI and REC protocols. The results of screening experiments show that α_{11}, β_{11}, α_{12}, β_{12}, α_{13}, β_{13}, and α_2 have greater impacts on SSA, but are less sensitive to SSI and REC. It is also shown that α_{31}, β_{31}, α_{32} and β_{32} are more sensitive to the SSI than other transition rates, and have similar impacts on REC. In addition, we found that α_{33}, α_2, α_4 and β_4 are sensitive to the REC protocols.
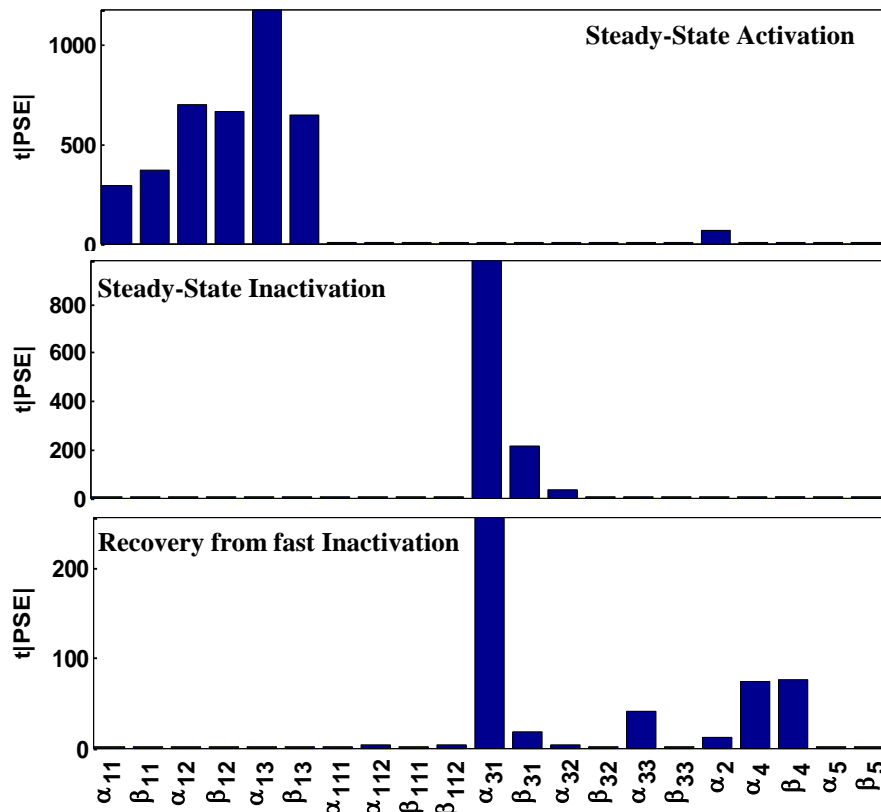

Figure 3-9 Sensitivity of transition rates in SSA, SSI and REC protocols.

Based on the results of screening experiments, we categorized the control variables into two groups. The first group includes those variables sensitive to SSA (i.e., $x_{SSA} = \{x_1, x_2, x_3, x_4, x_5, x_6, x_{17}, x_{22}\}$), and the second group includes those variables sensitive to both SSI and REC, i.e.,

$$x_{SSI+REC} = \{x_{11}, x_{12}, x_{13}, x_{14}, x_{15}, x_{18}, x_{19}, x_{23}, x_{24}, x_{25}\}$$

Therefore, the high-dimensional space of parameters is reduced to two sets of low-dimensional control variables. In addition, the problem of multi-objective optimization is decomposed into modular optimization formulations with a low-dimensional space of control variables.

3.4.2 Steady State Activation

Furthermore, we approximated the SSA discrepancy between computer model and electrophysiological data using the easy-to-evaluate statistical metamodels. First, we used the maximin Latin Hypercube Design (also see Section 3.2.2) to generate 20 design points of SSA control variables $x_{SSA} = \{x_1, x_2, x_3, x_4, x_5, x_6, x_{17}, x_{22}\}$, and then run the computer model to compute the responses. We fit the Gaussian Process metamodel to the data, then the metamodel is iteratively updated by adding a new design point where the probability to minimize model discrepancy is the highest. This process iterates until the SSA discrepancy is lower than a minimal tolerance value (i.e., MinTol=0.004 in this present study).

Figure 3-10 show steady state activation and inactivation under WT (i.e., control) and ST3Gal4^{-/-} in ventricular myocytes. It may be noted that the SSA in ST3Gal4^{-/-} myocytes is shifted toward a more depolarized potential than the WT. The experimental results show the shift of ~5mV. As shown in Figure 3-10, the SSA relationships from computer model match the trend of experimental data. It is remarkable that metamodel-based optimization converges to the minimum of the response surface very quickly (~100 iterations).
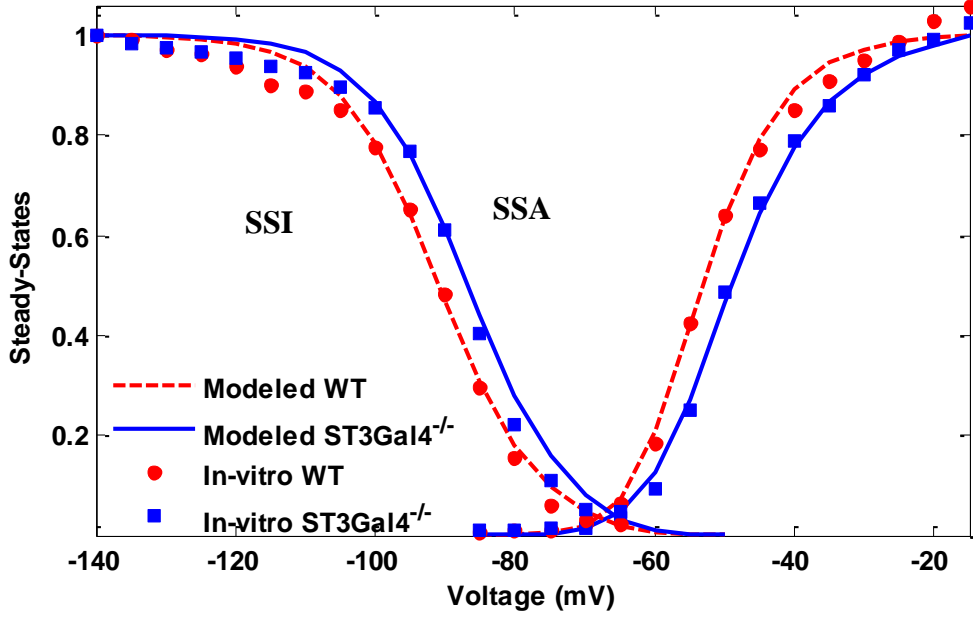
Figure 3-10 Steady state activation and inactivation for wild-type and ST3Gal4$^{-/-}$ conditions.

3.4.3 Steady State Inactivation and Recovery from Fast Inactivation

As mentioned in Section 3.4.1, we found that there are some common parameters sensitive to both SSI and REC.

$$x_{SSI} = \{x_{11}, x_{12}, x_{13}, x_{14}, x_{23}, x_{24}\}$$

$$x_{REC} = \{x_{11}, x_{12}, x_{15}, x_{18}, x_{19}, x_{23}, x_{25}\}$$

Therefore, we will minimize the model discrepancy for both SSI and REC protocols in the second stage of the optimization process. The combined set of control variables is:

$$x_{SSI+REC} = \{x_{11}, x_{12}, x_{13}, x_{14}, x_{15}, x_{18}, x_{19}, x_{23}, x_{24}, x_{25}\}$$

Statistical metamodels are constructed to approximate the relationship between $x_{SSI+REC}$ and model discrepancy (i.e., between experimental data and model responses under both SSI and REC protocols). Similarly, we used the statistical model as a surrogate to iteratively search a new design point where the probability to minimize model discrepancy is the highest. The original values of control variables $x_{SSI+REC}$, given in the Bondarenko and Rasmusson et al [31], are used as initial guesses in the process of model calibration. The minimal tolerance of SSI+REC discrepancy is set

77

to be 0.04. Note that SSI+REC experiments take more iterations (~1000 iterations) than SSA in the process to identify the optimal values of control variables because of the higher dimension of design space as well as two joint constraints of SSI+REC protocols.

However, statistical metamodeling and sequential design significantly improve the speed of convergence. As mentioned, if we treat the computer model as a blackbox, traditional linear and nonlinear optimization methods become very difficult or even infeasible, for calibrating the model in the high-dimensional design space. It is worth mentioning that the time cost to evaluate 1000 design points is only 0.040 seconds for the statistical GP model, but 2.75 hours for the computer model. Hence, it is a significant advantage to adopt the statistical metamodeling and sequential design strategy of computer experiments, especially for large-scale simulation models that are computationally expensive and time consuming.
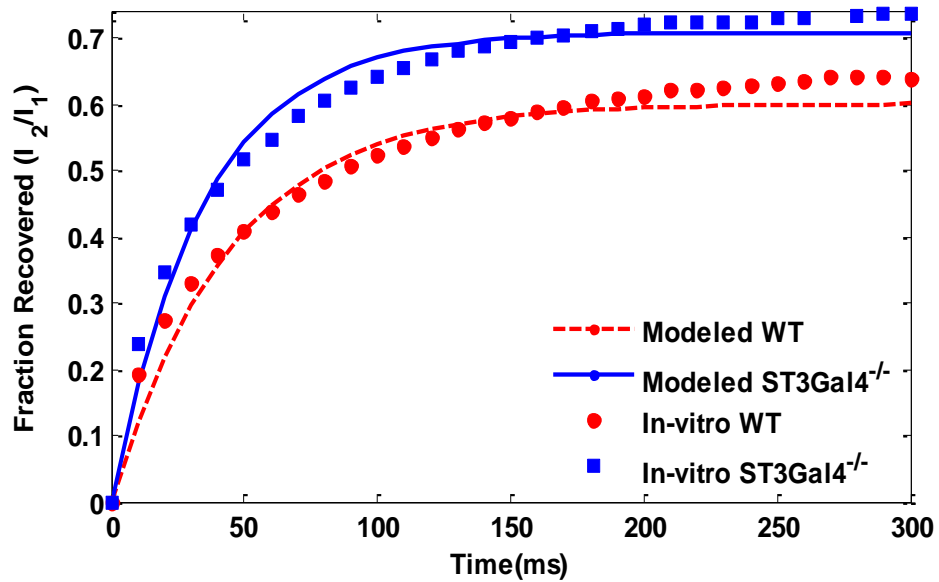

Figure 3-11 Recovery from fast inactivation of WT and ST3Gal4$^{-/-}$ cells.

Figure 3-10 shows that the calibrated model captures SSI relationships in the experimental data for both WT and ST3Gal4$^{-/-}$ myocytes. As shown in Figure 3-10, there is a depolarizing shift of ~4 mV in voltage-dependent SSI for ST3Gal4$^{-/-}$ myocytes compared to WT myocytes. This

indicates that ST3Gal4 gene deletion leads to the requirement of a greater depolarization for the inactivation of the Nav channels. In addition, Figure 3-11 shows that the recovery from fast inactivation from the computer model fits the experimental data. However, there are slight misfits in some portions of REC data due to the random effects in real-world electrophysiological experiments.

Table 3-4 Optimal values of control variables for WT and ST3GAL4$^{-/-}$ cells.

	WT	ST3Gal4$^{-/-}$		WT	ST3Gal4$^{-/-}$
x_1	16.3036	38.9756	x_{14}	0.0055	0.0041
x_2	23.6605	27.6129	x_{15}	28.6912	29.3783
x_3	8.0636	8.2235	x_{17}	12.3515	16.9279
x_4	14.8590	10.7454	x_{18}	3.3553e2	8.4621e2
x_5	31.0464	25.6248	x_{19}	4.3636e3	7.4270e3
x_6	-0.2266	-6.6274	x_{22}	-3.3326	-3.1787
x_{11}	19.6572	17.0064	x_{23}	-0.4042	-0.5177
x_{12}	0.0052	0.0046	x_{24}	-0.4496	-0.5496
x_{13}	28.3559	31.8518	x_{25}	-0.1292	-1.2045

Table 3-4 shows optimal values of control variables, x_{SSA}, x_{SSI}, and x_{REC} for the calibrated models of Nav channels isolated from WT and ST3Gal4$^{-/-}$ myocytes. Note that there are significant differences between these two sets of optimal values for control variables. However, calibrated models best fits the WT and ST3Gal4$^{-/-}$ experimental data with standard pulse protocols (i.e., SSA, SSI, and REC).

3.4.4 Model Validation

These two set of parameters, shown in Table 3-4, yield best fit of WT and ST3Gal4$^{-/-}$ experimental data obtained from SSA, SSI and REC protocols. As such, we have two initial versions of calibrated models for WT and ST3Gal4$^{-/-}$ myocytes. In order to validate calibrated models, we further measured model responses of current-voltage relationships and cellular

refractory period, and made a comparison with real experimental data, which are detailed as follows.

Current density-voltage relationship is modeled in this study using conventional protocols. Following the pulse protocols in Section 3.3.3, we computed the response of I_{Na} from calibrated models (both ST3Gal4$^{-/-}$ and WT myocytes) for each test pulse. The current density-voltage relationship is obtained by plotting the current density with respect to the clamp voltage.

As shown in Figure 3-12, I_{Na} current densities from the model of ST3Gal4$^{-/-}$ myocytes are bigger than in WT myocytes at relatively small depolarization, i.e., when cells are held at -100mv and then stepped to the voltages between -70mv and -30mv. However, there are no significant effects at greater depolarization. Note that the discrepancy of current density-voltage relationships between computer models and experimental data is minimized for both ST3Gal4$^{-/-}$ and WT myocytes. These results showed that computer models are well-calibrated and suggested that the gating dynamics of Nav channels differently with ST3Gal4 expression.
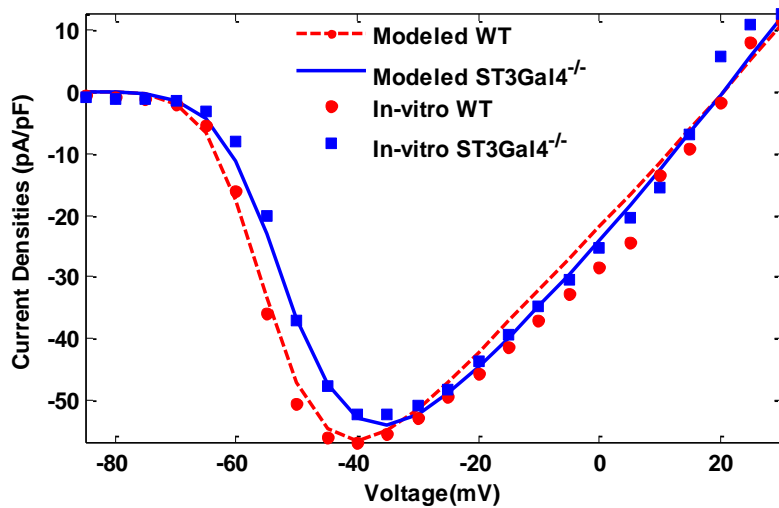

Figure 3-12 Current density-voltage relationships.

Cellular Refractory Period is compared between ST3Gal4$^{-/-}$ and WT conditions. We have also integrated the calibrated models of Na^+ channels into the ventricular cell model to predict whether

and how ST3Gal4 gene deletion influences the electrical activity of cardiac cells. It should be noted that the Na^+ channels are responsible for the excitation of cells and also contributes to electrical conduction in tissues. Na_v recovery from fast inactivation is closely pertinent to the cellular refractory period.

Figure 3-13 shows the responses of ventricular cell models using the refractory-period protocol (also see Section 3.3.3). Notably, there are significant differences in the cellular refractory periods from computer models of ST3Gal4^{-/-} and WT myocytes. However, resting membrane potentials and AP durations do not show significant differences between computer models of ST3Gal4^{-/-} and WT myocytes. In addition, our experimental results demonstrated that the model of ST3Gal4^{-/-} myocytes yields a 28.5ms shorter refractory period than WTs. In contrast, our electrophysiological experiments also show that the refractory periods are approximately 110.2 ± 10.0 ms (n=13) for ST3Gal4^{-/-} cells, and 139.8 ± 8.6 ms for WTs (n=11), i.e., 29.6ms shorter refractory period in ST3Gal4^{-/-} cells [15]. These results show the validity of computer models to capture the mechanistic details of Na^+ electrical signaling, as well as the effectiveness of the proposed algorithms for calibrating computer models.
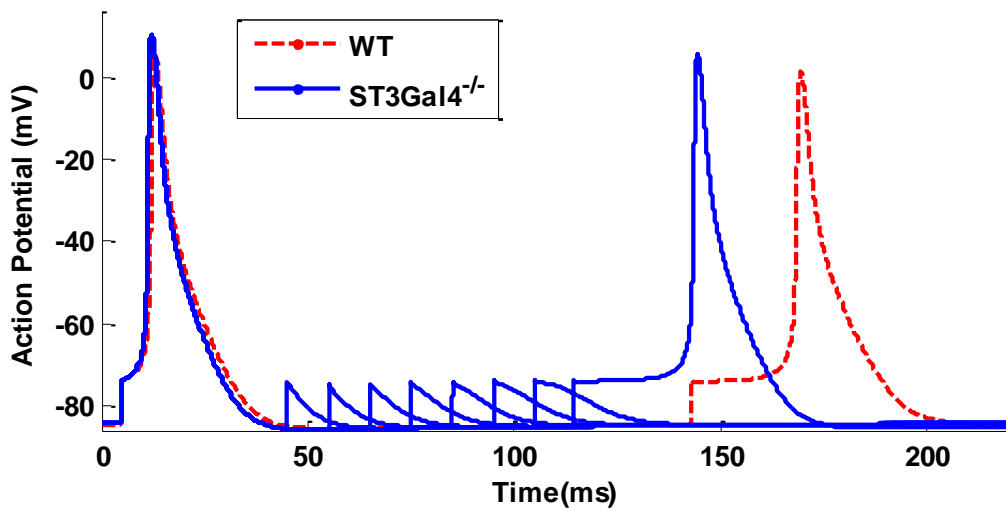

Figure 3-13 Cellular refractory periods from computer models of ST3Gal4^{-/-} and WT myocytes. (WT: 138.0ms, ST3Gal4^{-/-}: 109.5ms)

3.4.5 State Transitions in Nav Channels

Although electrophysiological experiments can observe aberrant electrical signaling in reduced sialylation with the use of standard pulse protocols, understanding mechanistic details of ST3Gal4$^{-/-}$ pathological variations in I_{Na} and AP is difficult without performing in-silico studies. In-vitro experiments can measure ionic currents I_{Na} and AP with voltage and current clamp protocols, but preclude us from determining directly the change in transitions among molecular states (e.g., open, close, intermediate inactivated, and fast inactivated states) and their systematic contributions to AP variations. In this section, we will use the calibrated in-silico models to predict the variations of mechanistic details in the state transitions and distributions of Na^+ Channels for both ST3Gal4$^{-/-}$ and WT myocytes.

As shown in Figure 3-14, there are significant variations in the state transitions of Na^+ Channels under ST3Gal4$^{-/-}$ and WT conditions. During the AP upstroke (Figure 3-14a), ST3Gal4$^{-/-}$ channels open slightly faster and wider than WT (i.e., 20% vs. 15%). This also leads to a shorter time-to-peak value for ST3Gal4$^{-/-}$ channels. It may also be noted that WT channels have a higher probability in the fast inactivation (IF), 38% vs. 27%, but a slower transition to the intermediate inactivation (I1) than ST3Gal4$^{-/-}$ channels, i.e., 2% vs. 4%.

At the peaks of APs (Figure 3-14b), ST3Gal4$^{-/-}$ channels show a more significant probability to stay in the intermediate inactivation (I1) than WTs (i.e., 67% vs. 40%), whereas most of WT channels are still in the state of Fast Inactivation (IF). This indicates that ST3Gal4$^{-/-}$ channels have a faster transition from the IF to the I1 state, and thereby a smaller probability of remaining in the IF state than WT channels (i.e., 27% vs. 55%). Also, it may be noted that both channels have a small probability (see Figure 3-14 b) in the open state (6% in ST3Gal4$^{-/-}$ channels and 4% in WT channels).
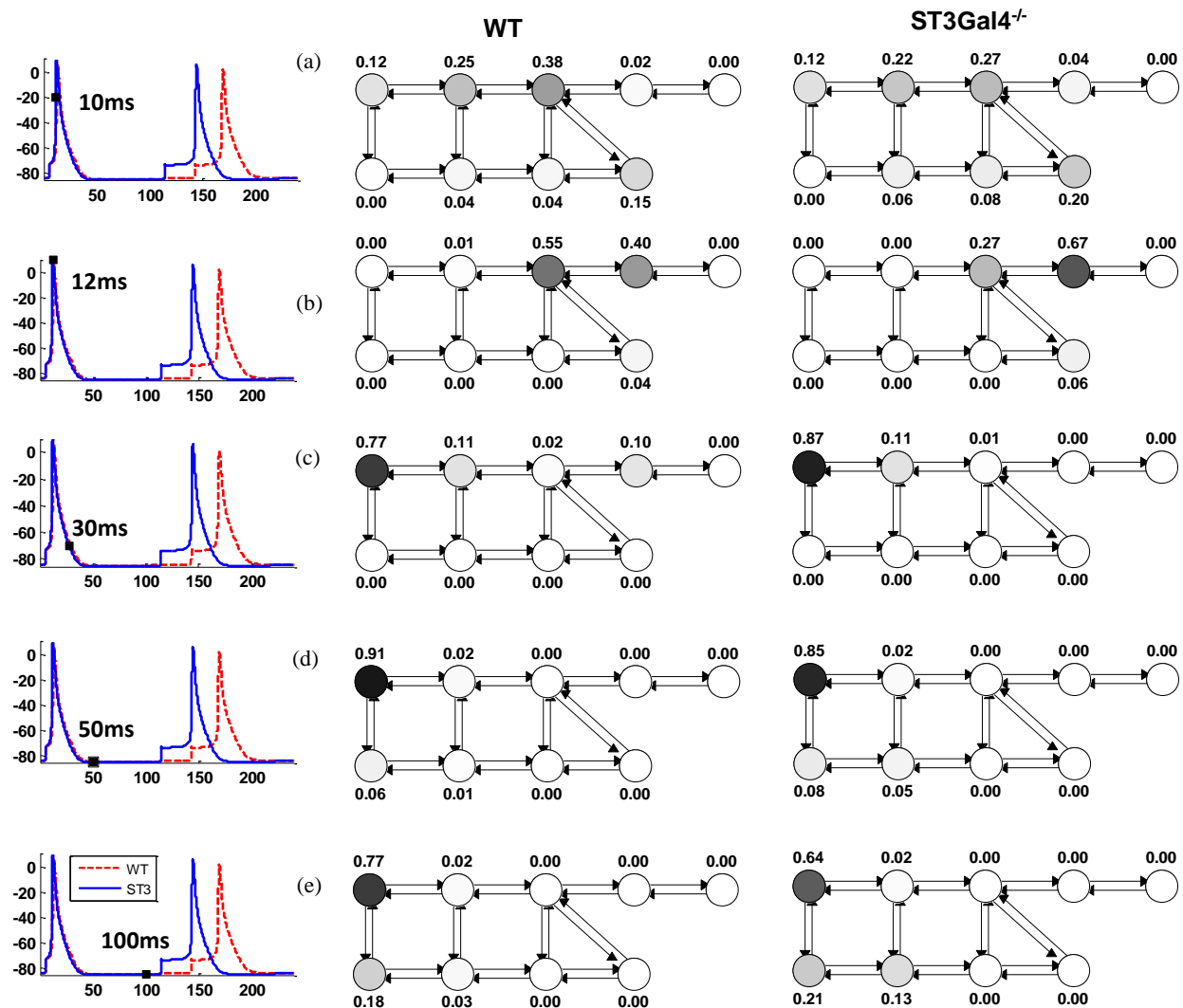
Figure 3-14 State transitions of sodium channels during the course of action potential under WT and ST3Gal4$^{-/-}$ conditions.

In the late repolarization phase (Figure 3-14c), all the ST3Gal4$^{-/-}$ channels exited the state of intermediate inactivation (I1), but WT channels have 10% remaining in the I1 state. Most importantly, ST3Gal4$^{-/-}$ channels have a higher probability in the closed-inactivation state (IC3) than WTs (i.e., 87% vs. 77%). This suggests that ST3Gal4$^{-/-}$ channels have a faster transition from I1 state to IC3 state.

After 50ms (Figure 3-14d), both ST3Gal4$^{-/-}$ and WT APs are at the end of the repolarization phase and reach the level of resting potential. In addition, both ST3Gal4$^{-/-}$ and WT channels have completely exited the open, fast inactivation and intermediate inactivation states. Figure 3-14c shows that ST3Gal4$^{-/-}$ channels have a smaller probability of remaining in the closed-inactivation state (IC3) than WTs (i.e., 85% vs. 91%). Further, it is shown that ST3Gal4$^{-/-}$ channels enters the close state earlier than WTs (ST3Gal4$^{-/-}$: C3=8% and C2=5%; WT: C3=6% and C2=1%).

This trend continues for ST3Gal4$^{-/-}$ and WT channels after 100ms (Figure 3-14e), and more and more ST3Gal4$^{-/-}$ channels enters the close state earlier than WTs. This indicates that ST3Gal4$^{-/-}$ channels get ready for the second stimulation earlier than WTs. Hence, in-silico models provide the underlying mechanistic details that explain why ST3Gal4$^{-/-}$ cells have shorter refractory periods.

3.5 Conclusions

This study presents a new statistical metamodeling approach for efficient computer experiments and optimization of Na_v models to describe glyco-altered Na$_v$ gating kinetics in the ST3Gal4$^{-/-}$ heart. Note that voltage-gated sodium (Na_v) channel activity is responsible for the excitation of cells and also contributes to electrical conduction in tissues. In addition, Na_v ion channels are heavily glycosylated, with up to 35% of a mature protein's mass comprised of glycan structures. There is a set of >40 distinct forms of inherited human diseases of reduced glycosylation known as Congenital Disorders of Glycosylation, which often leads to severe cardiac deficits, but the mechanisms are not yet understood.

We have conducted a series of electrophysiological experiments to investigate whether and how reduced glycosylation affects Na$_v$ activity and cardiac electrical signaling. Our experiments provide two full sets of data; one under "control" (physiological, wild-type - WT) condition, and the other under the condition of reduced sialylation (pathology, ST3Gal4$^{-/-}$). Although we observed

aberrant electrical signaling in reduced sialylation, understanding mechanistic details of pathological variations in I_{Na} and AP is very difficult without performing in-silico studies.

This study presents our efforts to couple in-silico studies with the wealth of experimental data to model, mechanistically, how reduced glycosylation that occurs in the ST3Gal4$^{-/-}$ heart affects Na_v activity and cardiac electrical signaling. Note that computer model of Na_v channels and cardiac myocytes poses significant challenges for computer experiments and model calibration, including (1) the high dimensionality of design space, (2) nonlinear and non-convex model characteristics, (3) a variety of cardiac functional responses from pulse protocols, and (4) specific kinetics and physical constraints in cardiac ion channels and cells. If the computer model is treated as the black-box, traditional linear and nonlinear optimization methods have encountered many difficulties, even infeasible, for calibrating the model in the high-dimensional design space.

Hence, this present investigation employs the statistical metamodel as a surrogate for efficient and effective calibration of cardiac models. First, we designed the fractional factorial experiments to identify control variables that are sensitive to the model response functions, and thereby identifying a low-dimensional set of important control variables from the high-dimensional set of *potential model parameters* so as to facilitate the process of statistical metamodeling. Second, we develop the Gaussian Process models as the surrogates of expensive and time-consuming computer models and then identify the next best design point that yields the maximal probability of improvement. The improvement is defined as the discrepancy between real data and model outputs under standard pulse protocols. This process is iterated until convergence.

Experimental results demonstrated the efficiency and effectiveness of the proposed algorithms for calibrating computer models, especially for large-scale simulation models that are computationally expensive and time consuming. The process of model calibration quickly

85

converges (<1000 iterations) to the best fits of experimental data of SSA, SSI and REC relationships for both WT and ST3Gal4$^{-/-}$ conditions. In addition, we evaluated and validated the calibrated models with the use of current density-voltage relationships and cellular refractory period. These results show computer models effectively capture the mechanistic details of Na^+ gating dynamics and cellular electrical signaling. Further, we used the calibrated in-silico models to predict the variations of mechanistic details in the state transitions and distributions of Na^+ Channels for both ST3Gal4$^{-/-}$ and WT myocytes. In-silico models provide the underlying mechanistic details that explain why ST3Gal4$^{-/-}$ cells have shorter refractory periods than WTs, as well as why ST3Gal4$^{-/-}$ channels get ready for the second stimulation earlier than WTs.

This study made an attempt to bridge the gaps in statistical metamodeling between engineering and cardiac domains. As opposed to traditional linear and nonlinear optimization methods, this study presents a new sequential design of computer experiments for calibrating complex models of cardiac systems (e.g., Na^+ ion channels). The proposed methodology is generally extensible to many other disciplines that involve the simulation experiments on large-scale and expensive computer models.

3.6   References

[1]   P. J. Stocker and E. S. Bennett, "Differential Sialylation Modulates Voltage-gated Na+ Channel Gating throughout the Developing Myocardium," The Journal of General Physiology, vol. 127, pp. 253-265, March 01, 2006.

[2]   A. R. Ednie and E. S. Bennett, "Modulation of Voltage-Gated Ion Channels by Sialylation," Comprehensive Physiology, vol. 2, pp. 1269-1301, 2012.

[3]   E. Bennett, M. S. Urcan, S. S. Tinkle, A. G. Koszowski and S. R. Levinson, "Contribution of Sialic Acid to the Voltage Dependence of Sodium Channel Gating: A Possible Electrostatic Mechanism," The Journal of General Physiology, vol. 109, pp. 327-343, March 01, 1997.

[4]   E. S. Bennett, "Isoform-specific effects of sialic acid on voltage-dependent Na+ channel gating: functional sialic acids are localized to the S5-S6 loop of domain I," The Journal of Physiology, vol. 538, pp. 675-690, February 01, 2002.

[5]   D. Johnson and E. S. Bennett, "Isoform-specific Effects of the β2 Subunit on Voltage-gated Sodium Channel Gating," Journal of Biological Chemistry, vol. 281, pp. 25875-25881, September 08, 2006.

[6]   D. Johnson, M. L. Montpetit, P. J. Stocker and E. S. Bennett, "The Sialic Acid Component of the ßl Subunit Modulates Voltage-gated Sodium Channel Function," Journal of Biological Chemistry, vol. 279, pp. 44303-44310, October 22, 2004.

[7]   Y. Zhang, H. A. Hartmann and J. Satin, "Glycosylation influences voltage-dependent gating of cardiac and skeletal muscle sodium channels" J. Membr. Biol., vol. 171, pp. 195-207, Oct 1, 1999.

[8]   C. A. Ufret-Vincenty, D. J. Baro, W. J. Lederer, H. A. Rockman, L. E. Qui ñones and L. F. Santana, "Role of Sodium Channel Deglycosylation in the Genesis of Cardiac Arrhythmias in Heart Failure," Journal of Biological Chemistry, vol. 276, pp. 28197-28203, July 27, 2001.

[9]   M. L. Montpetit, P. J. Stocker, T. A. Schwetz, J. M. Harper, S. A. Norring, L. Schaffer, S. J. North, J. Jang-Lee, T. Gilmartin, S. R. Head, S. M. Haslam, A. Dell, J. D. Marth and E. S. Bennett, "Regulated and aberrant glycosylation modulate cardiac electrical signaling," Proceedings of the National Academy of Sciences, vol. 106, pp. 16517-16522, September 22, 2009.

[10]   J. Jaeken and G. Matthijs, "Congenital disorders of glycosylation: a rapidly expanding disease family " Annu. Rev. Genomics Hum. Genet., vol. 8, pp. 261-278, 2007.

[11]   E. Footitt, A. Karimova, M. Burch, T. Yayeh, T. Dupre, S. Vuillaumier-Barrot, I. Chantret, S. Moore, N. Seta and S. Grunewald, "Cardiomyopathy in the congenital disorders of glycosylation (CDG): a case of late presentation and literature review," J. Inherit. Metab. Dis., pp. S313-9, 2009.

[12]   J. M. van de Kamp, D. J. Lefeber, G. J. Ruijter, S. J. Steggerda, N. S. den Hollander, S. M. Willems, G. Matthijs, B. J. Poorthuis and R. A. Wevers, "Congenital disorder of glycosylation type Ia presenting with hydrops fetalis " J. Med. Genet., vol. 44, pp. 277-280, Apr, 2007.

[13]   J. G. Leroy, "Congenital disorders of N-glycosylation including diseases associated with O- as well as N-glycosylation defects" Pediatr. Res., vol. 60, pp. 643-656, Dec, 2006.

[14]   H. H. Freeze, "Genetic defects in the human glycome " Nat. Rev. Genet., vol. 7, pp. 537-551, Jul, 2006.

[15]   A. R. Ednie, K. Horton, J. Wu and E. S. Bennett, "Expression of the sialyltransferase, ST3Gal4, impacts cardiac voltage-gated sodium channel activity, refractory period and ventricular conduction," J. Mol. Cell. Cardiol., vol. 59, pp. 117-127, 6, 2013.

[16] D. Du, H. Yang, S. Norring and E. Bennett, "In-Silico Modeling of Glycosylation Modulation Dynamics in hERG Ion Channels and Cardiac Electrical Signals," IEEE Journal of Biomedical and Health Informatics, vol. 18, pp. 205-214, 2013.

[17] D. Du, H. Yang, S. Norring and E. Bennett, "Multi-Scale Modeling of Glycosylation Modulation Dynamics in Cardiac Electrical Signaling," Engineering in Medicine and Biology Society (EMBC), Proceedings of 2011 Annual International Conference of the IEEE, pp. 104-107, August 30, 2011.

[18] C. E. Clancy and Y. Rudy, "Na+ Channel Mutation That Causes Both Brugada and Long-QT Syndrome Phenotypes: A Simulation Study of Mechanism," Circulation, vol. 105, pp. 1208-1213, March 12, 2002.

[19] D. R. Jones, "A taxonomy of global optimization methods based on response surfaces," Journal of Global Optimization, vol. 21, pp. 345-383, 2001.

[20] D. D. Frey and H. Wang, "Adaptive One-Factor-at-a-Time Experimentation and Expected Value of Improvement," Technometrics, vol. 48, pp. 418-431, 2006.

[21] M. F. Franklin, "Constructing Tables of Minimum Aberration Pn–m Designs," Technometrics, vol. 26, pp. 225-232, 1984.

[22] C. Daniel, "Use of half-normal plots in interpreting factorial two-level experiments," Technometrics, vol. 1, pp. 311-341, 1959.

[23] T. J. Santner, B. J. Williams and W. I. Notz, The Design and Analysis of Computer Experiments. New York: Springer, 2003.

[24] K. T. Fang, R. Li and A. Sudjianto, Design and Modeling for Computer Experiments. Boca Raton: Chapman and Hall, 2005.

[25] M. C. Kennedy and A. O'Hagan, "Bayesian calibration of computer models," Journal of the Royal Statistical Society: Series B (Statistical Methodology), vol. 63, pp. 425-464, 2001.

[26] P. Z. G. Qian and C. F. J. Wu, "Bayesian Hierarchical Modeling for Integrating Low-Accuracy and High-Accuracy Experiments," Technometrics, vol. 50, pp. 192-204, 2008.

[27] C. Chang and V. R. Joseph, "Model Calibration through Minimal Adjustments," Technometrics, vol. 56, no. 4, 2014.

[28] P. Z. G. Qian, C. C. Seepersad, V. R. Joseph, J. K. Allen and C. F. Jeff Wu, "Building Surrogate Models Based on Detailed and Approximate Simulations," Journal of Mechanical Design, vol. 128, pp. 668-677, June 7, 2005.

[29] P. Z. G. Qian, H. Wu and C. F. J. Wu, "Gaussian Process Models for Computer Experiments With Qualitative and Quantitative Factors," Technometrics, vol. 50, pp. 383-396, 2008.

[30]   C. E. Rasmussen and C. K. I. Williams, Gaussian Processes for Machine Learning. Cambridge: The MIT Press, 2006.

[31]   V. E. Bondarenko, G. P. Szigeti, G. C. L. Bett, S. Kim and R. L. Rasmusson, "Computer model of action potential of mouse ventricular myocytes," American Journal of Physiology - Heart and Circulatory Physiology, vol. 287, pp. H1378-H1403, September 01, 2004.

[32]   R. V. Lenth, "Quick and Easy Analysis of Unreplicated Factorials," Technometrics, vol. 31, pp. 469-473, 1989.

Chapter 4 In-Silico Modeling of Glycosylation Modulation Dynamics in K+ Ion Channels and Cardiac Signaling

Cardiac action potentials (AP) are produced by the orchestrated functions of ion channels. A slight change in ion channel activity may affect the AP waveform, thereby potentially increasing susceptibility to abnormal cardiac rhythms. Cardiac ion channels are heavily glycosylated, with up to 30% of a mature protein's mass comprised of glycan structures. However, little is known about how reduced glycosylation impacts the gating of K+ channels. Moreover, decomposing experimentally the joint K+ current is quite difficult because K+ channels activate at similar range of voltage, and share overlapping kinetics. The proposed decomposition method takes advantage of computer models of K+ channels, and describes the fine-grained details of specific currents. As such, it enables the interpretation of glycosylation modulation dynamics in the gating of each individual K+ channel. This work suggests new pharmaceutical targets for the glycan-altered cardiac diseases and potentially other cardiac disorders.

4.1 Introduction

Action potential (AP), the net change of transmembrane potential in a cardiac myocyte during a contraction cycle, is produced by the orchestrated function of ion channels. A slight change in ion channel activity may affect the AP waveform and electrical conduction, thereby potentially lead to severe cardiac disorders. Voltage-gated potassium (K_v) channels play significant role in forming the AP. The shape and the duration of the AP are determined by the activities of each individual K_v channels, and the diverse distribution of K_v channels has essential physiological

functions. In large mammals, there are different types of K_v isoforms that are responsible for different phases of the cardiac electrical activity. Figure 4-1 shows the AP waveforms of human (A) and mouse (B) ventricular myocytes and the currents that contribute to different phases of the APs. The two main K_v isoforms: $K_v 11.1$ and $K_v 7.1$ affect the ventricular repolarization by contributing to I_{Kr} and I_{Ks} currents during phase 2 through 3 of the AP [1, 2, 6]. The activities of these 2 isoforms enable long sustained K^+ currents that allow cardiac cells to stay at depolarization phase for a relatively long time. The 4 isoforms: $K_v4.2/K_v4.3$, $K_v1.5$ and $K_v2.1$ contribute to a rapid repolarization in mouse ventricles [3, 6]. $K_v4.3$ is also found in human ventricular mycytes, and is responsible for a smaller portion of repolarization [2, 4, 6]. In mouse ventricle, the phase 2 and 3 of the AP are controlled by the rapidly inactivating K^+ current I_{to}, which is contributed by the isoform of $K_v4.2/4.3$, and the slowly inactivating currents: I_{Kslow1}, and I_{Kslow2} which are likely conducted through $K_v1.5$ and $K_v2.1$ respectively [3, 6].
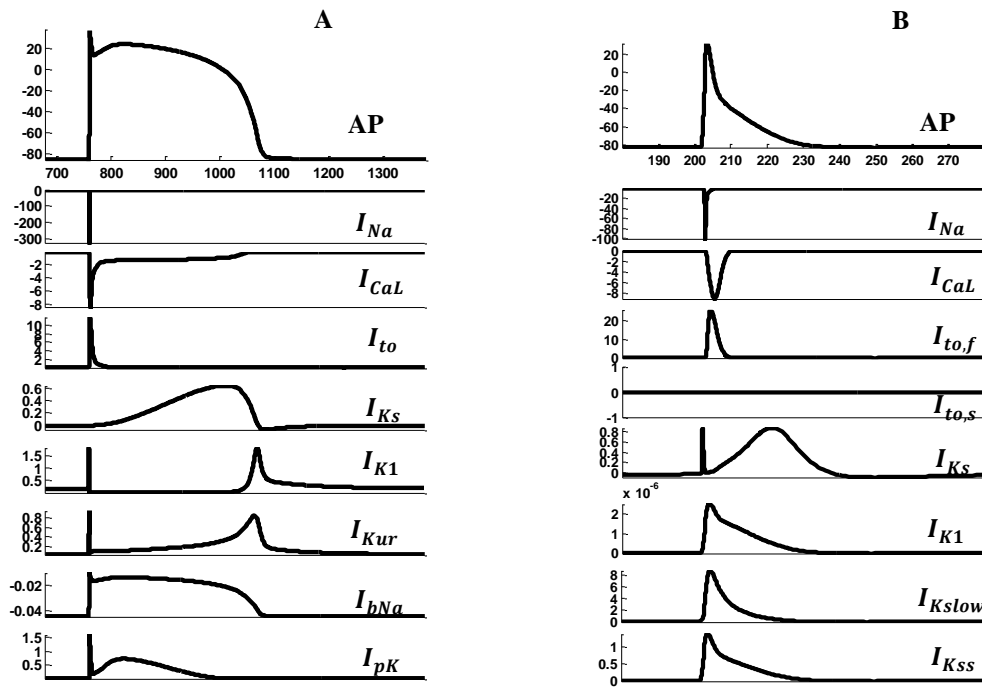

Figure 4-1 Modeled APs in human and mouse ventricular myocytes. Human AP is calculated with ten Tusscher et al. model [29], Mouse AP is calculated with Bondarenko et al. model [30].

Studies have shown that sialic acids have similar effect on K_v activities. As we mentioned in Chapter 2, Na_v channels can be extensively post-translationally modified by protein glycosylation through isoform-specific mechanisms [7-12]. The sialic acids have similar functional effects on K_v isoforms. In 1996 Thornhill et al., found that the $K_v1.1$ isoform in rat cardiac cells could be functionally affected by sialylation [13-15, 6]. Later, similar effects were observed at the single channel level [16]. The role of sialylation in $K_v1.2$ function was investigated through a novel approach, i.e. mutants were created where glycosylation sites were added to the channel compared with the function of healthy cells. This study found that N-linked deficient mutant led to a depolarizing shift in V_a, a broadening of the slope of the G-V curve and decreased channel kinetics [6,17]. Recently, Schwetz et al. investigated the effect of sialylation on the heterologously expressed K_v isoforms $K_v2.1$, $K_v4.2$ and K_v 4.3 [18].

In order to answer whether and how reduced glycosylation affects K_v activity and cardiac electrical signaling, in-vitro experiments were conducted to measure and characterize potassium currents. Although we observed aberrant electrical signaling in ST3Gal4$^{-/-}$ ventricular myocytes and across the ST3Gal4$^{-/-}$ ventricle, understanding mechanistic details of pathological variations in K^+ currents and AP is very challenging without performing in-silico studies. There are 6 different type of K^+ currents in mouse ventricular myocytes, i.e., a rapid transient outward K^+ current (I_{to}), a rapid delayed rectifier K^+ current (I_{Kr}), an ultra-rapidly activating delayed rectifier K^+ current (I_{Kur}), a non-inactivating steady-state K^+ current (I_{ss}), a very small slow delayed rectifier current (I_{Ks}), and a time-independent K^+ current (I_{K1}) [19]. Decomposing the joint K^+current, $I_{K,sum}$, experimentally is quite difficult because K_v channels activate at similar range of voltage, and share overlapping kinetics [20-22]. Experiments can measure the joint K^+ ionic currents and AP with voltage and current clamp protocols, but preclude us from determining

directly the systematic contributions of each individual K^+ current to AP variations. There is an urgent need to integrate computer models with experimental data to model the variations of state transitions under conditions of reduced sialylation, and the resulting changes in ionic currents and AP.

In this present study, we propose to couple in-silico studies with the wealth of data from our electrophysiological experiments to model, mechanistically, how reduced sialylation that occurs in the ST3Gal4$^{-/-}$ heart affects K_v channel activity and electrical signaling in the adult mouse ventricle. Indeed, computer models not only overcome practical and ethical limitations in physical experiments but also provide predictive insights into the underlying mechanisms.

4.2 Mouse Ventricular Models

In Chapter 3, we modeled the transition of molecular states in ST3Gal4-/- Na_v channels and myocytes, showing that glyco-gene defect affects Na_v channel activity and leads to shortened refractory periods. In-silico study showed the detailed state transitions under both ST3Gal4$^{-/-}$ and WT conditions. In addition, computer experiments predict how the changes at molecular level, i.e., Na_v channel level, affect the electrical activity at cellular level, i.e., altered channel activities cause shortened refractory periods in mouse ventricular myocytes. In this chapter, electrophysiological experiments have been conducted to measure how glyco-gene defect affects the K_v channel activity and APs of mouse ventricular myocytes. These experiments produced two sets of data; one under "control" (physiological, wild-type - WT) conditions, and the other under conditions of reduced sialylation (pathology, ST3Gal4$^{-/-}$). In this section, we will detail computer models that are used to describe mechanistic details of pathological variations in K_v channels and the AP of ventricular myocyte. With the computer model, changes in ion channels are modeled, and effect on cardiac function at cellular level is predicted.

4.2.1 Computer Model of Ventricular Myocyte

In this present investigation we applied the computer model of action potential of mouse ventricular myocytes from Bondarenko and Rasmusson et al [23]. The cellular AP is described by the ordinal differential equation:

$$-C_m \frac{dV}{dt} = I_{CaL} + I_{p(Ca)} + I_{NaCa} + I_{Cab} + I_{Na} + I_{Nab} + I_{NaK} +$$

$$I_{Kto,f} + I_{Kto,s} + I_{K1} + I_{Ks} + I_{Kur} + I_{Kss} + I_{Kr} + I_{Cl,Ca} + I_{stim}$$

where t is time, C_m is the cell capacitance, I_{stim} is the external stimulus current which activates the cell from the resting state. The transmembrane currents include the fast Na^+ current (I_{Na}), the L-type Ca^{2+} current (I_{CaL}), the rapidly recovering transient outward K^+ current ($I_{Kto,f}$), the slowly recovering transient outward K^+ current ($I_{Kto,s}$), the rapid delayed rectifier K^+ current (I_{Kr}), the ultrarapidly activating delayed rectifier K^+ current (I_{Kur}), the non-inactivating steady-state voltage-activated K^+ current (I_{Kss}), the time-independent inwardly rectifying K^+ current (I_{K1}), the slow delayed rectifier K^+ current (I_{Ks}), the Na^+/Ca^{++}exchange current (I_{NaCa}), the Na^+/K^+ pump current (I_{NaK}), the Ca^{2+}pump current ($I_{p(Ca)}$), the Ca^{2+}-activated Cl^- current, ant the background Ca^{2+} and Na^+ currents. Most ionic currents are modeled using Hodgkin-Huxley or Markov-based formulations, including the cell conductance, the gradients of membrane potential and gating dynamics. For details on all the ion-channel kinetics, see Bondarenko and Rasmusson et al [23].

The objective is to calibrate the model to describe the detailed mechanism of K_v channels and APs under both ST3Gal4^{-/-} and WT conditions. Notably, there are six different types of K+ currents that activate at similar range of voltage, and share overlapping kinetics [20-22]. The challenges of this investigation are posed by multiple K+ currents and the complex kinetics of K_v channels.

4.2.2 Computer Model of K_v Channels

In the mouse ventricular cell, there are several different types of K+ currents, i.e., Rapidly inactivating transient outward K+ current ($I_{Kto,f}$), Slow-inactivating transient outward K+ current ($I_{Kto,s}$), Rapid delayed rectifier K+ current (I_{Kr}), ultra-rapidly activating delayed rectifier K+ current (I_{Kur}), non-inactivating steady-state K+ current (I_{Kss}), slow delayed-rectifier K+ current (I_{Ks}), and time-independent K+ current (I_{K1}) [23]. The $I_{Kto,s}$ only exists in the septal cells of mouse ventricle. In this present study, we are investigating the effects of reduced glycosylation on the K_v channels in apical cells, so $I_{Kto,s}$ is equal to zero, and we will use I_{Kto} to denote the $I_{Kto,f}$. The K+ currents are described by the following equations:

Rapidly inactivating transient outward K+ current (I_{Kto}) contributes to the depolarization of APs. It characterizes the isoforms of the $K_v4.2/K_v4.2$, and the model formulation is:

$$I_{Kto} = G_{Kto}a^3{}_{to}i_{to}(V - E_K)$$

$$\frac{da_{to}}{dt} = \alpha_a(1 - a_{to}) - \beta_a a_{to}$$

$$\frac{di_{to}}{dt} = \alpha_i(1 - i_{to}) - \beta_i i_{to}$$

$$\alpha_a = 0.18064e^{0.03577(V+30.0)}$$

$$\beta_a = 0.3956e^{0.06237(V+30.0)}$$

$$\alpha_i = \frac{0.000152e^{-(V+13.5)/7.0}}{0.067083e^{-(V+33.5)/7.0} + 1}$$

$$\beta_i = \frac{0.00095e^{(V+33.5)/7.0}}{0.051335e^{(V+33.5)/7.0} + 1}$$

where G_{Kto} is the maximum whole cell conductance (mS/uF), E_K is the K+ reversal potential, and a_{to} and i_{to} are the activation and inactivation gating variables.

Rapid delayed rectifier K+ current (I_{Kr}) is modeled with a Markov model (see Figure 4-2). The I_{Kr} is presumably encoded by mERG channels with more complex kinetics. The Markov model includes five states, i.e., C_{K0}, C_{K1}, C_{K2}, O_K and I_K. The state transitions are regulated by nonlinear transitions, e.g. α_{a0}, β_{a0}. Each of these transition rate is function of some exponential equations [23-24].
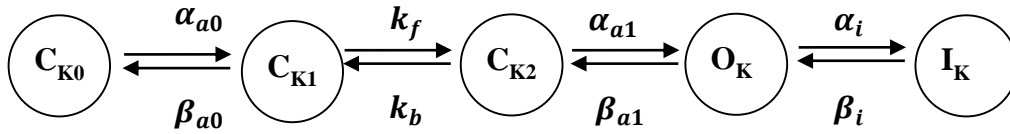

Figure 4-2 Markov model of mERG channel.

I_{Kr} is guided by the following equations:

$$I_{Kr} = G_{Kr}O_K[V - \frac{RT}{F}\ln(\frac{0.98[K^+]_0 + 0.98[Na^+]_0}{0.98[K^+]_i + 0.98[Na^+]_i})]$$

where G_{Kr} is the conductance (mS/uF), O_K is the probability of the channel staying in the open state, R is the ideal gas constand, F is the Faraday constant, and $[K^+]_0$ and $[K^+]_i$ are the K^+ concentrations outside and inside the cell [23]. The formulation for calculating $[K^+]_0$, $[K^+]_i$ and transition rates can be found in [23].

In addition, the I_{Kur} is described by the following differential equations [23]:

$$I_{Kur} = G_{Kur}a_{ur}i_{ur}(V - E_K)$$

$$\frac{da_{ur}}{dt} = \frac{a_{ss} - a_{ur}}{\tau_{aur}}$$

$$\frac{di_{ur}}{dt} = \frac{i_{ss} - i_{ur}}{\tau_{iur}}$$

$$\tau_{aur} = 0.493\, e^{-0.0629V} + 2.058$$

$$\tau_{iur} = 1200.0 - \frac{170.0}{1 + e^{(V+45.2)/5.7}}$$

96

where G_{Kur} and is the maximum whole cell conductance (mS/uF), a_{ur} and i_{ur} are activation and inactivation gates.

The Non-inactivating steady-state K+ current (I_{Kss}) is voltage independent ion current, which is described by the following equations [23]:

$$I_{Kss} = G_{Kss}a_{ss}i_{ss}(V - E_K)$$

$$\frac{da_{Kss}}{dt} = \frac{a_{ss} - a_{Kss}}{\tau_{Kss}}$$

$$\frac{di_{Kss}}{dt} = 0$$

$$\tau_{Kss} = 39.3e^{-0.0862V} + 13.17$$

where G_{Kur} and is the maximum whole cell conductance (mS/uF), a_{ss} and i_{ss} are activation and inactivation gates.

Lastly, the Slow delayed-rectifier K+ current (I_{Ks}) and Time-independent K+ current (I_{K1}) are determined by the following equations:

$$I_{Ks} = G_{Ks}n_{Ks}^2(V - E_K)$$

$$I_{K1} = 0.2938(\frac{[K^+]_0}{[K^+]_0 + 210.0})(\frac{V - E_K}{1 + e^{0.0896(V-E_K)}})$$

4.3 Materials and Experimental Design

4.3.1 Experimental Protocols and Methods

The cells were held at the resting potential, -70mV, then depolarized by a series of voltage steps ranging from -50mV to 50mV for 4.5 seconds in 10mV increments. At each clamp voltage the joint K+ current was collected [6].

The repolarization in adult mouse ventricular myocytes occurs primarily through the action of all the six K+ ion currents. In in-vitro experiments, the joint K+ current, i.e., the sum of all the six currents was measured following some pulse protocols. However, as we mentioned before, these

K+ currents share similar gating kinetics, and it is quite challenging to decompose experimentally the joint K+ currents. In fact, some of these currents, i.e., I_{K1}, I_{Ks} and I_{Kr}, are significantly small and have limited contribution to the joint current. As shown in Figure 4-3, at the clamp voltage of 50mV, the three currents, I_{Kto}, I_{Kur} and I_{Kss}, play significant roles in forming the joint K+ ion current ($I_{K,sum}$). It is also shown that the I_{Kss} does not exhibit any appreciable voltage-dependence. In addition, the I_{Kto} contributes greatly to the peak of the $I_{K,sum}$. This gives advantages of separating the kinetics components mathematically by fitting the decaying portion of the joint K+ current with a bi-exponential function [3,25-28]:

$$f(t) = I_{Kur}e^{-t/tau1} + I_{Kto}e^{-t/tau2} + I_{SS}$$

where I_{Kur} is the amplitude of the ultra-rapidly activating delayed rectifier K+ current of each current trace, I_{Kto} is the amplitude of the rapidly inactivating transient outward K+ current, t is the time in ms, and $tau1$ and $tau2$ are time constants.
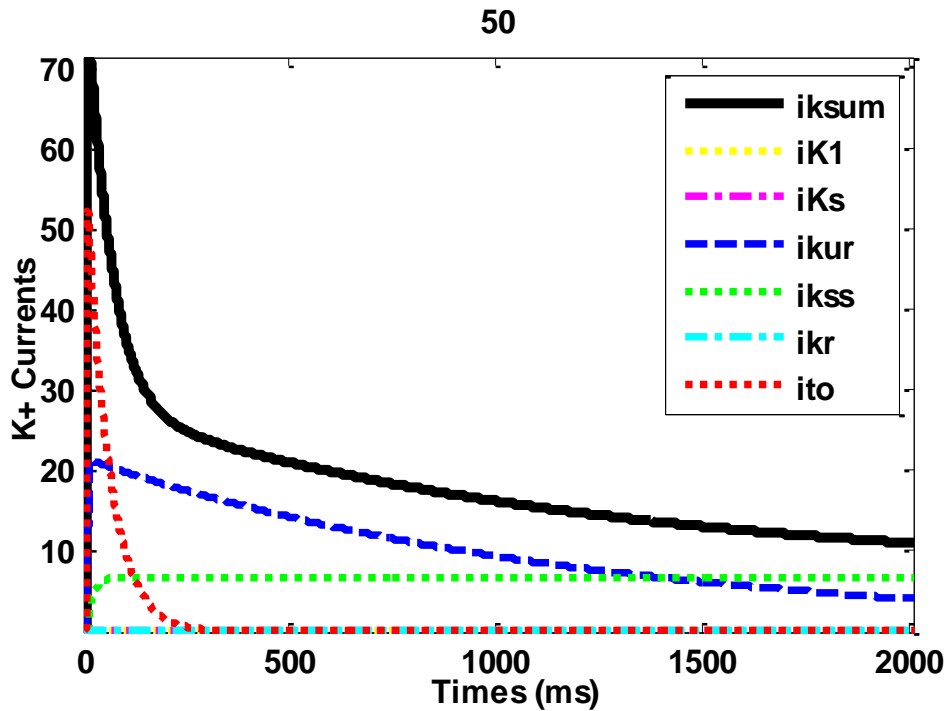

Figure 4-3 K+ currents at clamp voltage of 50mV.

To obtain the Steady-State Activation (SSA), the amplitudes of each component for each current trace, calculated from the bi-exponential function, were divided by the cell capacitance to generate current density (A/F). The conductance (G) can be obtained through dividing the current by the reverse potential using the following equation:

$$G = I/(V - E_K)$$

where I is the current at each clamp voltage, V is the clamp voltage, E_K is the reverse potential that is equal to 83.4mV in our in-vitro experiments. Conductance-voltage relationships were fit with a Boltzmann equation of the form:

$$G/G_{max} = \frac{1}{1 + \exp(-(V - V_a)/K_a)}$$

where V is the membrane potentials, V_a is the half-activation potential, K_a is the slope factor. The normalized data were averaged with those from the other cells to calculate the resulted average G–V curves.

In the experiments of Steady-State Inactivation, cells were held at -70 mV and then pre-pulsed to conditioning voltages ranging from -110 mV to 0 mV in 10 mV increments for 10 seconds. Following the conditioning pulses, the cells were depolarized to 30 mV for 4.5 seconds. The magnitude of I_{Kto}, I_{Kur} and I_{Kss} generated by each current trace were normalized to their corresponding peak currents from the pre-pulse, i.e., the first step to 30mV. The data was fit to a single Boltzmann distribution, from which the mean $V_i \pm$ SEM and $K_i \pm$ SEM values were determined. The fraction of maximal currents is:

$$I/I_{max} = \frac{1}{1 + \exp((V - V_i)/K_i)}$$

where I/I_{max} is the ratio of each current to the maximum current, V is the membrane potential, V_i is the voltage of half-inactivation, K_i is the slope factor.

4.3.2 Physical Experiments

Ednie et al. recently reported the effects of ST3Gal4$^{-/-}$ on K_v channels, showing that ST3Gal4$^{-/-}$ lead to a significant smaller peak density at the clamp voltage of -20mV to 50mV (Figure 4.4a). This peak current was separated using the method mentioned in Section 4.3.1. The decomposed I_{Kto} and I_{Kur} were shown in Figure 4-4 b and c. Physical data is provided by Ednie [6]
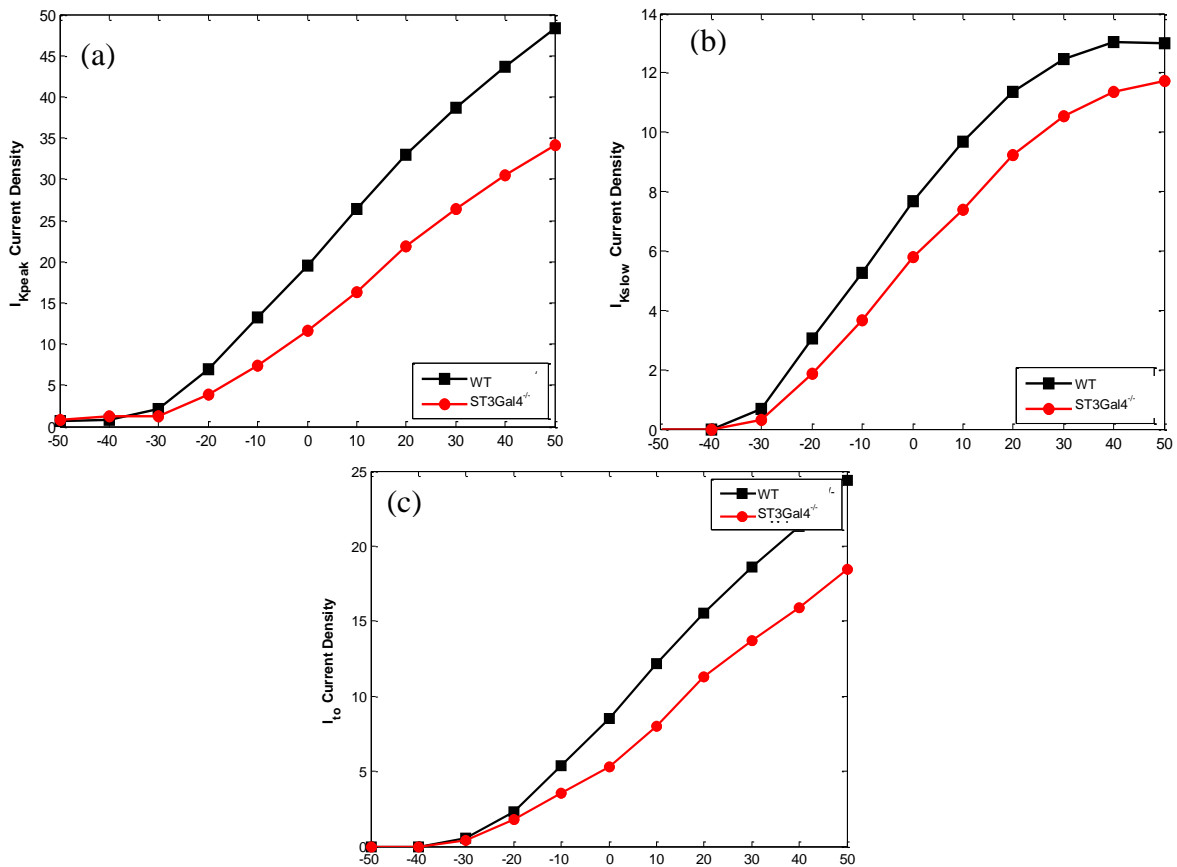

Figure 4-4 ST3Gal4$^{-/-}$ alters K+ currents.

4.3.3 Computer Experiments

The computer experiments are aimed at modeling the effects of ST3Gal4$^{-/-}$ on each individual K+ currents and further predicting the effects on cardiac electrical signaling of ventricular cells.

First, we modified the K_v channel gating equations in the detailed ventricular cell models based on the experimental data shown in the Section 4.2.2. The current density, steady-state activation and inactivation were optimized to fit the experimental results under both ST3Gal4$^{-/-}$ and WT conditions. Second, we simulated and compared the variations of each K+ current and cellular APs with respect to the two conditions. Third, the effects of ST3Gal4$^{-/-}$ on both Na_v and K_v channels are integrated to predict the joint effects on the electrical signaling at the cellular level.

Computer models were implemented using the MATLAB R2014a software from MathWorks (Natick, MA, USA) in a Windows 7 (Microsoft, Redmond, WA, USA) 64-bit machine. Computer experiments follow the same pulse protocols as in-vitro experiments to compute the model responses and to calibrate in-silico models. The models of cardiac cells and K_v channels are solved with the use of Ode15s solver at a maximal step size of 1ms.

4.4   Results

4.4.1 ST3Gal4$^{-/-}$ Affects K_v Channel Activities

The biophysical characterization of K_v channel gating indicated that the Steady-State Activation (SSA) of I_{Kur} channel was shifted to more depolarized potentials along the voltage axis under the ST3Gal4$^{-/-}$ condition [6]. The Steady-State Inactivation (SSI) of I_{Kur} channel shows higher inactivation probability when the clamp voltages are greater than 40mV. Figure 4-5 shows the modeled SSA and SSI. The modeling results are consistent with the in-vitro data, i.e., ST3Gal4$^{-/-}$ shifts the SSA linearly in the depolarized direction, and leads to a delayed de-inactivation at higher potentials (>40mV).

To further validate the modeling results, the current density of I_{Kur} is presented in Figure 4-6. The in-silico study shows that ST3Gal4$^{-/-}$ contributes to decreased I_{Kur} density at smaller, non-saturating membrane potentials.
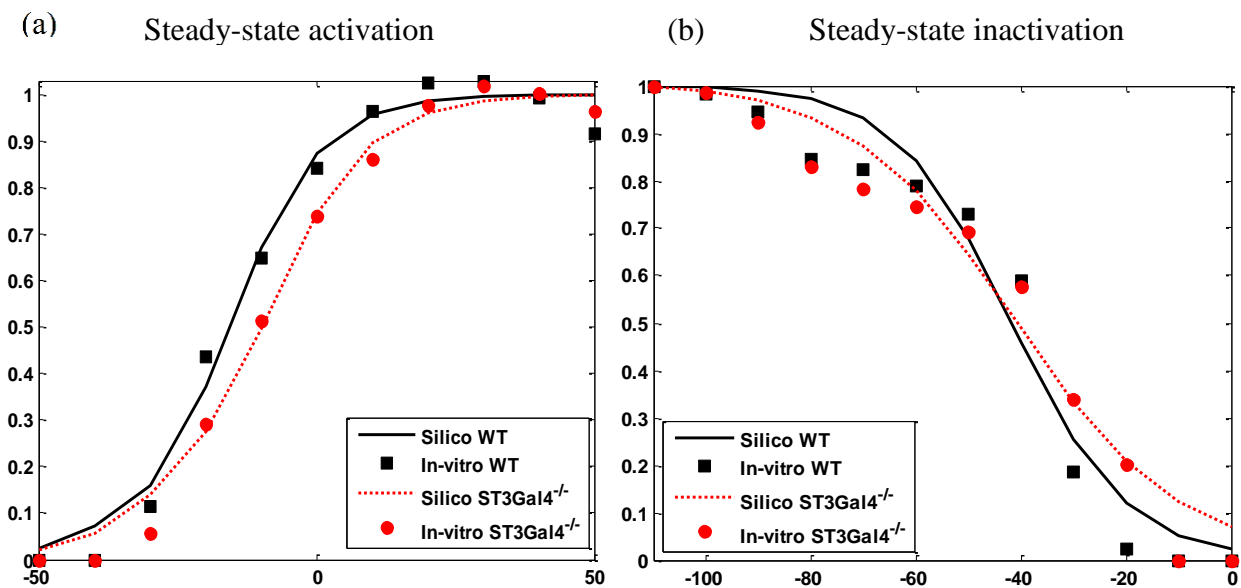
Figure 4-5 The I_{Kur} gating under ST3Gal4$^{-/-}$ and WT conditions. (a) Steady-state activation (b) Steady-state inactivation. (In-vitro data as reported by Ednie [6]: ■WT ● ST3Gal4$^{-/-}$, In-silico data from the I_{Kur} model: straight and dashed lines).
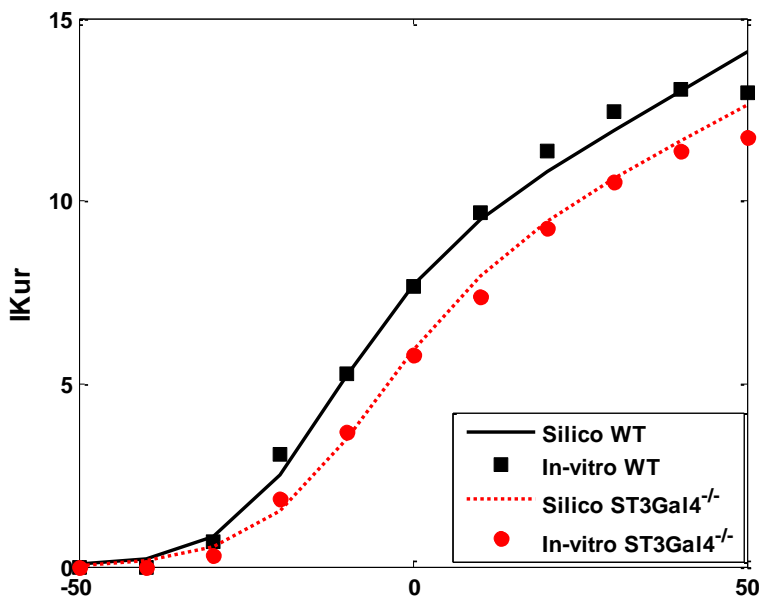

Figure 4-6 Current density of I_{Kur} under ST3Gal4$^{-/-}$ and WT conditions. (In-vitro data as reported by Ednie [6]: ■WT ● ST3Gal4$^{-/-}$, In-silico data from the I_{Kur} model: straight and dashed lines).

In addition to I_{Kur} channel, we also modeled the gating kinetics of I_{Kto} channel under both ST3Gal4$^{-/-}$ and WT conditions. Figure 4-7 shows the in-vitro and in-silico SSA and SSI of I_{Kto} channels. ST3Gal4$^{-/-}$ causes a rightward shift in SSA, which indicates that the channel opens at higher membrane potentials. However, the SSI curve shows no significant difference under the two conditions. Out modeled outputs replicate the physical data well.
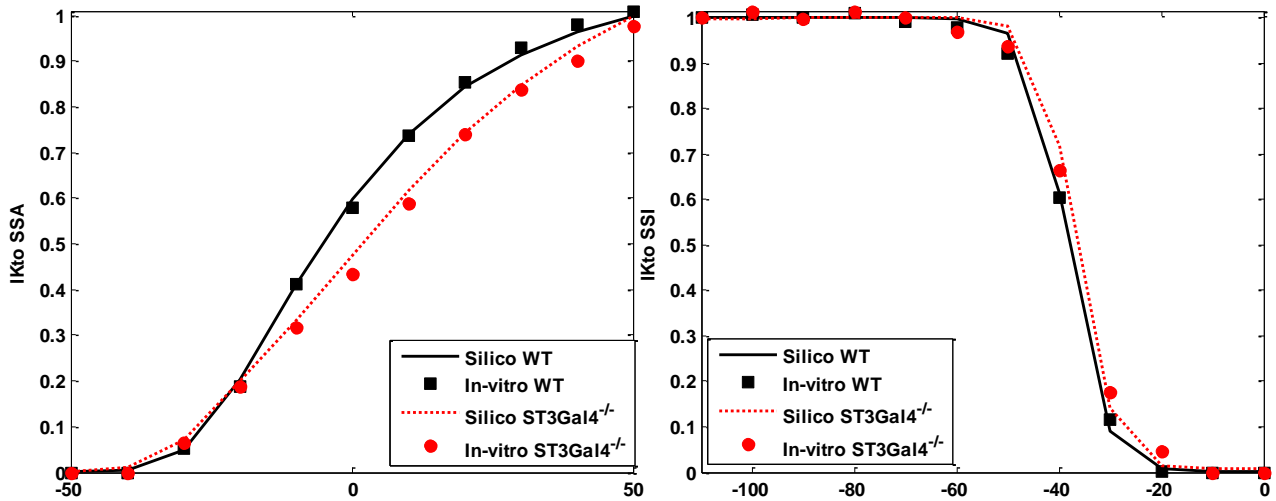

Figure 4-7 The I_{Kto} gating under ST3Gal4$^{-/-}$ and WT conditions. (a) Steady-state activation (b) Steady-state inactivation. (In-vitro data as reported by Ednie [6]: ■WT ● ST3Gal4$^{-/-}$, In-silico data from the I_{Kto} model: straight and dashed lines).

The current density of I_{Kto} was also plotted to test the model accuracy. As shown in Figure 4-8, ST3Gal4$^{-/-}$ leads to a reduced density in I_{Kto} current at more depolarized membrane potentials (>10mV). However, the densities are similar at smaller membrane potentials (-50mV~-10mV) Note that the discrepancy of current density-voltage relationships between computer models and experimental data is minimized for both ST3Gal4$^{-/-}$ and WT myocytes. The computer models are well-calibrated and the result shows that the gating dynamics of I_{Kto} channels is different with ST3Gal4 expression.
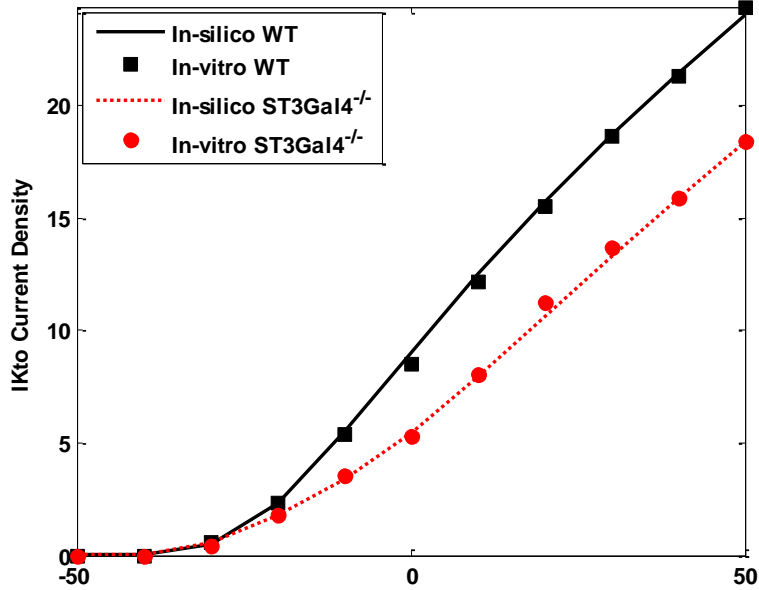
Figure 4-8 Current density of I_{Kto} under ST3Gal4$^{-/-}$ and WT conditions. (In-vitro data as reported by Ednie [6]: ■WT ● ST3Gal4$^{-/-}$, In-silico data from the I_{Kto} model: straight and dashed lines).

4.4.2 ST3Gal4$^{-/-}$ Affects Cellular Activities

We have also integrated the calibrated models of K_v channels into the ventricular cell model to predict whether and how ST3Gal4 gene deletion influence the electrical activity of cardiac cells. It should be noted that the K_v channels are responsible for multiple phases of the AP. Slightly change in each of these K_v channels may affect the depolarization and repolarization of the ventricular cell, and contribute to cellular excitation.

Figure 4-9 shows the three K+ currents: I_{Kur}, I_{Kto} and I_{Kss} during a single cardiac cycle and the AP of ventricular cells. Figure 4-9A indicates that ST3Gal4$^{-/-}$ leads to slower decay in the I_{Kur} current. This contributes to slower depolarization among AP (Figure 4-9C). In addition, ST3Gal4$^{-/-}$ promotes an early rise of I_{Kto}. Furthermore, The AF of ventricular cells is shown in Figure 4-9C, where the repolarization of AP is prolonged and leads to a larger AP duration.
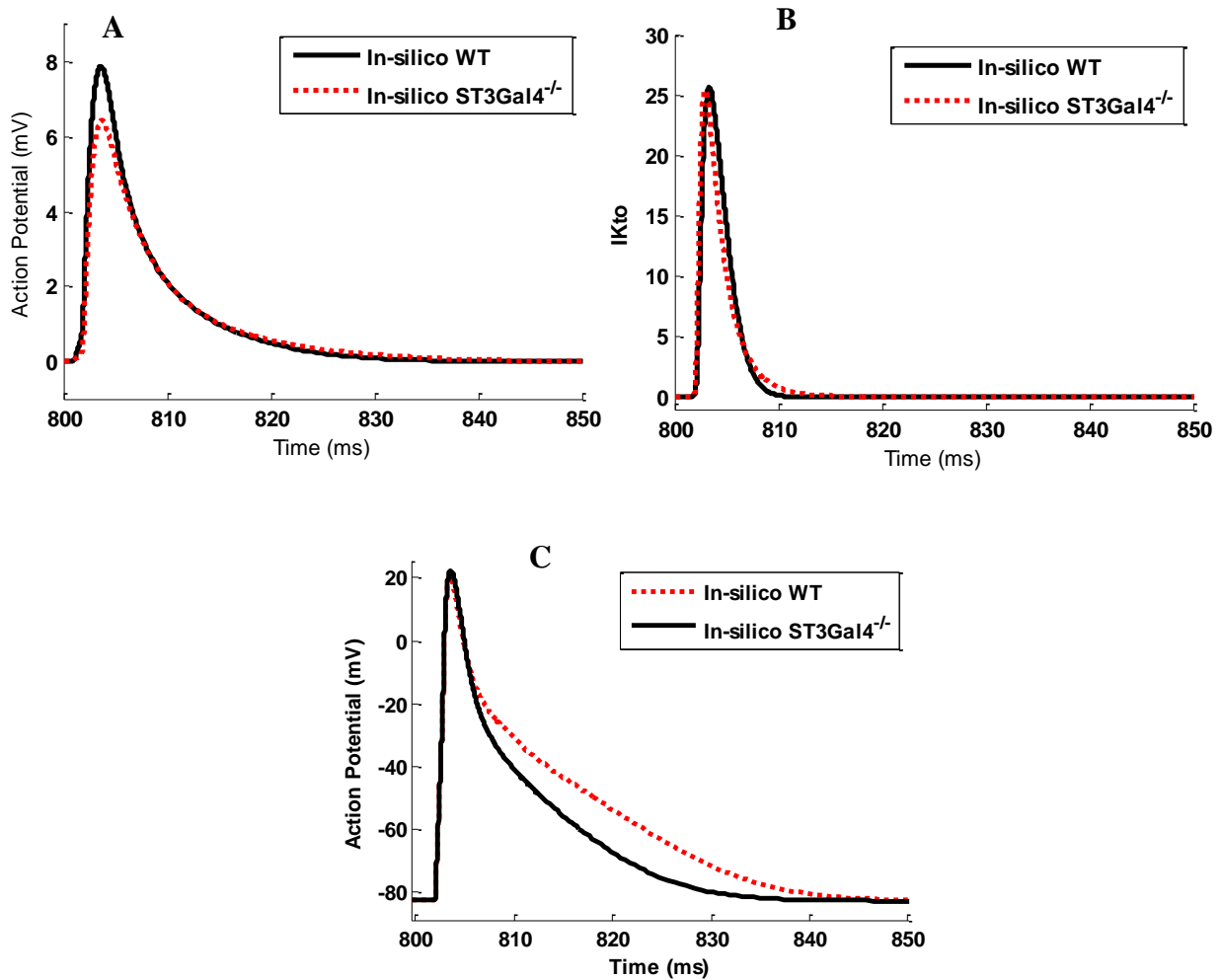
Figure 4-9 Simulated APs and underlying K+ currents of mouse ventricular myocytes under both ST3Gal4$^{-/-}$ and WT conditions. A: I_{Kur}. B: I_{Kto}. C: AP. Black line: WT condition. Red dash line: ST3Gal4$^{-/-}$ condition.

4.5 Conclusions

Mathematical modeling of cardiac myocytes allows one to investigate the detailed disease mechanisms at molecular levels, i.e. channel level, and predict the effects at other physical scales. We coupled in-silico studies with the wealth of experimental data to model, mechanistically, how reduced glycosylation occurring in the ST3Gal4$^{-/-}$ heart affects K_v activities and cardiac electrical signaling. The computer experiments showed that ST3Gal4$^{-/-}$ caused decreased current densities among K+ currents, and delays the repolarization of the AP in ventricular myocytes. This enriches

the fundamental knowledge of how ST3Gal4 defect leads to cardiac dysfunction and further causes cardiac arrhythmias. Once mechanistic details on how ST3Gal4 gene deletion contributes to aberrant electrical signaling in the heart are better understood, potential therapies can be explored to offset glyco-altered gating in ion channels. Further, new designs of therapies could be suggested to correct aberrant glycosylation, i.e., potential corrective gene, environmental, and/or metabolic therapies that could restore the altered cardiac glycome and resume normal cardiac electrical signaling.

4.6   References

[1]   JM Nerbonne. "Molecular basis of functional voltage-gated K+ channel diversity in the mammalian myocardium," J Physiol., vol. 525, Pt 2, pp. 285-98, 2000

[2]   M Tristani-Firouzi, J Chen, JS Mitcheson, MC Sanguinetti. "Molecular biology of K(+) channels and their role in cardiac arrhythmias. Am J Med., vol. 110, pp50-59, 2001

[3]   S Brunet, F Aimond, H Li, W Guo, J Eldstrom, D Fedida, et al. "Heterogeneous expression of repolarizing, voltage-gated K+ currents in adult mouse ventricles, " J Physiol., vol. 559, pp. 103-120, 2004

[4]   HS Wang, JE Dixon, D McKinnon. "Unexpected and differential effects of Clchannel blockers on the Kv4.3 and Kv4.2 K+ channels. Implications for the study of the I(to2) current," Circ Res., vol. 81, pp. 711-718, 1997

[5]   JM Nerbonne, "Studying cardiac arrhythmias in the mouse--a reasonable model for probing mechanisms," Trends Cardiovasc Med., vol. 14, pp. 83-93, 2004

[6]   Ednie A., "Aberrant Sialylation Alters Cardiac Electrical Signaling," Ph.D. dissertation, Dept. of Molecular Pharmacology and Physiology, USF, Tampa, FL, 2012.

[7]   E. Bennett, M. S. Urcan, S. S. Tinkle, A. G. Koszowski and S. R. Levinson, "Contribution of Sialic Acid to the Voltage Dependence of Sodium Channel Gating: A Possible Electrostatic Mechanism," The Journal of General Physiology, vol. 109, pp. 327-343, March 01, 1997.

[8]   E. S. Bennett, "Isoform-specific effects of sialic acid on voltage-dependent Na+ channel gating: functional sialic acids are localized to the S5-S6 loop of domain I," The Journal of Physiology, vol. 538, pp. 675-690, February 01, 2002.

[9]   D. Johnson and E. S. Bennett, "Isoform-specific Effects of the β2 Subunit on Voltage-gated Sodium Channel Gating," Journal of Biological Chemistry, vol. 281, pp. 25875-25881, September 08, 2006.

[10]   D. Johnson, M. L. Montpetit, P. J. Stocker and E. S. Bennett, "The Sialic Acid Component of the ßl Subunit Modulates Voltage-gated Sodium Channel Function," Journal of Biological Chemistry, vol. 279, pp. 44303-44310, October 22, 2004.

[11]   Y. Zhang, H. A. Hartmann and J. Satin, "Glycosylation influences voltage-dependent gating of cardiac and skeletal muscle sodium channels " J. Membr. Biol., vol. 171, pp. 195-207, Oct 1, 1999.

[12]   C. A. Ufret-Vincenty, D. J. Baro, W. J. Lederer, H. A. Rockman, L. E. Quiñones and L. F. Santana, "Role of Sodium Channel Deglycosylation in the Genesis of Cardiac Arrhythmias in Heart Failure," Journal of Biological Chemistry, vol. 276, pp. 28197-28203, July 27, 2001.

[13]   SK Patnaik, P. Stanley, "Lectin-resistant CHO glycosylation mutants," Methods Enzymol., vol. 416, pp. 159-82, 2006.

[14]   JD Esko, P. Stanley, "Glycosylation Mutants of Cultured Cells," in Essentials of Glycobiology, 2th ed. New York: Cold Spring Harbor Laboratory Press, ch. 26, pp. 1–10, 2009.

[15]   WB Thornhill, MB Wu, X Jiang, X Wu, PT Morgan, Margiotta JF. "Expression of Kv1.1 delayed rectifier potassium channels in Lec mutant Chinese hamster ovary cell lines reveals a role for sialidation in channel function," J Biol Chem., vol. 271, pp. 19093-8, 1996.

[16]   JJ Sutachan, I Watanabe, J Zhu, A Gottschalk, E Recio-Pinto, WB Thornhill. Effects of Kv1.1 channel glycosylation on C-type inactivation and simulated action potentials. Brain Res. vol.1058, pp. 30-43, 2005

[17]   I Watanabe, J Zhu, JJ Sutachan, A Gottschalk, E Recio-Pinto, WB Thornhill. "The glycosylation state of Kv1.2 potassium channels affects trafficking, gating, and simulated action potentials," Brain Res., vol. 1144, pp. 1-18, 2007

[18]   TA Schwetz, SA Norring, AR Ednie, ES Bennett. "Sialic acids attached to Oglycans modulate voltage-gated potassium channel gating," J Biol Chem., vol. 286, pp. 4123-32, 2011.

[19]   A. R. Ednie, K. K. Horton, J. Wu and E. S. Bennett, "Expression of the sialyltransferase, ST3Gal4, impacts cardiac voltage-gated sodium channel activity, refractory period and ventricular conduction," J Mol Cell Cardiol, vol. 59, pp. 117-127, 2013.

[20]   J. Liu, K. Kim, B. London, M. J. Morales and P. H. Backx, "Dissection of the voltage-activated potassium outward currents in adult mouse ventricular myocytes: Ito,f, Ito,s, IK,slow1, IK,slow2, and Iss," Basic Res Cardiol, vol. 106, pp. 189-204, 2011.

[21]   J. Brouillette, R. B. Clark, W. R. Giles and C. Fiset, "Functional properties of K+ currents in adult mouse ventricular myocytes," vol. 559, pp. 777-798, 2004.

[22]   S. Brunet, F. Aimond, H. Li, W. Guo, J. Eldstrom, D. Fedida, K. A. Yamada and J. M. Nerbonne, "Heterogeneous expression of repolarizing, voltage-gated K+ currents in adult mouse ventricles," J Physiol., vol. 559, pp. 103-120, 2004.

[23]   V. E. Bondarenko, G. P. Szigeti, G. C. L. Bett, S. Kim and R. L. Rasmusson, "Computer model of action potential of mouse ventricular myocytes," American Journal of Physiology - Heart and Circulatory Physiology, vol. 287, pp. H1378-H1403, September 01, 2004.

[24]   S Wang, S Liu, MJ Morales, HC Strauss, and RL Rasmusson. "A quantitative analysis of the activation and inactivation kinetics of HERG expressed in Xenopus oocytes, " J Physiol., vol. 502, pp. 45–60, 1997.

[25]   W Guo, H Xu, B London, JM Nerbonne. Molecular basis of transient outward K+ current diversity in mouse ventricular myocytes," J Physiol., vol. 521 Pt 3, pp. 587-99, 1999.

[26]   C Marionneau, S Brunet, TP Flagg, TK Pilgram, S Demolombe, JM Nerbonne. "Distinct cellular and molecular mechanisms underlie functional remodeling of repolarizing K+ currents with left ventricular hypertrophy," Circ Res., vol. 102, pp. 1406-15, 2008.

[27]   KC Yang, PY Jay, JR McMullen, JM Nerbonne. "Enhanced cardiac PI3Kalpha signalling mitigates arrhythmogenic electrical remodelling in pathological hypertrophy and heart failure," Cardiovasc Res. vol. 93, pp. 252-62, 2012.

[28]   C Marionneau, F Aimond, S Brunet, N Niwa, B Finck, DP Kelly, et al. "PPARalpha-mediated remodeling of repolarizing voltage-gated K+ (Kv) channels in a mouse model of metabolic cardiomyopathy," J Mol Cell Cardiol. vol. 44, pp. 1002-15, 2008.

[29]   K. H. W. J. ten Tusscher, D. Noble, P. J. Noble and A. V. Panfilov, "A model for human ventricular tissue," Am J Physiol Heart Circ Physiol, vol. 286, pp. 1573-1589, 2004.

[30]   V. E. Bondarenko, G. P. Szigeti, G. C. L. Bett, S. Kim and R. L. Rasmusson, "Computer model of action potential of mouse ventricular myocytes," American Journal of Physiology - Heart and Circulatory Physiology, vol. 287, pp. H1378-H1403, September 01, 2004.

Chapter 5 Computer Modeling and Experiments of Electrical Dynamics in Atrial Fibrillation

Atrial Fibrillation (AF) is a common cardiac arrhythmia that affects more than 5 million Americans. The impact of AF on healthcare systems is overwhelming, due to high risk of stroke, increased mortality, impaired quality of life and hospitalization. Catheter ablation is an established treatment for AF. During the procedure, physicians use the electrodes at the end of catheters to record electrical activity in the atria (i.e., intracardiac electrogram). Further, cardiologists pinpoint the potential AF sources and deliver energy through the catheter to create incision lines that block faulty electrical pathways. However, the understanding of AF initiation and maintenance has remained sketchy at best. One salient problem is the inability to interpret intracardiac recordings, which have thus far been unable to reconstruct the rhythmic mechanisms for AF. As a result, physicians often need to make ablation decisions using ad hoc or heuristic strategies. There is an urgent need to realize the full potentials of intracardiac electrograms for optimizing ablation decisions. The objective of this chapter is to develop and calibrate multi-scale computer models of human atria to simulate fibrillatory conductions that replicate the patterns in clinical recordings. Specifically, the multi-scale model of atrial cell, tissue and organ are built to investigate AF behaviors under different scenarios, and the corresponding intracardiac signals are derived. This research will accelerate the knowledge discovery in the initiation and perpetuation of AF. The research outcomes will positively impact cardiovascular patients, the largest population at risk of death in the world.

5.1 Introduction

Cardiac electrical signaling is an integrative multi-scale system that reflects the orchestrated functions of ion channels, cell, tissues, and organs. The regular heart activity is initiated at the sinoatrial (SA) node. Electrical impulse is generated from the SA node and conducted into bother atria, and then relayed through the antriventricular (AV) node to further propagate through bundle of His and Purkinje fibers toward ventricular depolarization and repolarization [1]. The recursive heartbeat is generated by the repeated stimulation originated from at the SA node. Any electrical impulse initiated at other locations instead of the SA node would disorder the regular heartbeat, and eventually causes life-threatening heart events [2-3].

Atrial Fibrillation (AF) is the most common type of cardiac arrhythmia and leads to significant morbidity and mortality. AF is caused by irregular signals that are initiated at another part of atria other than the SA node or in the nearby pulmonary veins. The abnormal electrical signals spread throughout both atria in a rapid and disorganized way, which disturbs the normal electrical conduction and makes the atria to fibrillate. There are two types of mechanisms that have been identified in triggering and maintaining AF: enhanced automaticity in one or more depolarization, and reentry involving one or more aberrant circuits [4]. Generally, AF includes three stages: paroxysmal AF which usually occurs and lasts for seconds, minutes or even hours and stops by itself; persistent AF which can only be stopped by pharmacological and catheter-based surgical interventions; permanent AF which cannot be easily stopped by treatments.

Catheter ablation is a common invasive procedure that is frequently used to stop either paroxysmal or persistent AF. Pulmonary vein isolation (PVI) is one common strategy for rhythm control in patients with AF. PVI has been proved to be efficient for most paroxysmal AF, but less efficient for persistent AF. Persistent AF happens because some reentrant spiral waves occur and

constantly rotate in atria. The reentrant rotor(s) persistently disorders the regular electrical conduction in the atria. To stop persistent AF, lesions are placed in the left and sometimes right atrium in addition to the lesions circled around pulmonary vein. However, identifying the location of lesion is quite challenging because the strategies should be patient-specific and anatomically-based. It is very critical to correctly target the rotor(s) and avoid the ablation of healthy tissue. In reality, locating the rotors is very difficult due to the complex and convoluted relationships between intracardiac electrogram, i.e., the sensor signals collected during AF surgery for identifying the rotors, and persistence of different patterns, e.g. single rotor, multiple wavelets. Hence, there is an urgent need to realize the full potentials of intracardiac electrograms for optimizing ablation decisions. The objective of this chapter is to develop and calibrate computer models of human atria to simulate fibrillatory conductions that replicate the patterns in clinical recordings. Specifically, we modeled the AF behavior under different scenarios such as enhanced automaticity and reentry, and derived the corresponding intracardiac signals of each scenarios. The research outcomes will accelerate the knowledge discovery in the initiation and perpetuation of AF, which will positively impact cardiovascular patients, the largest population at risk of death in the world.

In this chapter, we simulated AF in 2D tissue and surface of 3D atria to linking the potential mechanisms of AF to the intracardiac signals observed during AF. Section 5.2 presents the multi-scale models for simulating different type of AF; Section 5.3 illustrates the design of experiments and is followed by some experimental results in Section 5.4. Section 5.5 concludes this chapter

5.2 Human Atrial Models

Computer models facilitate the quantitative simulation, elucidation, and understanding of cardiac function in AF. Simulation studies overcome the practical limitations in clinical practices,

and enable the investigation of detailed disease mechanisms. This present study builds multi-scale models of human atrial cell and tissue to examine different AF behavior and the corresponding intracardiac signals. The development of multi-scale atrial model is described as follows.

5.2.1 Model of Human Atrial Myocyte

The cellular excitation is controlled by the orchestrated function of ion channels. When a cardiac myocyte is stimulated, The close, activation, inactivation of ion channels allow the ions (e.g., Na^+, Ca^{++}, and K^+) to cross the membrane. The influx and efflux of ions form some ionic currents that further vary trans-membrane potentials. Specific to human atrial cells, a number of models have been developed in the literature, e.g., the CRN model [5], the Nygren and Fiset model [6] and the Simitev-Biktashev model [7].

In this present investigation, we utilized CRN model to describe the electrophysiological behaviors of human atrial myocytes [5]. The justification is that the AP duration (APD) generated by this model matches clinical observations well. At the same time, the AP waveforms changes adaptively when cells are excited within the average atrial effective refractory period. Refractory period is the time that a cell consumes to get ready for the second excitation after the first excitation. In AF, cells are stimulated frequently by abnormal triggers and rotors, and produce inadequate AP with shorter AD durations (APD) and smaller magnitudes. Capturing the inadequate AP waveforms during the AF is essential for modeling different disease behaviors.

The atrial cell of the CRN model includes 12 different types of ion currents, and the membrane potential V is calculated with the following ordinal differential equation [5]:

$$-C_m \frac{dV}{dt} = I_{Na} + I_{K1} + I_{to} + I_{Kur} + I_{Kr} + I_{Ks} + I_{Ca,L} + I_{p,Ca} + I_{NaK}$$

$$+I_{NaCa} + I_{b,Na} + I_{b,Ca} + I_{stim}$$

where t is time, C_m is the cell capacitance per unit surface area, I_{stim} is the external stimulus current which activates the cell from the resting state. The transmembrane currents include transient outward current (I_{to}), slow delayed rectifier K^+ current (I_{Ks}), rapid delayed rectifier K^+ current (I_{Kr}), inward rectifier current (I_{K1}), Na^+/Ca^{++}exchange current (I_{NaCa}), pump current (I_{NaK}, I_{NaCa}), plateau currents (I_{pCa}), background currents (I_{bCa}, I_{bNa}), fast Na⁺ current (I_{Na}) and L-type Ca^{++} current (I_{CaL}). Most of these voltage-gated ionic currents are modeled in the form of cell conductance, membrane potential gradients and channel gate dynamics. The details of all ion-channel kinetics can be found in references [5]. All parameters and initial values are the same as was given in the CRN model.

5.2.2 Model of Human Atrial Tissue

Cardiac tissue behaves as a functional syncytium, and electrical waves of depolarization and repolarization continuously propagate among the tissues. At the cellular scale, each depolarized cell can stimulate neighboring cells and trigger cell-to-cell conductions. The depolarization of cardiac myocytes is delayed by gap junctions. When modeling the tissue activity, we make the assumption that the electrical propagation can be consider as a continuous process, hence we could simulate the tissue with mathematical descriptions.

In this study, we simulate the electrical propagation in a 1D cable using the following mono-domain reaction-diffusion equation:

$$\frac{\partial V}{\partial t} = -\frac{1}{C_m}(I_{ion} + I_{stim}) + g_{gap}\frac{\partial^2 V}{\partial x^2}$$

and in 2D tissue, the equation is:

$$\frac{\partial V}{\partial t} = -\frac{1}{C_m}(I_{ion} + I_{stim}) + g_{gap}\left(\frac{\partial^2 V}{\partial x^2} + \frac{\partial^2 V}{\partial y^2}\right)$$

where I_{ion} is the sum of trans-membrane ion currents, g_{gap} is the gap junction between cells. To simulate the propagation of cardiac electrical waves along 1D fiber, reaction-diffusion equations are numerically solved with the finite-difference scheme, and no flux boundary condition is assumed to ensure there are no current leakages on the borders. On the 1D and 2D tissues, the numerical finite-difference scheme is formulated as:

$$\frac{V_i^{t+1} - V_i^t}{dt} = -\frac{1}{C_m}(I_{ion} + I_{stim}) - g_{gap}\frac{2V_i^t - V_{i-1}^t - V_{i+1}^t}{dx}$$

$$\frac{V_{i,j}^{t+1} - V_{i,j}^t}{dt} = -\frac{1}{C_m}(I_{ion} + I_{stim}) - g_{gap}(\frac{2V_{i,j}^t - V_{i-1,j}^t - V_{i+1,j}^t}{dx} + \frac{2V_{i,j}^t - V_{i,j-1}^t - V_{i,j-1}^t}{dy})$$

For simplicity, we consider the gap junctions along different directions are identical.

In the 3D surface of the atria, a finite triangular mesh is used to describe the topological surface of both atria. The heart surface, however, is irregular and cannot be approximated by the same way as was described above for 2D tissue. Popular treatment for irregular shapes in various engineering discipline is Finite Element Method (FEM) and similar methods. Unfortunately, typical FEM technique relies on precise formulation of the problem under Cartesian coordinate systems, often assuming the independency of net flux along each axis. The problem of interest here is action potential diffusion along the heart surface, but not homogeneously along the three independent axes of the Cartesian system that the surface is in. For this reason, FEM does not provide a feasible approach in this case. To approximate the diffusion process guided by the Laplace Operator over the surface, one has to start with the fundamental property of the operator to derive the suitable formula.

By the divergence theorem, Laplace Operator of AP integrated over a surface area A is equal to the line integration of net flux around the close boundary S of the surface area A:

$$\int \nabla V dA = \oint F dS$$

114

where V is the action potential, F is the first order derivative of V, A is the surface area, and the integration is circled around this surface area along its boundary.

For sufficiently small area, and sufficiently smooth action potential V over the surface, we can approximate the Laplace Operator at a point as the average of Laplace Operator around its vicinity:

$$\nabla V_p = \frac{1}{A_p} \oint FdS$$

where ∇V_p denotes the approximated Laplace Operator at a point P, and A_p is the surface area around P.

To formulate a FDM-like approximation, we further partition the right-hand-side into n pieces first, with n independent, discrete action potential differential:

$$\nabla V_p = \oint FdS = \sum_{i=1,n} F_i \times S_i / A_p$$

where F_i is the action potential differential and S_i is the length of the boundary covered by i's sub area (See Figure 5-1 a). Also,

$$A_p = \sum_{i=1,n} A_i$$

where A_i is i's sub area. By evaluating this formulation, we are allowed to calculate the circular integration discretely

Apparently, when we are doing the actual approximation, the selection of the pieces surrounding the interested point is arbitrary. However, in order to maintain accuracy, one needs to choose a reasonable set of sub areas. A good choice for triangular mesh is to divide the surface area around point P into fan shaped sectors (see Figure 5-1 b). Each sector has radius equal to half length of the edge it was attached to, and spans half of the angle between the two edges besides P.
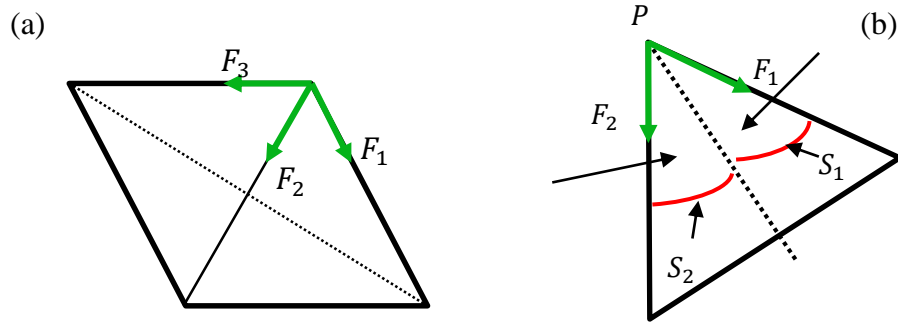
Figure 5-1 Illustration of partial integration in one triangle.

The calculation is based on a few assumptions: (1) We approximate F_i as the difference of action potential between two adjacent vertexes divided by the length of the edge linking them. Because the best estimate of the location where F is equal to this approximation is just half way along the edge, the sector radius is naturally half of the edge's length. (2) We assume the other two points other than P have equivalent weighting when calculating net flux, thus the two sectors have the same angle. (3) We assume F_i is always orthogonal toward the arc of the sector. This eliminates the necessity to calculate the integral along the border between the two sectors.

5.2.3 Intracardiac Electrograms

The intracardiac signals are the most fundamental features for understanding different AF behaviors and locating rotors and wavelets. In surgery, a catheter is placed on the surface of atrial wall, and the potentials at each electrodes of the catheter vary while electrical waves pass through. In this study, catheters are simulated according to the real size and structure in clinical surgery. The potential at each electrode is calculated using the following equation:

$$\emptyset = \iint_S \frac{I_{membrane}}{r} \, dxdy$$

where S is the area over cardiac tissue, $i_{membrane}$ is the transmembrane currents which can be calculated as:

$$I_{membrane} = I_{ion} + C_m \frac{\partial V}{\partial t}$$

and r is given as:

$$r = \sqrt{(x - x_e)^2 + (y - y_e)^2 + z_e^2}$$

where $e = (x_e, y_e, z_e)$ is the location of the electrode, x and y represent the coordinates of cells

on 2D tissue. The $I_{membrane}$ current is obtained with the following equation:

$$I_{membrane} = g_{gap} \left(\frac{\partial^2 V}{\partial x^2} + \frac{\partial^2 V}{\partial y^2} \right)$$

$\emptyset$ gives the signals collected from a single electrode, which is a unipolar signal. In reality, all

recorded signals in the EP laboratory are bipolar. In bipolar catheter, potential differences between

2 electrodes are measured. The potential differences between two electrodes as:

$$CS_{12} = \emptyset(x_{e1}, y_{e1}, z_{e1}) - \emptyset(x_{e2}, y_{e2}, z_{e2})$$

It may be noted that 2-3mm distance is considered between each two electrodes.

5.3 Design of Experiments

5.3.1 Experimental Protocols

In this present investigation, we modeled the electrical propagation in AF among atria at

different scales of 1D fiber, 2D tissue and 3D topological atrial surface. The conductance is chosen

to be 1/4000 in the experiments of 1D and 2D cases.

As we mentioned before, stimulation within the effective refractory period could generate

inadequate AP waveforms, which will further lead to insufficient depolarization and repolarization

among atria. The AF could occur because of the propagations of abnormal and disorganized AP

waveforms. In 1D cable experiments, we tested the APD of atrial cells on 1D cable composed of

600 atrial cells at different pacing rate (PR) of 200ms, 300ms, 400ms and 500ms. The temporal

step is 0.01ms, and the spatial distance between every two neighbor cells is 0.1mm. A 2ms

stimulation (2000pA/pF) is given at the beginning the cable (cell 1-cell 5). Euler method is used to calculate the electrical propagation among the 1D cable.

In 2D tissue, we construct the model by arranging cardiac cells in an array composed of 600 by 600 cardiac cells. Different stimulation strategies are applied: 1) a 4ms stimulation (2000pA/pF) with pacing rate of 500ms is given to the upper left corner of the cell array, which triggers a sequence of electrical waves propagating towards the lower right corner of the tissue. 2) A same stimulation is given at the middle of upper boundary of the cell array (cell (1,300)), which produces electrical waves propagating down to the other side of the tissue. 3) The spiral wave was initiated by applying a first stimulus (S1 = 2 ms) along one side of the tissue to generate a rectilinear wave propagating toward the other side. When the refractory tail of electrical waves reaches the middle, a second stimulus (S2 = 2 ms) will be given in the middle of the tissue, paralleling to the first rectilinear wave and covering only 3/4 of the length of the tissue [9]. The temporal and spatial steps used in 2D experiments are 0.01ms and 0.1mm accordingly.

In the 3D topological surface of atria, we simulate the electrical propagation on a finite triangular mesh (Figure 5-2). Stimulation (2ms, 2000pA/pF) with 500ms pacing rate is give at the Sinoatrial node. The conductance is 1/60 in this current simulation.
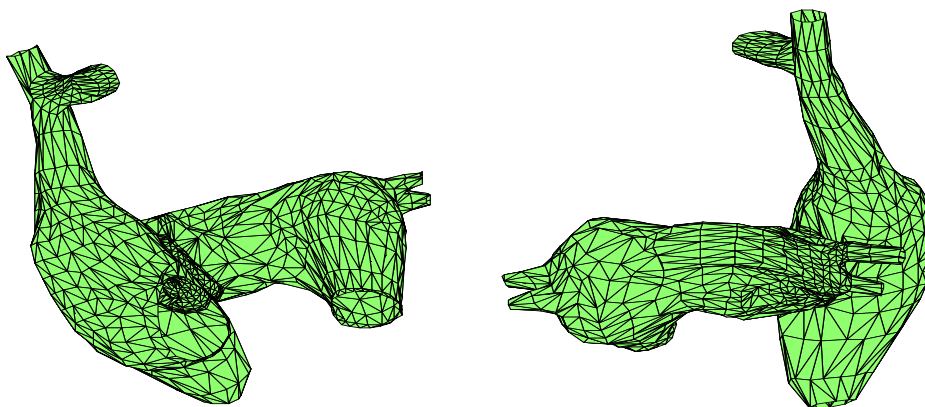
Figure 5-2 Finite element mesh of atria.

All the experiments are implemented on a workstation with an Intel dual core i3-2100 CPU @3.10GHz and 16G of DDR3 memory. The models of 1D and 2D tissue are solved with the use explicit finite-difference methods. Computer models were implemented using MATLAB R2012a software from MathWorks (Natick, MA, USA) in a Windows 7 (Microsoft, Redmond, WA, USA) 64-bit machine.

5.3.2 Catheter Placement

Different types of catheters are used in EP lab, for example ablation catheter, PentaRay catheter. The structures of catheters vary in sizes and number of electrodes. Figure 5-3 shows the design of an ablation catheter, where three electrodes and one ablation electrode are embedded on the flexible polymer body. During the test, catheters will be place against the atrial wall, and each electrodes could measure one lead of electrical signals, i.e., intracardiac signals. In reality, all signals collected in the EP lab are bipolar, i.e., the signals constitute a potential difference between 2 electrodes with the distance of 2-3mm. In this study, we simulate the electrode following the design in reality, and place 4 electrodes with the distance of 2mm-20mm-2mm on the surface of the 2D tissue. The potential signals were calculated using the equations mentioned in Section 5.2.3.

Ablation Catheter   Simulated Catheter
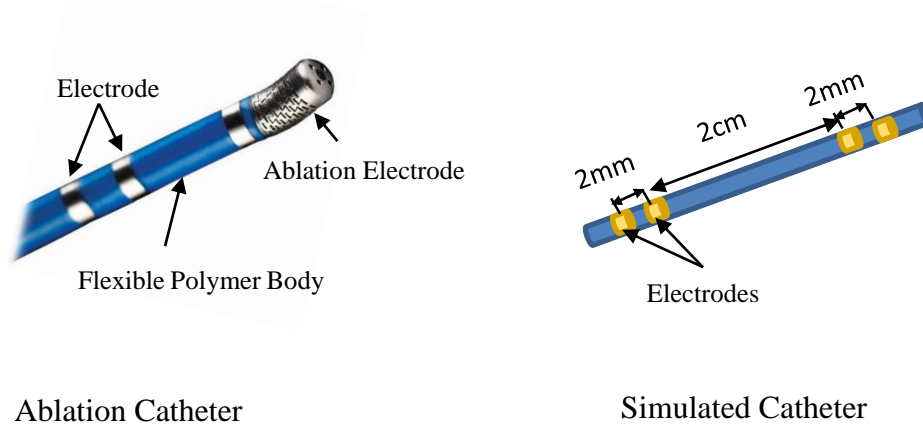
Figure 5-3 Structure of the ablation catheter. (Image on the left is from [10], in public domain.)

119

5.4 Results

5.4.1 APs at Different Pacing Rates on A 1D Cable

We tested the response of atrial cells in the CRN model to different PR of 500ms, 400ms, 300ms and 200ms and 100ms on a 1D cable. Figure 5-4 shows the APs of the 300th cell in the middle of the atrial cable. As shown in Figure 5-4, when stimulation is given every 500ms to the first cell of the cable, the 300th cell generates slightly smaller AP waveforms with shorter plateau phase (Figure 5-4 b). When the PR is 400ms or 200ms (Figure 5-4 c and e), cells produced alternant AP waveforms, i.e., one normal AP followed by one AP with shortened APD lacking plateau phase. It may be noted that if the PR is equal to 300ms, cells show regular and normal AP waveforms (Figure 5-4 d). This is because every other stimulation falls into the absolute refractory period, during which a second stimulus (no matter how strong) will not excite the cell. In this case, the electrical waves are triggered in every 600ms, and propagate smoothly on the cable. This indicates the PR and the abnormality of electrical propagation do not follow linear relationship, i.e., smaller PR is not necessary to be the reason of abnormal electrical propagation among atrial tissue. However, when PR is equal to 100ms, cells cannot get fully excited all the time (Figure 5-4 e). The discussion on how PR affects the electrical propagation among atria is important because abnormal AF waveforms can results in different types of reentry, which further lead to cardiac tachycardia. The vortices of reentry can be a mechanism of life-threatening cardiac arrhythmias.

5.4.2 Modeling of Atrial Fibrillation on 2D Tissue

AF remains a challenging task because the connection between the intracardiac signals and the mechanism of AF is missing. Many efforts have been made to study the intracardiac signals either analytically or statistically, but the progress is limited. This is partially due to scarcity of information about the ground truth, i.e., the exact mechanism of the AF presented in each patient.

In most cases, the information regarding the disease behavior is mainly based on empirical guessing. The limitation mentioned above makes the validation of the developed analytical methods quite challenging. In this section, we investigated the relationships between the intracardiac signals and different types of electrical waves with simulation models.
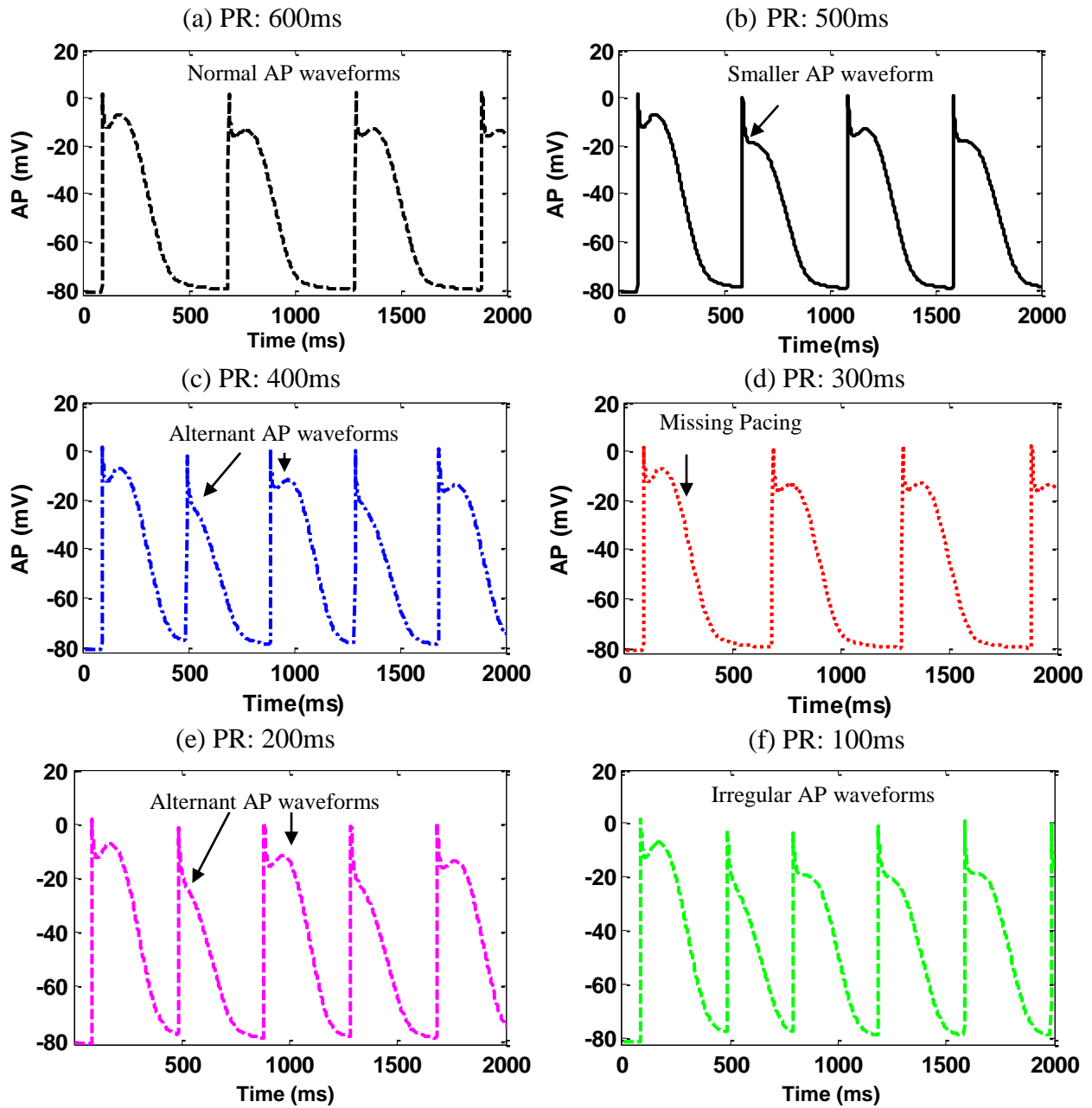
Figure 5-4 AP waveforms of 1D cable at different pacing rates.

We first simulated the regular electrical conduction on a 6cm by 6cm atrial tissue, and placed the modeled electrodes on the surface of the tissue to measure the potential signals. The stimulation protocol is described in Section 5.3.1, i.e., an electrical wave is triggered every 500ms at the upper left corner of the tissue, and the four electrodes are placed horizontally. When the wave passes through the four electrodes, sequence of potential signals are collected (Figure 5-5 c). The difference of the electric potentials collected from electrode 1 and 2, and the difference of the signals collected from electrode 3 and 4 are calculated to obtain the bipolar data (Figure 5-5 b). Figure 5 (a) shows the zoom in of the signals, where the electrical wave takes less time while passing through electrode 1-2 comparing with electrode 3-4, i.e., the time interval between minimal and maximal value of a single waveform is 4.00ms in the signal collected from electrode 1-2, and is 7.73ms in the signal collected from electrode 34. The intracardiac signals show regular and recursive patterns (Figure 5-5 b) since the normal electrical waves were generated by pulse with higher pacing rate.

The patterns of the potential signals highly depend on the locations of the sensors, the angels between the wave font and the sensor direction, as well as the conduction velocities. Furthermore, we placed the four electrodes horizontally, and stimulated electrical wave in the middle of the upper boundary of the tissue (Figure 5-6 c). This generates two leads of intracardiac signals that are symmetrically identical to each other (Figure 5-6 a).

We also simulated the intracardiac signals measured from spiral wave propagation. Following the protocols given in Section 5.3.1, spiral waves were generated on the 2D tissue. The electrodes were placed horizontally on the tissue. Figure 5-7 shows the two leads signals measured by the sensors. Since the wave frequently passes the electrodes, the potential signals present higher frequency (~116ms between each two spike).
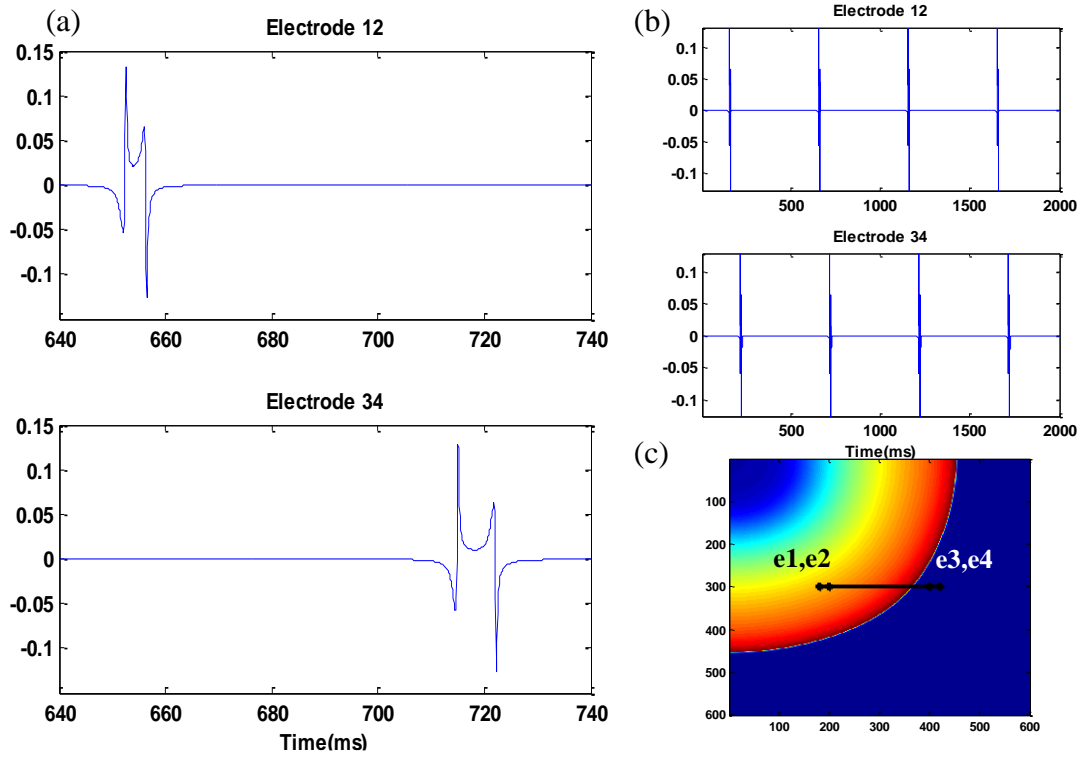
Figure 5-5 Simulated intracardiac signals - asymmetric layout of sensors.
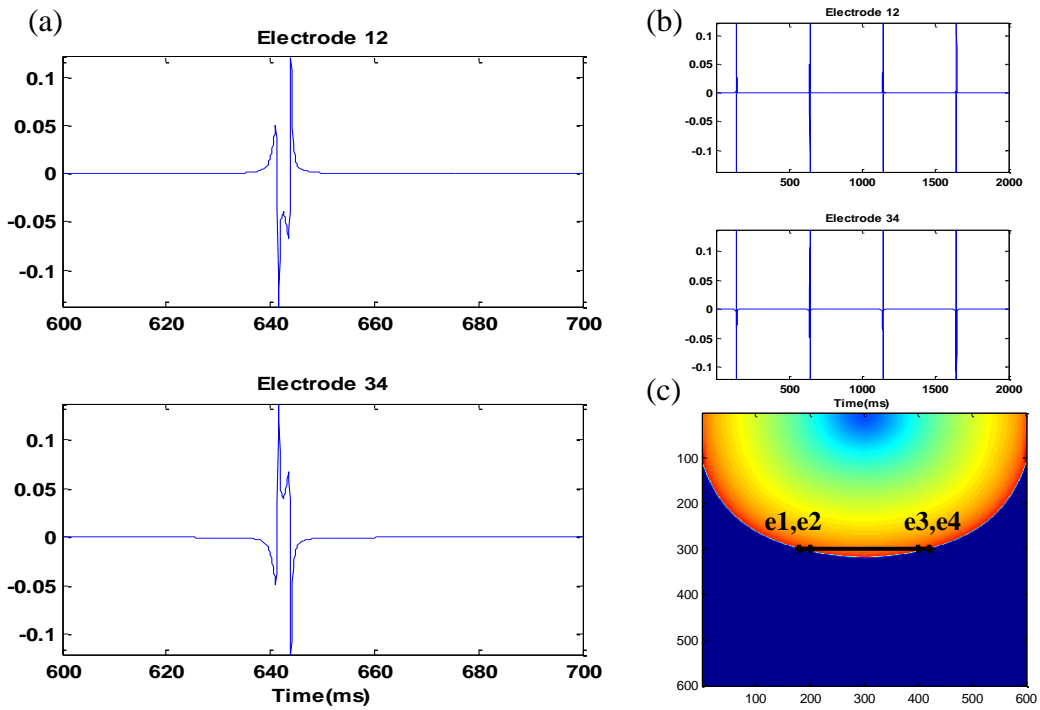
Figure 5-6 Simulated intracardiac signals - symmetric layout of sensors.
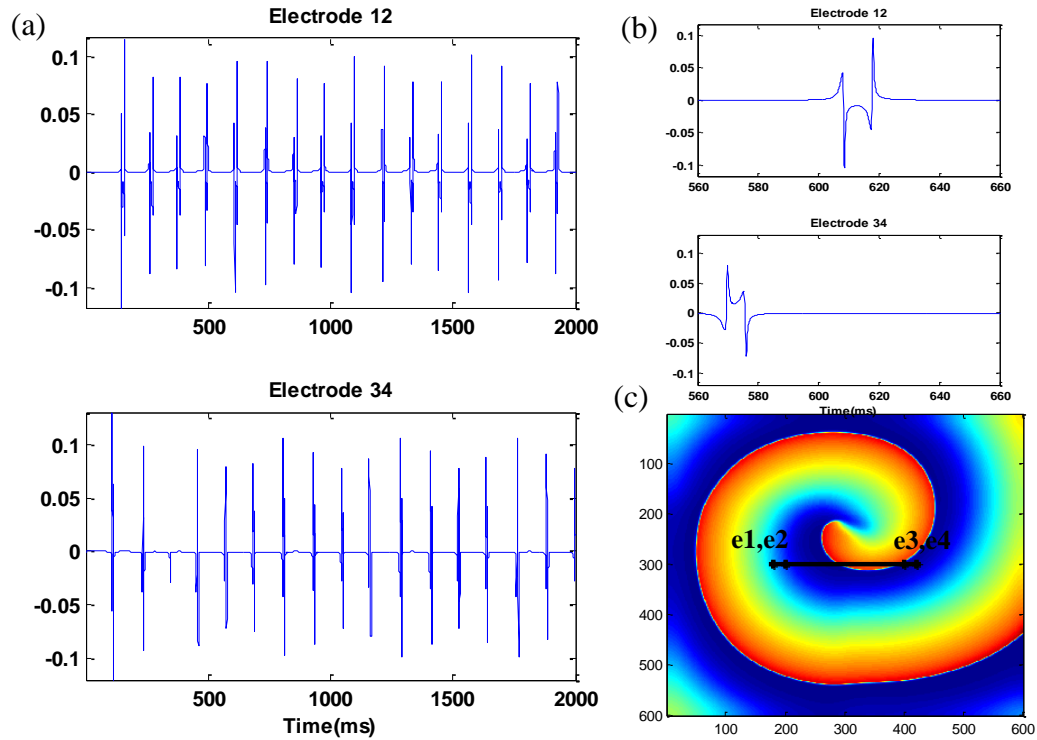
123

Figure 5-7 Simulated intracardiac signals of spiral wave propagation.

5.4.3 Modeling of Atrial Fibrillation on 3D Topological Surface of Atria

The simulation on the 2D flat tissue indicates very important mechanisms of AF and intracardiac signals. After all, 2D simulation produces limited spatial information. It is quite necessary to build 3D models for investigating AF mechanisms and identifying abnormal activations. Studies have demonstrated that the 2D models are sufficient for simulating the electrical activities in atria, since atrial walls are thin, and electrical propagation on the surface of atrial could represent the real signals from the 3D atria.

In this study, we simulated the electrical conduction on the inner surface of both left and right atria. For simplicity, each point in the finite element mesh represents one atrial cell, and cells are connected by gap junction. The AP of each cell is calculated using the CRN model described in Section 5.2.1. Figure 5-8 shows the screenshots of the electrical propagation at 100ms, 600ms,

124

1000ms, 1300ms and 1700ms. Two cells, i.e., below the SA node and on the posterior wall, are selected, and the APs are plotted on the right column. Stimulation is given in every 500ms at the SA node to generate electrical conductions. Since 500ms is smaller than the effective refractory period, the atrial cells present alternant AP waveforms.
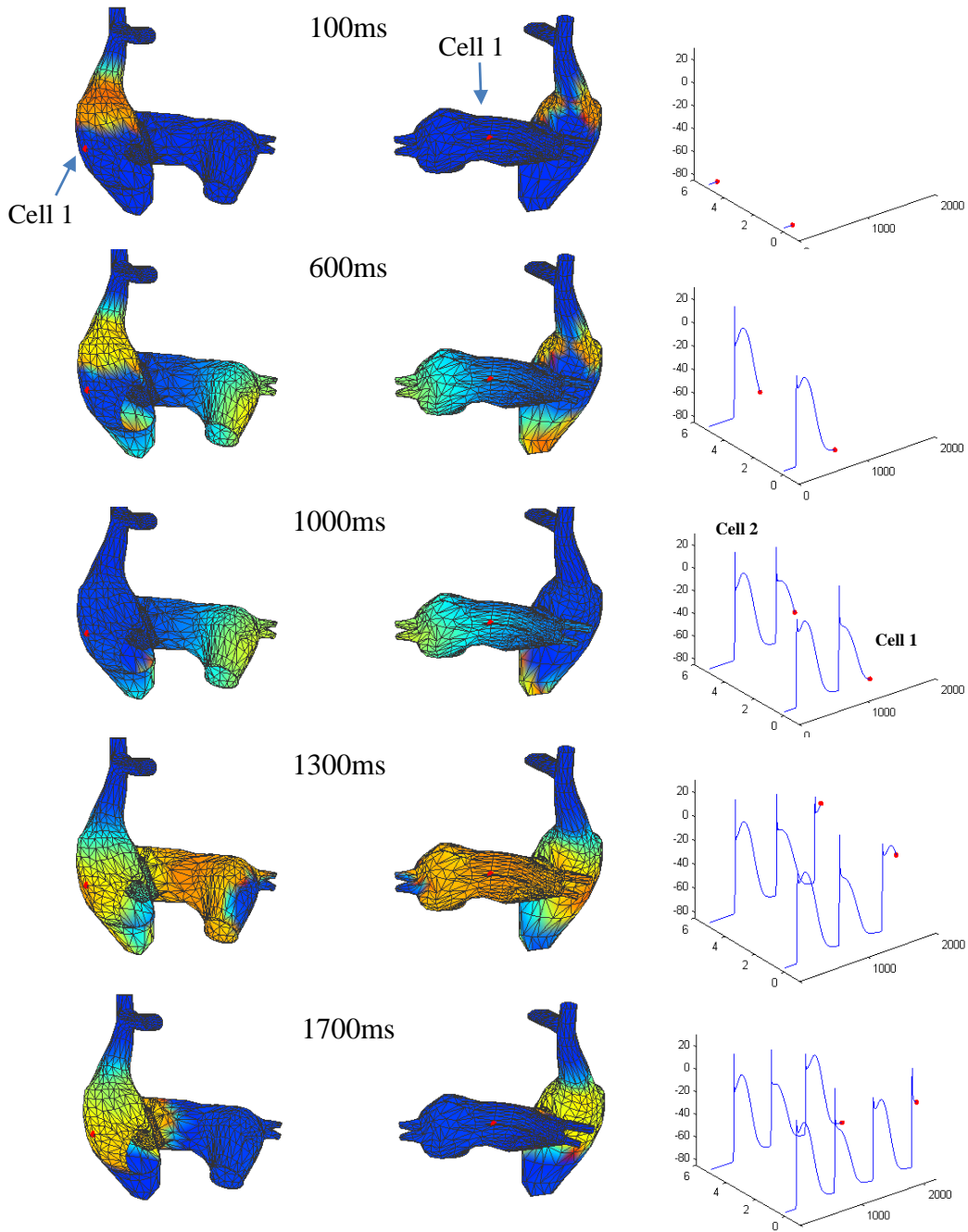
Figure 5-8 Electrical propagation on atria.

125

5.5 Conclusions

AF is a very common cardiac disorder that is associated with high morbidity and mortality. AF is generally caused by electrical impulses generated from abnormal atrial cells other than the natural activations. The most common strategy for treating AF is catheter ablation, i.e., lesions are placed in atria to stop abnormal trigger initiating the fibrillation. However, correctly targeting the location of the lesions remains challenging because there is lacking of theory that links the mechanism of AF with the complex intracardiac signals. The challenges are pose by (1) limited knowledge regarding the real disease behaviors since it is almost impossible to visualize and observe the electrical propagation among human atrial muscles, and (2) the high complexity of the intracardiac signals produced by multiple waves propagating in various directions and rotating at different spots.

Modeling and simulation provide unique opportunity for studying AF mechanisms and developing efficient approaches of diagnosis. In-silico models can simulate different AF behaviors and generate the corresponding intracardiac signals. In this chapter, we built multiscale model of atria and modeled the regular and spiral waves propagating on 1D and 2D tissue. We first test the APs of 1D cable at different pacing cycles, the results showed the irregular pacing rates can lead to alternant AP waveform and inadequate AFs, which will potentially cause cardiac tachycardia and atrial fibrillation. We also derived the intracardiac signals generated by different electrical propagations. In addition, electrical propagation among 3D atrial surface is simulated, and this provides a framework for investigating AF mechanisms and developing robust rotor identification methodologies.

5.6 References

[1]   J. Malmivuo and R. Plonsey, "Bioelectromagnetism: Principles and Applications of Bioelectric and Biomagnetic Fields," New York, NY, USA: Oxford Univ. Press, 1995.

[2]   Vidaillet H, et al. "A population-based study of mortality among patients with atrial fibrillation or flutter," Am J Med.; vol. 113(5), pp365-370, 2002.

[3]   Go AS, Hylek EM, Phillips KA, et al. "Prevalence of diagnosed atrial fibrillation in adults: national implications for rhythm management and stroke prevention: the AnTicoagulation and Risk Factors in Atrial Fibrillation (ATRIA) Study," JAMA. vol. 285, pp2370-2375, 2001.

[4]   J. David Burkhardt, L. Di Biase, A. Natale. "Long-Standing Persistent Atrial Fibrillation," Journal of the American College of Cardiology. 60(19), pp1930-1932, 2012

[5]   M. Courtemanche, R. J. Ramirez, and S. Nattel. "Ionic mechanisms underlying human atrial action potential properties: insights from a mathematical model," *American Physiological Society*, vol, 98, pp 301-321, 1998.

[6]   A. Nygren, C. Fiset, J. W. Clark, D. S. Lindblad, R. B. Clark and W. R. Giles. "Mathematical model of an adult human atrial cell: the role of K+ currents in repolarization," *Circulation Research*. vol. 60, pp1930-1932, 2012.

[7]   R. D. Simitev and V. N. Biktashev. "Conditions for Propagation and Block of Excitation in an Asymptotic Model of Atrial Tissue," Biophysical Journal. vol. 90, pp 2258-2269.

[8]   E. J.Benjamin, P.A.Wolf, R. B. D'Agostino, H. Silbershatz,W. B. Kannel, and D. Levy, "Impact of atrial fibrillation on the risk of death: The Framingham heart study," Circulation, vol. 98, pp. 946–952, Sep. 8, 1998.

[9]   D. Du, H. Yang, S. Norring and E. Bennett, "In-Silico Modeling of Glycosylation Modulation Dynamics in hERG Ion Channels and Cardiac Electrical Signals," IEEE Journal of Biomedical and Health Informatics, vol. 18, pp. 205-214, 2014.

[10]   Medical EXPO The online medical devices exhibition, St. Jude Medical: Ablation catheter/irrigated. Available: http://www.medicalexpo.com/

Chapter 6 Conclusions

Physical experiments are expensive and difficult to conduct, and often encounter many practical and ethical limitations. These limitations have posed significant challenges for knowledge discovery and scientific research. Computer experiments and simulation optimization provide an unprecedented opportunity for addressing those challenges. This research developed innovative methodologies for modeling and optimizing complex systems, and creates enabling technologies for improving cardiac healthcare. Specifically, this study integrates physics-based models with statistical methodologies to improve the understanding of pathological changes in the heart. It enables and assists in (i) developing a system-level mechanistic understanding of multi-scale cardiac systems from ions to cells to tissues to the whole heart; (ii) improving the understanding of disease pathologies and creating better diagnostic/prognostic tools; and (iii) optimizing pharmaceutical designs and medical treatment planning.

This study integrates in-silico models with the wealth of data from in-vitro experiments to model and predict glycosylation modulation dynamics of multi-scale cardiac electrical signaling. This research provides new pharmaceutical targets for the long QT syndrome and potentially other cardiac disorders.

It is well known that computer models of cardiovascular systems involve greater levels of complexity such as high-dimensional parameter space, nonlinear and non-convex equations. Traditional linear and nonlinear optimization methods have encountered many difficulties for

model calibration. This research develops a new statistical metamodeling approach for efficient computer experiments and optimization of large-scale cardiac models.

The results and experience gained from my previous projects lay a solid foundation for my continued research and innovation. As a next vertical step, my future research will be focusing on design of experiments and simulation optimization with application in healthcare and systems engineering. Specifically, the following topics will be interested: Multi-scale physical-statistical modeling of complex systems with focus on uncertainty analysis; Optimizing cardiac surgical treatment and planning; Design and analysis of physical and computer experiments for leveraging in-silico and in-vitro experiments.

Appendices

Appendix A Copyright Permissions

Below is permission for the use of material in Chapter 2.

About the Author

Dongping Du received Bachelor's and Master's Degree in Electrical Engineering from CUMTB, Beijing, China in 2008 and 2010. She also received a Master Degree in Industrial Engineering at University of South Florida, Tampa in 2012. She is currently a Ph.D. candidate in the department of Industrial and Management Systems Engineering at University of South Florida. Her research interests include nonlinear stochastic modeling and analysis of complex systems with application in healthcare and system engineering. She received the 1st place in IBM best student paper competition, and one of her papers was featured by IEEE Journal of Biomedical and Health Informatics.